Master's Thesis

Long Range Coulomb Interactions in Nearly Metallic Carbon Nanotubes

Marius Folden Simonsen

Supervisors: Karsten Flensberg and Mark Rudner

Center for Quantum Devices, Niels Bohr Institute
University of Copenhagen

13 February 2014

Abstract

Tight-binding models show that many metallic carbon nanotubes have a gapped band structure due to curvature and spin-orbit effects, making them only nearly metallic. The predicted spin-orbit coupling and orbital magnetic moment of these tubes are however smaller than what experiments show. In this thesis, an effective model for long range Coulomb interactions is derived. Through the random phase approximation, it is shown that Coulomb interactions are heavily screened due to excitations in the four Dirac cones. The screened interaction is used to perturbatively calculate how the gap is modified by Coulomb interactions. The results reduce the discrepancy between theoretical and experimental orbital magnetic moments and spin-orbit coupling.

Resumé

Tight-binding-beregninger har vist, at mange metalliske kulstofnanorør har et gab i båndstrukturen på grund af krumningseffekter og spin-banekobling. Dette båndgab gør, at disse rør kun er næsten metalliske. Forsøg viser dog, at spin-banekoblingen og det orbitale magnetiske moment i disse rør er større end forudsagt af tight-binding-modellen. I dette speciale bliver en effektiv model for langtrækkende Coulomb-vekselvirkninger udledt. Det viser sig ved brug modellen random phase approximation, at disse vekselvirkninger bliver skærmet af spontant eksciterede elektron-hulpar i de fire Dirac kegler. Den reducerede Coulomb-vekselvirkning bliver brugt i førsteordens perturbationsteori til at beregne båndgabet. Dette båndgab ligger tættere op ad eksperimentelle resultater end det båndgab, tight-binding-modellen forudsiger.

Acknowledgements

I would first and foremost like to thank my supervisors Karsten Flensberg and Mark Rudner. It has been invaluable to have supervisors who have always made time for discussing my thesis, no matter how many questions I have had. In the same manner I thank Mathias Rosdahl Jensen and Kim Georg Lind Pedersen for always being ready for discussing any problems I encountered, both when it came to fundamental principles and mere factors of 2. Finally I would like to thank Samuel Sanchez, Konrad Wölms and Esben Bork Hansen for proofreading and valuable inputs. Without their help this thesis would be far less readable.

Marius Folden Simonsen
Center for Quantum Devices, Niels Bohr Institute
University of Copenhagen
13 February 2014

Contents

Chapter 1

Introduction

A carbon nanotube can be viewed as graphene sheet that has been rolled up into a cylinder. Its band structure can therefore be approximated by a one-dimensional version of the graphene band structure. By further including curvature and spin-orbit effects, one may calculate the band structure to high precision under the assumption that the electrons do not interact with each other. There is however increasing experimental evidence that this calculated band structure is not the full picture [1, 2]. Recent work [3] on electron-electron interactions in carbon nanotubes gives promising explanations of some of the discrepancies between experiments and the non-interacting theory. The goal of this thesis is to find out whether some of the remaining unexplained experimental results for nearly metallic carbon nanotubes are due to long range interelectronic Coulomb interactions.

1.1 A carbon nanotube

In nature, carbon appears in several forms, including graphite. Graphite is a macroscopic crystal structure consisting solely of carbon. It can be viewed as a stack of weakly bound two-dimensional layers, called graphene. The carbon atoms of each graphene layer are organized in a hexagonal lattice, and are bound much more tightly to each other than to atoms in neighboring graphene layers in a graphite crystal [4]. The weak binding of the graphene layers in graphite makes it easy to rub off material from a piece of graphite, which is why it is used for pencil leads. However, graphene was first isolated in a fashion that facilitates quantum transport measurements 2004 by Geim, Novoselov, et al. [5, 6]. As predicted by Wallace in 1947 [4], they found the band structure close to the Fermi energy of neutral graphene to be linear,

$$E_{\boldsymbol{k}} = \pm v_F \sqrt{k_x^2 + k_y^2}, \tag{1.1}$$

resembling the one for massless Dirac fermions in two-dimensional free space [7, sec. 3.2], [8, sec. 1], [9]. v_F is called the Fermi velocity, and is approximately equal to 10^6m/s, so 300 times less than the speed of light, by which free space massless Dirac fermions travel. The dispersion relation thus forms a cone in energy momentum space. There are two of

those cones in the Brillouin zone, and the momentum space coordinates of their vertices are called the Dirac points. The band structure of graphene will be derived in Chapter 2.

A carbon nanotube can be viewed as a sheet of graphene, where two of the sides have been folded together to create a cylinder. In the same way as graphene layers can stick together to form graphite, carbon nanotubes can lie inside each other, a structure called a multi-walled carbon nanotube. In this thesis we will solely be concerned with single-walled carbon nanotubes. A typical radius of a carbon nanotube is 1 nm, while the length can be of the order $\sim 1\,\mu$m. In the same way as graphene is a quasi two-dimensional material, a carbon nanotube is therefore quasi one-dimensional. Its properties are determined by the radius and the chirality. The smaller the radius, the larger the curvature, so we expect a larger difference from the graphene band structure for tubes with a small radius. The chirality is a measure of the circumferential direction with respect to the hexagonal lattice. This determines whether the tube is metallic or semiconducting.

The band structure of a carbon nanotube can approximately be found by a particle-on-a-ring approximation [10, problem 6.7], giving several subbands that can be viewed as one-dimensional slices of the graphene band structure, as seen in Fig. 3.2. For some chiralities one of the subbands cross the Dirac point, giving a linear band structure. This is called a metallic tube, since there is no band gap. For other chiralities there are no subbands crossing the Dirac point. There will thus be a band gap even in the lowest subband, making the tube semiconducting. For many metallic tubes, small gaps also open due to curvature [11, 12] and spin-orbit effects [12], indicating that they are only nearly metallic. It was shown that the gaps opened for spin up and down electrons are not the same, and the whole spin up band is shifted in energy compared to the spin down band. Therefore the energy difference between a spin up and a spin down state in the conduction band is different from the energy difference between a spin up and a spin down state in the valence band. For metallic tubes, theory predicts that the splitting between spin up and spin down electrons should be smaller than the hole splitting.

At the bottom of the conduction band and top of the valence band the energy splitting in both conduction and valence band in a nearly metallic tube has been measured by Kuemmeth et al. [2]. They found an electron splitting of $0.37 \pm 0.02\,$meV and a hole splitting of $0.21 \pm 0.01\,$meV, in contradiction to the non-interacting theoretical prediction. The conduction band splitting has also been measured by Steele et al. [1]. They got a spin up down splitting of 3.4 meV, which is 13 times larger than the theoretically predicted value [12]. In this thesis we will show that Coulomb interactions enhance the theoretically predicted value by a factor 1.7.

The above results can be obtained by transport experiments, where the carbon nanotube is placed between two electrical leads, a source and a drain. When an electric potential difference between the source and drain is applied, a current may run through the tube if an energy level lies between the source and drain potential. In these experiments, the nanotube is also capacitively coupled to an electrical gate. When the electrical potential of the gate is changed, the energy levels of the nanotube are shifted. This corresponds to changing the chemical potential. It is therefore possible to tune the gate voltage such that the gap lies between the source and gate potential, inhibiting current from running through the tube. By changing the gate voltage until a current starts to run, one

may find the size of the gap. Additional information about the system can be otained by applying a magnetic field through the tube while performing the transport experiments. This changes the gap due to the Aharonov-Bohm effect [13, p. 141-145], [2], which is most easily understood in the particle-on-a-ring picture. A magnetic field B through the tube shifts the circumferential momentum vector by

$$k_\perp \to k_\perp + \frac{eRB}{2}, \tag{1.2}$$

where e is the electron charge and R is the radius of the nanotube. Since the gap in the non-interacting theory is proportional to $k_\perp$, it can be tuned by the magnetic field. Typically these measurements are expressed in terms of the orbital magnetic moment,

$$\mu_{\text{orb}} = \frac{1}{2}\frac{dE_{\text{gap}}}{dB}, \tag{1.3}$$

where E_{gap} is the energy difference between the valence and conduction band at zero momentum. μ_{orb} can be calculated from the radius and Fermi velocity of the tube. This has been done by Kuemmeth et al. [2], Steele et al. [1], Deshpande et al. [14], Jespersen et al. [15], Minot et al. [16] and many others, [17, 18, 19, 20]. Kuemmeth, Steele, Jespersen and Minot all measured orbital magnetic moments that are about twice as high as expected from the non-interacting theory. Jespersen's and Minot's measurements can be explained by short range Coulomb interactions, as shown by Kane et al. [3]. This is however not enough to account for Kuemmeth's and Steele's results. It is shown in this thesis that long range interactions may partly account for this discrepancy. The non-interacting theory predicts that it should be possible to tune the magnetic field to zero energy gap. In Steele's and Deshpande's experiments, they found a non-zero minimal energy gap of up to 120 meV. It has been proposed that this could be interpreted as a transition to a Mott insulating state [21, 22, 23].

1.2 Coulomb interactions

The calculation of the band structure in the non-interacting theory assumes that each electron is affected only by the fixed potential of the carbon atoms, and not by the electric potential of all the other electrons. This might seem strange at first, since the negative charge of the electrons is just as large as the positive charge of the nuclei. If we consider that the charge of the electrons to be homogeneously distributed in the nanotube, each electron would be repelled by the same amount, regardless of which state it is in. The whole band structure would thus be shifted in energy, see Sections 5.3 and 5.6.1. Such a constant shift is however not measurable, since the zero point energy is always measured relative to the surroundings. In practice it would thus not alter the band structure. Therefore only inhomogeneities in the electron cloud can change the energy levels. In Fermi liquid theory [24, chap. 15], the interacting Hamiltonian and eigenstates are created by starting with the non-interacting Hamiltonian and eigenstates, and then adiabatically turning on interactions. In this way each non-interacting eigenstate is slowly transformed into an eigenstate of the interacting Halmiltonian. This description does not work for all solid

state systems, the most relevant example for us being metallic nanotubes, where second order perturbation theory diverges. They can however be described by Luttinger liquid theory instead [24, chap. 19], [25]. Through perturbation theory, nearly metallic carbon nanotubes have also been examined using Luttinger liquid theory [26], see Section 5.4.

Most electrons are situated far below the Fermi surface, so there are no quantum states nearby to which they can be excited by Coulomb interactions. There is only a small amount of electrons close to the Fermi surface, for which interactions are not suppressed by the energy cost of reaching the Fermi surface. Therefore interaction effects will be dominated by these near surface electrons. Since there is a one-to-one correspondence between the non-interacting and the interacting eigenstates, the exact interacting eigenvalues can be found from infinite order perturbation theory using the interacting Hamiltonian on the non-interacting eigenstates. As mentioned earlier, there are two Dirac points in the Brillouin zone, so including spin there are effectively $N_f = 4$ Dirac cones in our model. Coulomb interactions induce electron hole pairs, similar to excitons, in all four cones, as described in Chapter 6. The more cones there are, the more important exciton interactions are, compared to other types of interactions. Including only this type of interaction is called the random phase approximation or $1/N_f$ expansion [27]. Due to the high number of cones ($N_f = 4$), this is a good approximation, as we will see in Section 6.3. Excitons effectively screen the electron from the field of the other electrons. The quasiparticle eigenstates of the interacting theory can thus be viewed as bare electrons which are protected from the surroundings by a cushion of excitons. Effectively, the random phase approximation screens the interaction, making low order perturbation theory in the interaction strength more precise. In Chapter 5 it is shown that the first order term increases the gap in qualitatively the same way as was previously found in graphene [28] and semiconducting nanotubes [3].

Chapter 2

Band structure of graphene

The band structure of a carbon nanotube is to a large extent a one-dimensional version of the band structure of graphene. Much can therefore be learned about nanotubes from studying graphene. Since graphene is geometrically less complex than a nanotube, the theory is also simpler. We will therefore start out by deriving the band structure of graphene.

2.1 The carbon atom

Carbon is the sixth element of the periodic table, and therefore has 6 electrons. Assuming that they are non-interacting, the basis of hydrogenic eigenstates written as $|nlm\rangle$ will be a useful representation of their quantum state [10, sec. 4.2]. Since they obey the Pauli exclusion principle, the $1s$ state with $n = 1$ must be completely filled with two electrons, while the four remaining electrons are distributed among the $2s, 2p_x, 2p_y, 2p_z$ states with $n = 2$.

2.2 Geometry

It has been found [5, 6] that carbon atoms can form a two-dimensional periodic hexagonal lattice, called graphene, as shown in Fig. 2.1. Any d-dimensional periodic lattice can be described by a unit cell and d linearly independent primitive vectors. The unit cell is a group of atoms in some geometrical configuration. When identical unit cells are placed next to each other to fill all of space, a periodic lattice is generated. The vectors connecting different unit cells in the lattice are called lattice vectors. All lattice vectors $\boldsymbol{r}$ can be expressed in terms of some primitive vectors $\boldsymbol{a}_i$ as

$$\boldsymbol{r} = \sum_{i=1}^{d} n_i \boldsymbol{a}_i, \quad n_i \in \mathbb{Z} \tag{2.1}$$

where n_i is an integer. From this definition, it can be seen that a unit cell is not uniquely defined, since we could always double the size of our unit cell, and still be able to generate

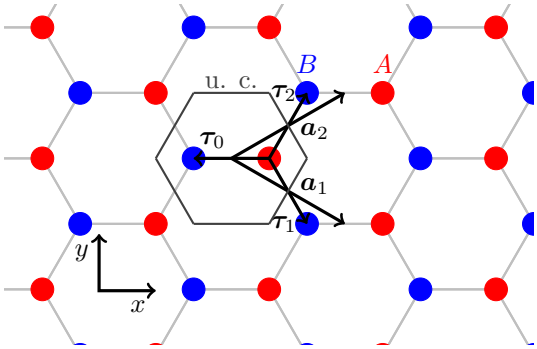

Figure 2.1: Graphene. The red and blue circles represent the A and B sublattices. The hexagon is the Wigner-Seitz primitive unit cell, which contains one A and one B atom. It generates the entire lattice through translations by integer linear combinations of the primitive lattice vectors $\boldsymbol{a}_1$ and $\boldsymbol{a}_2$.

the entire lattice. However, for simplicity we usually define the primitive unit cell, or just the unit cell, as the smallest possible unit cell. It is seen from Fig. 2.1 that a unit cell containing only one atom would not be able to generate the entire graphene lattice from only two primitive vectors. However the hexagon containing the two atoms A and B can be used to generate the entire lattice through translations along $\boldsymbol{a}_1$ or $\boldsymbol{a}_2$, so this hexagon must be the unit cell, and $\boldsymbol{a}_1$ and $\boldsymbol{a}_2$ a set of primitive vectors. The shape of the unit cell is not unique as defined above. We choose to construct the unit cell as the area enclosed by the lines perpendicular to the lattice vectors situated at the middle of the lattice vectors, as shown in Fig. 2.1. This is called a Wigner-Seitz primitive cell.

The four nearest unit cells are displaced along the vectors $\boldsymbol{a}_1$, $\boldsymbol{a}_2$, $-\boldsymbol{a}_1$ and $-\boldsymbol{a}_2$. The unit cells are enumerated by an index j, their position is denoted by $\boldsymbol{R}_j$ relative to the first unit cell, and the atoms are divided into two sublattices A_j and B_j. As seen on figure Fig. 2.1, each A-atom has three B-atoms as its nearest neighbors, with the vectors $\boldsymbol{\tau}_0$, $\boldsymbol{\tau}_1$ and $\boldsymbol{\tau}_2$ going from the A-atom to each of the B-atoms. They are related by

$$\boldsymbol{\tau}_i = \boldsymbol{a}_i + \boldsymbol{\tau}_0 \quad \text{for} \quad i \in \{0, 1, 2\}, \tag{2.2}$$

$$\tag{2.3}$$

where we have introduced $\boldsymbol{a}_0$ as the zero vector for notational simplicity. The distance between neighboring A and B atoms is $a_{\mathrm{C-C}} = |\boldsymbol{\tau}_i| = 1.42\text{Å}$. A coordinate system is chosen such that

$$\boldsymbol{\tau}_0 = a_{\mathrm{C-C}} \begin{pmatrix} -1 \\ 0 \end{pmatrix}, \tag{2.4}$$

$$\boldsymbol{a}_1 = \frac{a}{2} \begin{pmatrix} \sqrt{3} \\ -1 \end{pmatrix}, \tag{2.5}$$

$$\boldsymbol{a}_2 = \frac{a}{2} \begin{pmatrix} \sqrt{3} \\ 1 \end{pmatrix}. \tag{2.6}$$

For using Bloch's theorem, it is convenient to define the reciprocal lattice. It has reciprocal lattice vectors instead of lattice vectors and fundamental reciprocal lattice vectors instead of primitive vectors. The fundamental reciprocal lattice vectors $\boldsymbol{b}_i$ are found from the primitive vectors by the condition [29, p. 61]

$$\boldsymbol{b}_i \cdot \boldsymbol{a}_j = 2\pi\delta_{ij}, \tag{2.7}$$

giving

$$\boldsymbol{b}_1 = \frac{2\pi}{a}\begin{pmatrix} \frac{1}{\sqrt{3}} \\ -1 \end{pmatrix}, \tag{2.8}$$

$$\boldsymbol{b}_2 = \frac{2\pi}{a}\begin{pmatrix} \frac{1}{\sqrt{3}} \\ 1 \end{pmatrix}. \tag{2.9}$$

The reciprocal lattice consists of all integer linear combinations of $\boldsymbol{b}_1$ and $\boldsymbol{b}_2$, so a reciprocal lattice vector $\boldsymbol{G}$ can be written as

$$\boldsymbol{G} = n_1\boldsymbol{b}_1 + n_2\boldsymbol{b}_2 \quad \text{for} \quad n_1, n_2 \in \mathbb{N}. \tag{2.10}$$

The Wigner-Seitz primitive cell in the reciprocal lattice that generates the entire reciprocal lattice through translation by the reciprocal lattice vectors, and is called the first Brillouin zone or just the Brillouin zone. The reciprocal space is also called $\boldsymbol{k}$-space. All quantum states of the system can be described by a wave vector in the Brillouin zone, so each vector outside the Brillouin zone generates the same quantum states as some vector inside the Brillouin zone.

The s-orbital introduced in Section 2.1 is spherically symmetric, while the p_x-, p_y- and p_z-orbitals are symmetric around the $x-, y-$ and $z-$axis. The two-dimensional structure of graphene breaks the three-dimensional rotational symmetry of the carbon atom, and the axis orthogonal to the plane will be called the $z-$axis [30]. In the plane, graphene is symmetric under a $2\pi/3$ rotation, so the eigenstates of graphene are better described by a set of states obeying this symmetry than the s, p_x-, p_y- and p_z-orbitals. Let us now examine how the orbitals introduced in Section 2.1 hybridize in graphene. The two $1s$ electrons are too tightly bound to the nucleus to participate in the formation of graphene. The in-plane orbitals $2s, 2p_x, 2p_y$ hybridize to an $sp2$ structure. The hybridized orbitals are given as

$$|\sigma_i\rangle = \frac{1}{\sqrt{3}}|s\rangle + \sqrt{\frac{2}{3}}|p_i\rangle, \tag{2.11}$$

where p_i is a p-orbital in the direction of the bond. $|\sigma_i\rangle$ is called a σ-orbital. The wave function of a p_z-orbital is [10, p. 164], in standard spherical coordinates where $r^2 = x^2 + y^2 + z^2$ and $\cos\theta = z/r$,

$$\psi_{p_z}(r, \theta, \phi) = \alpha \cos\theta e^{-r/\beta}, \tag{2.12}$$

where α is a normalization and β depends on the screened charge of the nucleus. p_x and p_y have the same form, just aligned along the x- and y-axes instead of the z-axis. In the $|nlm\rangle$ basis,

$$|2p_x\rangle = \frac{1}{\sqrt{2}}\left(-|211\rangle + |21-1\rangle\right), \tag{2.13}$$

$$|2p_y\rangle = \frac{i}{\sqrt{2}}(|211\rangle + |21-1\rangle), \tag{2.14}$$

$$|2p_z\rangle = |210\rangle. \tag{2.15}$$

It can be easily shown from Eq. (2.12) that a general p-orbital along the unit vector $a_x^i\hat{\boldsymbol{x}} + a_y^i\hat{\boldsymbol{y}} + a_z^i\hat{\boldsymbol{z}}$ can be expressed as

$$|p_i\rangle = a_x^i|p_x\rangle + a_y^i|p_y\rangle + a_z^i|p_z\rangle. \tag{2.16}$$

Therefore, if we choose the x-axis along the first bond, the three $sp2$-orbitals can be written

$$|\sigma_1\rangle = \frac{1}{\sqrt{3}}|s\rangle + \sqrt{\frac{2}{3}}|p_x\rangle, \tag{2.17}$$

$$\begin{aligned}|\sigma_2\rangle &= \frac{1}{\sqrt{3}}|s\rangle + \sqrt{\frac{2}{3}}\left(\cos\left(\frac{2\pi}{3}\right)|p_x\rangle + \sin\left(\frac{2\pi}{3}\right)|p_y\rangle\right)\\ &= \frac{1}{\sqrt{3}}|s\rangle + \sqrt{\frac{2}{3}}\left(-\frac{1}{2}|p_x\rangle + \frac{\sqrt{3}}{2}|p_y\rangle\right)\\ &= \frac{1}{\sqrt{3}}|s\rangle - \sqrt{\frac{1}{6}}|p_x\rangle + \sqrt{\frac{1}{2}}|p_y\rangle,\end{aligned} \tag{2.18}$$

and from symmetry

$$|\sigma_3\rangle = \frac{1}{\sqrt{3}}|s\rangle - \sqrt{\frac{1}{6}}|p_x\rangle - \sqrt{\frac{1}{2}}|p_y\rangle. \tag{2.19}$$

It is easily seen that they are orthonormal, and orthogonal to p_z. The p_z-orbital will be called a π-orbital in the following.

2.3 Graphene band structure

As described in Section 2.2, the carbon atoms of graphene form a periodic lattice. To a good approximation, this lattice can be assumed to be rigid, and we may neglect inter-electronic interactions. Therefore the Hamiltonian of a single electron is

$$H = T + \sum_i^N \left(V_{A_i} + V_{B_i}\right), \tag{2.20}$$

where N is the number of unit cells, T is the kinetic energy operator, and V_{A_i} and V_{B_i} are the spherical Coulomb potentials of the nuclei at A and B atoms in the i'th unit cell.

This is invariant under discrete translations along the lattice vectors, so Bloch's theorem may be applied [29, p. 305]. It states that an eigenstate of a periodic potential will only change by a phase when the wavefunction is translated by a lattice vector.

To calculate the band structure, the tight-binding approximation will be used. In tight-binding, the eigenstates of the Hamiltonian are approximated as a superposition of orbitals of free atoms, given by

$$|\phi_{\nu,\boldsymbol{k}}\rangle = \frac{1}{\sqrt{N}} \sum_{j}^{N} e^{i\boldsymbol{k}\cdot\boldsymbol{R}_j} \sum_{\mu} (\alpha_{\nu\mu}|\phi_{\mu,A}(\boldsymbol{R}_j)\rangle + \beta_{\nu\mu}|\phi_{\mu,B}(\boldsymbol{R}_j)\rangle), \tag{2.21}$$

where $\boldsymbol{R}_j$ is a lattice vector, $\phi_{\mu,A(B)}(\boldsymbol{R}_j)$ is an atomic orbital centered at the $A(B)$ atom in the unit cell at position $\boldsymbol{R}_j$, $\alpha_{\nu\mu}, \beta_{\nu\mu}$ are constants, which have the normalization $\sum_\mu |\alpha_{\nu\mu}|^2 + |\beta_{\nu\mu}|^2 = 1$, and $\boldsymbol{k}$ is a wave vector in the Brillouin zone. The normalization is not exactly 1 due to the finite overlap between orbitals on neighboring atoms, but this will be neglected. If we write $|\psi_{\mu,\boldsymbol{k}}\rangle$ in the position basis

$$\psi_{\nu,\boldsymbol{k}}(\boldsymbol{r}) = \frac{1}{\sqrt{N}} \sum_{j}^{N} e^{i\boldsymbol{k}\cdot\boldsymbol{R}_j} \sum_{\mu} (\alpha_{\nu\mu}\phi_{\mu,A}(\boldsymbol{r}-\boldsymbol{R}_j) + \beta_{\nu\mu}\phi_{\mu,B}(\boldsymbol{r}-\boldsymbol{R}_j)), \tag{2.22}$$

it is easily seen that it fullfills the Bloch condition, since

$$\begin{aligned}
\psi_{\nu,\boldsymbol{k}}(\boldsymbol{r}-\boldsymbol{R}_i) =& \frac{1}{\sqrt{N}} \sum_{j}^{N} e^{i\boldsymbol{k}\cdot\boldsymbol{R}_j} \sum_{\mu} (\alpha_{\nu\mu}\phi_{\mu,A}(\boldsymbol{r}-\boldsymbol{R}_i-\boldsymbol{R}_j) + \beta_{\nu\mu}\phi_{\mu,B}(\boldsymbol{r}-\boldsymbol{R}_i-\boldsymbol{R}_j)) \\
=& e^{-i\boldsymbol{k}\cdot\boldsymbol{R}_i} \frac{1}{\sqrt{N}} \sum_{j}^{N} e^{i\boldsymbol{k}\cdot(\boldsymbol{R}_j+\boldsymbol{R}_i)} \sum_{\mu} (\alpha_{\nu\mu}\phi_{\mu,A}(\boldsymbol{r}-\boldsymbol{R}_i-\boldsymbol{R}_j) \\
& + \beta_{\nu\mu}\phi_{\mu,B}(\boldsymbol{r}-\boldsymbol{R}_i-\boldsymbol{R}_j)) \\
=& e^{-i\boldsymbol{k}\cdot\boldsymbol{R}_i}\psi_{\nu,\boldsymbol{k}}(\boldsymbol{r}).
\end{aligned} \tag{2.23}$$

From Bloch's theorem, it is known that the Hamiltonian is diagonal in $\boldsymbol{k}$ space, when the basis is chosen as Eq. (2.21).

As described in Section 2.2, the σ-orbitals form the chemical bonds that bind graphene together. The two σ-orbitals on neighboring atoms hybridize to a bonding and an anti-bonding state. The bonding state has a much lower energy than a free σ-orbital, thus forming the bond. The antibonding state has a higher energy, so it is empty. Therefore three electrons are bound in the σ-bands. Since the π-orbitals do not participate in the bonding, their energy remains the same regardless of the formation of graphene, and their band thus lies between the filled bonding band and the empty antibonding band. Out of the six electrons of a carbon atom, two are bound by the $1s$ orbital and three by the σ-orbitals, so there is one left for the π-band. Since there is space for two electrons in a π-orbital, the π-band will be half filled. We are interested in transport phenomena close to zero chemical potential, so only the π-band will participate in transport, and therefore it is only necessary to examine the structure of the π-band.

From Eq. (2.12) it will now be shown that a π-orbital is not only orthogonal to the σ-orbitals on the same atom, but also to all the other σ-orbitals. The π-orbital wave function is antisymmetric in the π-direction. A σ_i-orbital is rotationally symmetric around an axis i in the plane, so it is symmetric in the π-direction. An s-orbital is also rotationally symmetric, so it is also symmetric in the π-direction. Therefore the integral of the product of the $\pi-$ and $\sigma-$wave functions is zero, so they are orthogonal. Since the π-orbitals are orthogonal to the σ-orbitals, the two bands do not mix, and we can examine the π-band separately. We will follow the derivation of Lunde, [31].

The π-band wave functions must be a linear combination of the π-orbitals on the A- and B-atom in the unit cell. Therefore

$$|\psi_{\boldsymbol{k}}\rangle = \frac{1}{\sqrt{N}} \sum_{j}^{N} e^{i\boldsymbol{k}\cdot\boldsymbol{R}_j} (\alpha |p_\pi^A(\boldsymbol{R}_j)\rangle + \beta |p_\pi^B(\boldsymbol{R}_j)\rangle), \tag{2.24}$$

where α and β are constants to be determined by diagonalisation,

$$H|\psi_{\boldsymbol{k}}\rangle = \epsilon_{\boldsymbol{k}} |\psi_{\boldsymbol{k}}\rangle. \tag{2.25}$$

By multiplying from the left with $\langle\psi_{\boldsymbol{k}}|$, we can transform this into a problem of solving a 2×2 matrix. Since $|p_\pi^A\rangle$ and $|p_\pi^B\rangle$ are not orthogonal, there will be an overlap matrix, so

$$\begin{pmatrix} H_{AA,\boldsymbol{k}} & H_{AB,\boldsymbol{k}} \\ H_{BA,\boldsymbol{k}} & H_{BB,\boldsymbol{k}} \end{pmatrix} \begin{pmatrix} \alpha \\ \beta \end{pmatrix} = \epsilon_{\boldsymbol{k}} \begin{pmatrix} S_{AA,\boldsymbol{k}} & S_{AB,\boldsymbol{k}} \\ S_{BA,\boldsymbol{k}} & S_{BB,\boldsymbol{k}} \end{pmatrix} \begin{pmatrix} \alpha \\ \beta \end{pmatrix}, \tag{2.26}$$

where

$$H^*_{X'X,\boldsymbol{k}} = H_{XX',\boldsymbol{k}} = \frac{1}{N} \sum_{j}^{N} e^{-i\boldsymbol{k}\cdot\boldsymbol{R}_j} \sum_{l}^{N} e^{i\boldsymbol{k}\cdot\boldsymbol{R}_l} \langle p_\pi^X(\boldsymbol{R}_j)|H|p_\pi^{X'}(\boldsymbol{R}_l)\rangle, \tag{2.27}$$

$$S^*_{X'X,\boldsymbol{k}} = S_{XX',\boldsymbol{k}} = \frac{1}{N} \sum_{j}^{N} e^{-i\boldsymbol{k}\cdot\boldsymbol{R}_j} \sum_{l}^{N} e^{i\boldsymbol{k}\cdot\boldsymbol{R}_l} \langle p_\pi^X(\boldsymbol{R}_j)|p_\pi^{X'}(\boldsymbol{R}_l)\rangle. \tag{2.28}$$

Here we have introduced the notation X, X' for representing either A or B, and we will use $\bar{X}$ as not X, such that if $X = A$, then $\bar{X} = B$ and vice versa. Since the π-orbitals fall off exponentially fast in distance from the nucleus, everything else than nearest neighbor interactions can be neglected. As described in Section 2.2, X-atoms only have $\bar{X}$-atoms

as nearest neighbors. Therefore

$$\begin{aligned}
H_{XX,\boldsymbol{k}} &= \frac{1}{N}\sum_{j}^{N} e^{-i\boldsymbol{k}\cdot\boldsymbol{R}_j}\sum_{l}^{N} e^{i\boldsymbol{k}\cdot\boldsymbol{R}_l}\langle p_\pi^X(\boldsymbol{R}_j)|H|p_\pi^X(\boldsymbol{R}_l)\rangle\delta_{j,l} \\
&= \langle p_\pi^X(0)|(T+V_X(0))|p_\pi^X(0)\rangle, && (2.29)\\
H_{X\bar{X},\boldsymbol{k}} &= \frac{1}{N}\sum_{j}^{N} e^{-i\boldsymbol{k}\cdot\boldsymbol{R}_j}\sum_{l}^{N} e^{i\boldsymbol{k}\cdot\boldsymbol{R}_l}\langle p_\pi^X(\boldsymbol{R}_j)|H|p_\pi^{\bar{X}}(\boldsymbol{R}_l)\rangle\sum_{i=0}^{2}\delta_{\boldsymbol{R}_l-\boldsymbol{R}_j,\pm\boldsymbol{a}_i} \\
&= \sum_{i=0}^{2} e^{\pm i\boldsymbol{k}\cdot\boldsymbol{a}_i}\langle p_\pi^X(0)|(T+V_X(0)+V_{\bar{X}(\pm\boldsymbol{a}_i)})|p_\pi^{\bar{X}}(\pm\boldsymbol{a}_i)\rangle && (2.30)\\
&= \sum_{i=0}^{2} e^{\pm i\boldsymbol{k}\cdot\boldsymbol{a}_i}\langle p_\pi^X(0)|(T+V_X(0)+V_{\bar{X}}(0))|p_\pi^{\bar{X}}(0)\rangle, && (2.31)\\
S_{XX,\boldsymbol{k}} &= \langle p_\pi^X(0)|p_\pi^X(0)\rangle = 1, && (2.32)\\
S_{X\bar{X},\boldsymbol{k}} &= \sum_{i=0}^{2} e^{\pm i\boldsymbol{k}\cdot\boldsymbol{a}_i}\langle p_\pi^X(0)|p_\pi^{\bar{X}}(0)\rangle. && (2.33)
\end{aligned}$$

Here we have introduced $\pm\boldsymbol{a}_i$ corresponding to $X = A, B$ respectively. When going from Eq. (2.30) to Eq. (2.31), we have used the fact that both the atomic potentials and the π-orbitals are rotationally symmetric in the π-direction. The matrix elements are renamed to

$$\begin{aligned}
\langle p_\pi^X(0)|(T+V_X(0))|p_\pi^X(0)\rangle &= \epsilon_0, && (2.34)\\
\langle p_\pi^X(0)|(T+V_X(0)+V_{\bar{X}}(0))|p_\pi^{\bar{X}}(0)\rangle &= -\gamma_0, && (2.35)\\
\langle p_\pi^X(0)|p_\pi^{\bar{X}}(0)\rangle &= s_0. && (2.36)
\end{aligned}$$

The entire band structure has been calculated numerically [32] using the LCAO method [10, sec. 7.3], where interactions have been included in the Hartree-Fock approximation [24, sec. 4.3]. To get the same band structure from our analytical calculation, the parameters should be $\gamma_0 = 3.033\,\mathrm{eV}$ and $s_0 = 0.129$ [30, p. 27]. We will see in the following that ϵ_0 is fixed by the zero of the energy scale, so it bears no physical significance.

Let us define

$$\Upsilon(\boldsymbol{k}) = \sum_{i=0}^{2} e^{i\boldsymbol{k}\cdot\boldsymbol{a}_i}. \tag{2.37}$$

Then

$$H_{XX,\boldsymbol{k}} = \epsilon_0, \tag{2.38}$$
$$H_{A,B,\boldsymbol{k}} = -\gamma_0 \Upsilon(\boldsymbol{k}), \tag{2.39}$$
$$H_{B,A,\boldsymbol{k}} = -\gamma_0 \Upsilon(\boldsymbol{k})^*, \tag{2.40}$$
$$S_{XX,\boldsymbol{k}} = 1, \tag{2.41}$$
$$S_{A,B,\boldsymbol{k}} = \Upsilon(\boldsymbol{k}) s_0 \tag{2.42}$$
$$S_{B,A,\boldsymbol{k}} = \Upsilon(\boldsymbol{k})^* s_0. \tag{2.43}$$

Therefore we can rewrite Eq. (2.26) as

$$\begin{pmatrix} \epsilon_0 - \epsilon_{\boldsymbol{k}} & (-\gamma_0 - s_0\epsilon_{\boldsymbol{k}})\Upsilon(\boldsymbol{k}) \\ (-\gamma_0 - s_0\epsilon_{\boldsymbol{k}})\Upsilon(\boldsymbol{k})^* & \epsilon_0 - \epsilon_{\boldsymbol{k}} \end{pmatrix} \begin{pmatrix} \alpha \\ \beta \end{pmatrix} = \begin{pmatrix} 0 \\ 0 \end{pmatrix}. \tag{2.44}$$

It is seen that ϵ_0 enters as a constant term, so it has no influence on the eigenstates, and only shifts the whole band structure. Therefore it can be set to zero. Eq. (2.44) only has non-trivial solutions for α and β if the determinant of the matrix equals zero, which leads to

$$\epsilon_{\boldsymbol{k}}^{\pm} = \pm \frac{\gamma_0 |\Upsilon(\boldsymbol{k})|}{1 \mp s_0 |\Upsilon(\boldsymbol{k})|}. \tag{2.45}$$

Inserting this in the first row of Eq. (2.44), the eigenstates are found,

$$\frac{\alpha}{\beta} = -\frac{(\epsilon_{\boldsymbol{k}} s_0 + \gamma_0)\Upsilon(\boldsymbol{k})}{\epsilon_{\boldsymbol{k}}}. \tag{2.46}$$

Inserting $\epsilon_{\boldsymbol{k}}^{\pm}$ from Eq. (2.45),

$$\frac{\alpha}{\beta} = \Upsilon(\boldsymbol{k}) \frac{\gamma_0 + \frac{\pm\gamma_0 s_0 |\Upsilon(\boldsymbol{k})|}{1 \mp s_0 |\Upsilon(\boldsymbol{k})|}}{\mp \frac{\gamma_0 |\Upsilon(\boldsymbol{k})|}{1 \mp s_0 |\Upsilon(\boldsymbol{k})|}} = \mp \frac{\Upsilon(\boldsymbol{k})}{|\Upsilon(\boldsymbol{k})|}. \tag{2.47}$$

We choose

$$\begin{pmatrix} \alpha \\ \beta \end{pmatrix} = \frac{1}{\sqrt{2}} \begin{pmatrix} \mp \frac{\Upsilon(\boldsymbol{k})}{|\Upsilon(\boldsymbol{k})|} \\ 1 \end{pmatrix}. \tag{2.48}$$

This gives the band structure depicted in figure Fig. 2.2a. It is observed from Eq. (2.45) that $\epsilon_{\boldsymbol{k}}^{+} > 0$ and $\epsilon_{\boldsymbol{k}}^{-} < 0$, so half of the states have negative energies and the other half have positive energies. For neutral graphene the bands are half filled, so the Fermi energy must lie where the upper and lower π-band meet. At $\Upsilon(\boldsymbol{k}) = 0$, $\epsilon_{\boldsymbol{k}}^{+} = \epsilon_{\boldsymbol{k}}^{-} = 0$. These points are called the Dirac points, and their position in $\boldsymbol{k}$-space will be labeled by $\boldsymbol{K}_\tau$, where $\tau = \pm 1$. Since the two bands meet at $\boldsymbol{K}_\tau$, graphene is a conductor. However, since the bands intersect at only two points in the Brillouin zone at the Fermi level, the density of states is zero, so there are almost no conduction electrons. Therefore it is normally

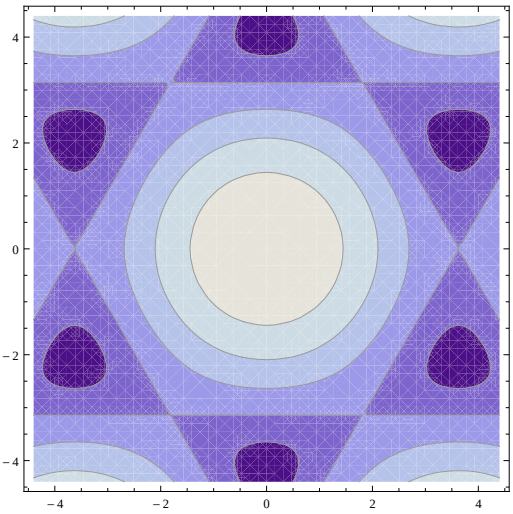

(a) Contour plot of the band structure of graphene. The horizontal axes are in units of $1/a$.

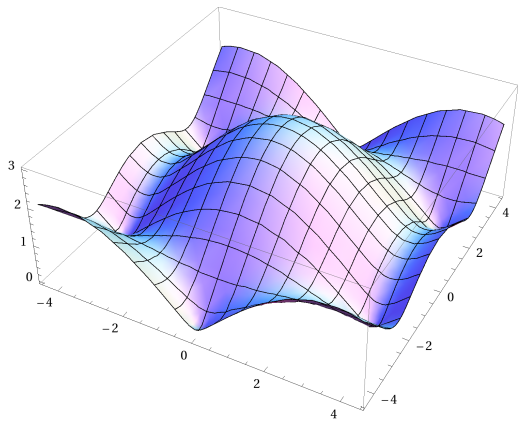

(b) Surface plot of the positive π-band. The height is in units of γ_0, and the horizontal axes are in units of $1/a$.

classified as a semimetal [29, p. 392]. Conventionally the Dirac point $\boldsymbol{k}$-space vectors are not called $\boldsymbol{K}_+$ and $\boldsymbol{K}_-$ but $\boldsymbol{K}$ and $\boldsymbol{K}'$. For calculational simplicity we will keep the notation $\boldsymbol{K}_\tau$ in this chapter, and change to $\boldsymbol{K}(\boldsymbol{K}')$ in the rest of the thesis.

It is seen from Eq. (2.45) that at the Dirac point, the real and imaginary parts of Eq. (2.37) must be zero separately. For the imaginary part of Eq. (2.37) to be zero,

$$\boldsymbol{K}_\tau \cdot \boldsymbol{a}_1 = -\boldsymbol{K}_\tau \cdot \boldsymbol{a}_2 \bmod 2\pi, \tag{2.49}$$

so a solution is $\boldsymbol{K}_\tau$ orthogonal to $\boldsymbol{a}_1 + \boldsymbol{a}_2$,

$$\boldsymbol{K}_\tau \propto \begin{pmatrix} 0 \\ 1 \end{pmatrix}. \tag{2.50}$$

For this $\boldsymbol{K}_\tau$, the real part must satisfy $\cos(\boldsymbol{K}_\tau \cdot \boldsymbol{a}_1) = \cos(\boldsymbol{K}_\tau \cdot \boldsymbol{a}_2) = -\frac{1}{2}$, so

$$\boldsymbol{K}_\tau \cdot \boldsymbol{a}_2 = \pm\frac{2}{3}\pi. \tag{2.51}$$

Therefore

$$\boldsymbol{K}_\tau = \tau\frac{2}{3}\pi\frac{2}{a}\begin{pmatrix} 0 \\ 1 \end{pmatrix} = \tau\frac{4\pi}{3a}\begin{pmatrix} 0 \\ 1 \end{pmatrix}. \tag{2.52}$$

Graphene is symmetric under a $\frac{2}{3}\pi$ rotation, and the band structure must have the same rotational symmetry as the real space lattice, so the $\boldsymbol{K}_\tau$ rotated by $\frac{2}{3}\pi$ also satisfies

$\Upsilon(\boldsymbol{k}) = 0$. Therefore four additional $\boldsymbol{K}_\tau$ points are found, namely

$$\begin{aligned}
\boldsymbol{K}_{\tau,1} &= \tau\frac{4\pi}{3a}\begin{pmatrix} -\frac{\sqrt{3}}{2} \\ -\frac{1}{2} \end{pmatrix} \\
&= \tau\frac{2\pi}{3a}\begin{pmatrix} -\sqrt{3} \\ -1 \end{pmatrix}, \qquad (2.53) \\
\boldsymbol{K}_{\tau,2} &= \tau\frac{2\pi}{3a}\begin{pmatrix} \sqrt{3} \\ -1 \end{pmatrix}. \qquad (2.54)
\end{aligned}$$

It should be noted that these points are not different from the original $\boldsymbol{K}$ and $\boldsymbol{K}'$, but have the same position in neighboring unit cells as the original $\boldsymbol{K}$ and $\boldsymbol{K}'$ have in the original unit cell, i.e. they are related by a reciprocal lattice vector. Since these points are right at the Fermi energy, transport properties are determined by the band structure in their vicinity. Therefore it is useful to Taylor expand the band structure around $\boldsymbol{K}_\tau$.

$$\begin{aligned}
\Upsilon\left(\boldsymbol{K}_\tau + \tilde{\boldsymbol{k}}\right) &= 1 + e^{i(\boldsymbol{K}_\tau+\tilde{\boldsymbol{k}})\cdot\boldsymbol{a}_1} + e^{i(\boldsymbol{K}_\tau+\tilde{\boldsymbol{k}})\cdot\boldsymbol{a}_2} \\
&= e^{i\boldsymbol{K}_\tau\cdot\boldsymbol{a}_1} i\tilde{\boldsymbol{k}}\cdot\boldsymbol{a}_1 + e^{i\boldsymbol{K}_\tau\cdot\boldsymbol{a}_2} i\tilde{\boldsymbol{k}}\cdot\boldsymbol{a}_2, \qquad (2.55) \\
\boldsymbol{K}_\tau\cdot\boldsymbol{a}_1 &= -\tau\frac{2}{3}\pi \qquad (2.56) \\
\boldsymbol{K}_\tau\cdot\boldsymbol{a}_2 &= \tau\frac{2}{3}\pi \qquad (2.57) \\
\Rightarrow e^{i\boldsymbol{K}_\tau\cdot\boldsymbol{a}_1} &= -\frac{1}{2} - \tau i\frac{\sqrt{3}}{2}\pi \qquad (2.58) \\
\Rightarrow e^{i\boldsymbol{K}_\tau\cdot\boldsymbol{a}_2} &= -\frac{1}{2} + \tau i\frac{\sqrt{3}}{2}\pi, \qquad (2.59) \\
\tilde{\boldsymbol{k}}\cdot\boldsymbol{a}_1 &= \frac{a}{2}\left(\sqrt{3}\tilde{k}_x - \tilde{k}_y\right) \quad \text{from Eq. (2.4)} \qquad (2.60) \\
\tilde{\boldsymbol{k}}\cdot\boldsymbol{a}_2 &= \frac{a}{2}\left(\sqrt{3}\tilde{k}_x + \tilde{k}_y\right) \qquad (2.61) \\
\Rightarrow \Upsilon\left(\boldsymbol{K}_\tau + \tilde{\boldsymbol{k}}\right) &= -\left(\frac{1}{2} + \tau i\frac{\sqrt{3}}{2}\pi\right)\frac{a}{2}\left(\sqrt{3}\tilde{k}_x - \tilde{k}_y\right) \\
&\quad + \left(-\frac{1}{2} + \tau i\frac{\sqrt{3}}{2}\pi\right)\frac{a}{2}\left(\sqrt{3}\tilde{k}_x + \tilde{k}_y\right) \\
&= \frac{\sqrt{3}a}{2}\left(-\tilde{k}_x + \tau i\tilde{k}_y\right) \qquad (2.62) \\
\Rightarrow \left|\Upsilon(\boldsymbol{K}_\tau + \tilde{\boldsymbol{k}})\right| &= \frac{\sqrt{3}a}{2}\left|\tilde{\boldsymbol{k}}\right|. \qquad (2.63)
\end{aligned}$$

Inserting this result in the expression for the energy, Eq. (2.45), and expanding to first

order in $|\tilde{\boldsymbol{k}}|$, one obtains

$$\begin{aligned}\epsilon^{\pm}_{\boldsymbol{k}} &= \frac{\pm\gamma_0 \frac{\sqrt{3}a}{2}|\tilde{\boldsymbol{k}}|}{1 \mp s_0 \frac{\sqrt{3}a}{2}|\tilde{\boldsymbol{k}}|} \\ &= \pm\gamma_0 \frac{\sqrt{3}a}{2}\left|\tilde{\boldsymbol{k}}\right|. \end{aligned} \tag{2.64}$$

The energy is thus rotationally symmetric around $\boldsymbol{K}_\tau$, and linear in $|\tilde{\boldsymbol{k}}|$. This is equivalent to the dispersion relation of a massless relativistic particle [7, sec. 3.2], [8, sec. 1], [9], and the band structure is called a Dirac cone, with $\boldsymbol{K}_\tau$ being the Dirac point. The Fermi velocity, equivalent to the speed of a relativistic particle, is

$$v_F = \left|\frac{\epsilon^{\pm}_{\boldsymbol{k}}}{|\tilde{\boldsymbol{k}}|}\right| = \gamma_0 \frac{\sqrt{3}a}{2}. \tag{2.65}$$

From Eqs. (2.44), (2.62) and (2.65), the effective Hamiltonian close to the Dirac point is

$$H = v_F \begin{pmatrix} 0 & \tilde{k}_x - \tau i \tilde{k}_y \\ \tilde{k}_x + \tau i \tilde{k}_y & 0 \end{pmatrix}. \tag{2.66}$$

This Hamiltonian will be the starting point of our calculation of the carbon nanotube band structure in the next chapter.

Chapter 3

Band structure of a carbon nanotube

To a large extend, the band structure of a carbon nanotube can be viewed as a set of one-dimensional slices through the two-dimensional graphene band structure. The direction of the slices is determined by the chirality of the tube. This gives rise to both metallic tubes with no gap, and semiconducting tubes with gaps of the size $1/R \sim 500\,\text{meV}$.

The curvature of the tube induces small overlaps between the σ and π orbitals on neighboring atoms. This shifts the one-dimensional band structure slices by a tiny distance in $\boldsymbol{k}$-space, such that many metallic tubes are no longer metallic, but only nearly metallic, with gaps of $\sim 10\,\text{meV}$. The curvature induced overlaps between the σ and π orbitals also enhances spin-orbit coupling, so the energy bands for spin up and spin down electrons split, with a gap difference of $\sim$0.1meV. The quantization axis of spin lies parallel to the tube axis.

3.1 Geometry

A carbon nanotube can be viewed as a graphene sheet folded into a cylinder, as shown in figure Fig. 3.1. This can be done in several ways. Imagine having a rectangular sheet of graphene, where two of the sides are orthogonal to $\boldsymbol{\tau}_0$. If the sheet is folded such that the two sides orthogonal to $\boldsymbol{\tau}_0$ meet, a cylinder is created. The pattern at the end of the tube is seen in Fig. 3.1, and the tube is named a zig-zag tube due to this pattern. If one choses to fold the two other sides together instead, the tube is called an armchair tube due to the end pattern. It is also possible to have rectangular sheets where none of the sides are parallel to any of the $\boldsymbol{\tau}$'s. They can be folded to a carbon nanotube too, and will give an end pattern which is neither zig-zag nor armchair. These tubes are called chiral nanotubes. Typically, the length of the tube is much larger than the circumference, so one should rather imagine folding a graphene ribbon than a square sheet.

It is convenient to describe the nanotube by a cylindrical coordinate system, where $\hat{\boldsymbol{t}}$ is the unit vector in the axial direction, $\hat{\boldsymbol{c}}$ is the unit vector in the circumferential direction, and $\hat{\boldsymbol{\pi}}$ is the unit vector in the radial direction, such that $\hat{\boldsymbol{\pi}} \times \hat{\boldsymbol{c}} = \hat{\boldsymbol{t}}$. An angle ϕ_c is defined

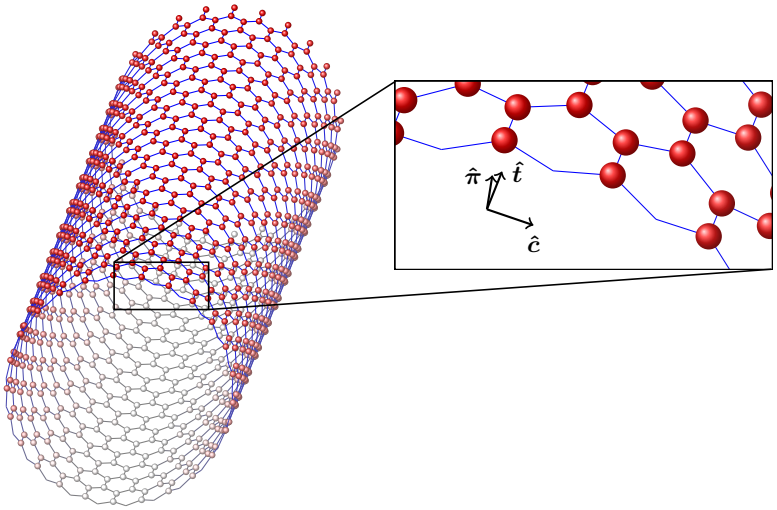

Figure 3.1: A zig-zag carbon nanotube with a radius of 1nm. The box shows the pattern at the end, from which is seen that it is a zig-zag tube. This figure is a modification of the one found in [33].

as the angle from $\hat{\boldsymbol{c}}$ to $\boldsymbol{\tau}_0$. ϕ_c must lie in the interval $[0, \frac{\pi}{6}]$, since we are free to choose any of the $\boldsymbol{\tau}$'s as $\boldsymbol{\tau}_0$, and we can just choose $-\hat{\boldsymbol{c}}$ instead of $\hat{\boldsymbol{c}}$ as our circumferential vector if that makes ϕ_c smaller. An armchair tube thus has $\phi_c = 0$, and a zig-zag tube has $\phi_c = \frac{\pi}{6}$. The chiral angle is conventionally defined as $\eta = \frac{\pi}{6} - \phi_c$.

To quantify both radius and chirality, the chiral vector is introduced. It is defined as the vector going along the short edge of the graphene sheet, so when the sheet is folded, the chiral vector would lie in the circumferential direction, connecting an atom to itself along the circumference. It is thus parallel to $\hat{\boldsymbol{c}}$. Since any lattice vector can be written as an integer linear combination of primitive vectors, we may define

$$\boldsymbol{C} = n\boldsymbol{a}_1 + m\boldsymbol{a}_2, \quad \text{for} \quad m, n \in \mathbb{Z}. \tag{3.1}$$

Since the tube is invariant under changing $\boldsymbol{C}$ to $-\boldsymbol{C}$, or switching m and n, degeneracies are avoided by introducing the additional constraint

$$m \geq |n| \geq 0. \tag{3.2}$$

From the chiral vector we may derive

$$\cos\phi_c = \frac{\boldsymbol{C} \cdot \boldsymbol{\tau}_0}{|\boldsymbol{C}||\boldsymbol{\tau}_0|}, \tag{3.3}$$

$$R = \frac{|\boldsymbol{C}|}{2\pi}, \tag{3.4}$$

where R is the radius. Since both the radius and the chirality can be found from the chiral vector, it contains all information about the geometry of the tube, except for the length. The tube must be smooth all the way around and without any seam where the two edges of the graphene sheet are connected, so m, n have to be integers. This means that only some combinations of chirality and radius are possible.

3.2 Band structure

In Section 2.2 it was seen that the entire graphene lattice could be generated by the primitive vectors via two translation operators. This can also be done for the tube, but now the operators do not generate translations, but helical rotations. The Hamiltonian is formally the same as for graphene Eq. (2.20),

$$H = T + \sum_{i}^{N} (V_{A_i} + V_{B_i}), \tag{3.5}$$

but the potentials are now not fixed on a flat lattice, but on a cylinder. Therefore the 2-dimensional discrete translational symmetry that justified the use of Bloch's theorem is broken. However two new helical symmetries arise instead, making it possible to still use Bloch's theorem. Let us define θ as the angle rotated along the $\hat{\boldsymbol{c}}$ direction, so for a vector $\boldsymbol{x} = x_c\hat{\boldsymbol{c}} + t\hat{\boldsymbol{t}} + R\hat{\boldsymbol{\pi}}$ it is given as $\theta = \frac{x_c}{R}$. We may then define the generator of rotations, $\mathcal{R}(\theta)$, which rotates the whole system an angle θ, and a generator of translations, $\mathcal{T}(t)$, which translates the whole system a distance t in the $\hat{\boldsymbol{t}}$ direction. It is seen that for some specific combinations of θ and t, corresponding to lattice vectors of graphene, the tube is rotated and translated into itself. Since the Coulomb potential is rotationally symmetric, the Hamiltonian Eq. (3.5) is invariant under the operation

$$\mathcal{R}(\theta)^{-1}\mathcal{T}(t)^{-1} H \mathcal{T}(t)\mathcal{R}(\theta) = H. \tag{3.6}$$

3.2.1 Discretized k-vectors

If we neglect curvature effects, the carbon nanotube Hamiltonian is identical to the graphene Hamiltonian. Therefore they must have the same eigenstates. However, the wavefunction on the cylinder has to be periodic in the circumferential direction with the circumference as period, so that it is continuous and differentiable everywhere. The wavefunction Eq. (2.24) satisfies this condition if

$$\boldsymbol{k} \cdot \boldsymbol{C} = 2\pi n, \quad n \in \mathbb{N}. \tag{3.7}$$

For an infinite graphene sheet, there is a quantum state for each $\boldsymbol{k} \in \mathbb{R}^2$. For an infinitely long carbon nanotube, there will still be a continuum of allowed states in the $\hat{\boldsymbol{t}}$ direction, while the allowed states in the $\hat{\boldsymbol{c}}$ direction will be spaced with a distance $\frac{1}{R}$, as seen from Eq. (3.7). The band structure will thus be 1-dimensional slices of the graphene band structure, as seen in figure Fig. 3.2. Since wave vectors outside the Brillouin zone are redundant, there will only be a finite number of wave vectors in the $\hat{\boldsymbol{c}}$ direction. The Hamiltonian near a Dirac point is thus

$$H = v_F \begin{pmatrix} 0 & k_c - \tau i k \\ k_c + \tau i k & 0 \end{pmatrix}, \tag{3.8}$$

where k_c is a wave vector in the $\hat{\boldsymbol{c}}$ direction, and k is a wave vector in the $\hat{\boldsymbol{t}}$ direction. For armchair, some zig-zag and some chiral tubes $k_c = 0$, meaning that one of the 1-dimensional bands passes through the Dirac point [31]. In this case the band structure

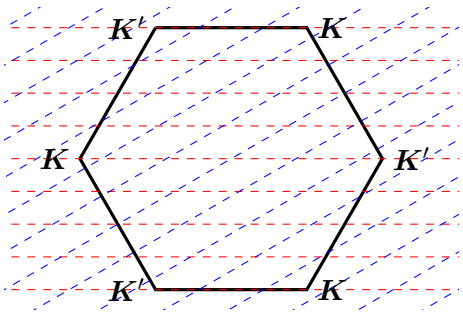

Figure 3.2: The discretization of the band structure due to the finite circumference. The hexagon is the graphene Brillouin zone, and the red and blue lines show where the one-dimensional nanotube band structure lies in the two-dimensional graphene band structure. The red lines are an (m,n)=(4,4) armchair nanotube, which has $R = 0.271\,\text{nm}$. The lines hit the Dirac points, so the tube is metallic, like all armchair tubes. The blue lines are an (m,n)=(7,0) zig-zag nanotube with $R = 0.274\,\text{nm}$. The lines do not cross the Dirac points, so this tube is semiconducting.

is a 1-dimensional Dirac cone. More specifically, the criterion for a tube being metallic is [31, p. 33]

$$\frac{2n+m}{3} \in \mathbb{Z}. \tag{3.9}$$

Some tubes have a finite k_c, giving the energy spectrum

$$\epsilon_k^{\pm} = \pm v_F \sqrt{k_c^2 + k^2}. \tag{3.10}$$

The band structure is thus gapped, giving a hyperbola instead of linear dispersion. Like Eq. (2.64) was equivalent to the dispersion for a massless Dirac fermion in two dimensions, Eq. (3.10) is the dispersion of a one-dimensional massive Dirac fermion.

3.2.2 Non-orthogonal π- and σ-orbitals

When the transformation of the wave function from a flat graphene sheet to a cylinder is performed, the π-orbitals point in the radial direction, while the σ-orbitals lie parallel to the surface of the cylinder. Due to the curvature, a π-orbital on one atom is neither parallel to the π-orbitals nor orthogonal to the σ-orbitals on neighboring atoms. This means that the value of γ_0 from Eq. (2.35) is changed, and that the π- and σ-bands mix. Izumida et al. [12] have shown that this gives rise to a shift in $\boldsymbol{k}$ space of the one-dimensional bands. We will now outline their calculation. It is similar to the calculation of the graphene bandstructure in Section 2.3, except that instead of only having a 2×2 Hamiltonian containing two π-orbitals as in Eq. (2.26), it is necessary to include all four orbitals on each atom, so the Hamiltonian will be 8×8.

In the following we will enumerate the unit cells by the index l, and whether an atom is an A or a B atom by X. The four orbitals s, p_x, p_y, p_π will be described by the index j.

Instead of the momentum k_c we will use $\mu = k_c R$, such that μ takes integer values. This means that $k_c x_c = \mu\theta$. The basis is chosen as

$$|jX\boldsymbol{k}\rangle = \frac{1}{\sqrt{N}} \sum_l e^{ikt_l + i\mu\theta_l} |\phi_{jXl}\rangle, \tag{3.11}$$

where N is the number of unit cells, t_l and θ_l are the t and θ coordinates of the l'th unit cell, and $|\phi_{jXl}\rangle$ is the j orbital on the X, l site. Equivalent to Eq. (2.24), the Hamiltonian is diagonal in $\boldsymbol{k}$-space, so it only has to be diagonalized in j, X space. This is done similar to Eqs. (2.29)-(2.33), so

$$\begin{aligned} \langle jX\boldsymbol{k}|H|j'X'\boldsymbol{k}\rangle &= \sum_l e^{-ikt_l - i\mu\theta_l} \langle \phi_{jXl}|H|\phi_{j'X'l'=0}\rangle \\ &\equiv \sum_l e^{-ikt_l - i\mu\theta_l} H^{XX'}_{j,j',l}. \end{aligned} \tag{3.12}$$

The states of Eq. (3.11) are not orthogonal, but a finite overlap

$$\begin{aligned} \langle jX\boldsymbol{k}|j'X'\boldsymbol{k}\rangle &= \sum_l e^{-ikt_l - i\mu\theta_l} \langle \phi_{jXl}|\phi_{j'X'l'=0}\rangle \\ &\equiv \sum_l e^{-ikt_l - i\mu\theta_l} S^{XX'}_{j,j',l}. \end{aligned} \tag{3.13}$$

The sum over l runs in principle over all unit cells, but only for neighbouring atoms do Eqs. (3.12) and (3.13) give a non-zero inner product. Therefore for $l \neq 0$, $S^{XX'}_{j,j',l}$ and $H^{XX'}_{j,j',l}$ are zero unless $X' \neq X$. Similar to Eq. (2.44), the matrix equation

$$\left(\overline{\overline{H}} - \epsilon_{\boldsymbol{k}} \overline{\overline{S}}\right) \boldsymbol{C} = 0 \tag{3.14}$$

is found, where $\overline{\overline{H}}$ and $\overline{\overline{S}}$ are the matrices for which Eqs. (3.12) and (3.13) are the elements.

$H_{jX,j'X'}$ and $S_{jX,j'X'}$ can be found from the graphene hopping parameters and geometrical considerations. In addition to H_π and S_π, Eqs. (2.35) and (2.36), it is also necessary to introduce the remaining graphene hopping parameters,

$$H_\tau = \langle p^X_\tau(0)|(T + V_X(0) + V_{\bar{X}}(0))|p^{\bar{X}}_\tau(0)\rangle = 5.037\text{eV} \tag{3.15}$$

$$S_\tau = \langle p^X_\tau(0)|p^{\bar{X}}_\tau(0)\rangle = -0.146 \tag{3.16}$$

$$H_{s\tau} = \langle s^B(0)|(T + V_X(0) + V_{\bar{X}}(0))|p^A_\tau(0)\rangle = -5.580\text{eV} \tag{3.17}$$

$$S_{s\tau} = \langle s^B(0)|p^A_\tau(0)\rangle = -\langle s^A(0)|p^B_\tau(0)\rangle = 0.102 \tag{3.18}$$

$$H_{ss} = \langle s^X(0)|(T + V_X(0) + V_{\bar{X}}(0))|s^{\bar{X}}(0)\rangle = -6.769\text{eV} \tag{3.19}$$

$$S_{ss} = \langle s^X(0)|s^{\bar{X}}(0)\rangle = 0.212 \tag{3.20}$$

$$\epsilon_s = \langle s^X(0)|(T + V_X(0))|s^X(0)\rangle = -8.868\text{eV}. \tag{3.21}$$

Here τ denotes a p-orbital along $\boldsymbol{\tau}_0$. The numerical values are given by the table in [30, p. 32]. The diagonal terms of $S^{XX'}_{j,j',l}$, meaning $j = j'$ and $X = X'$, are equal to 1. From the choice $\epsilon_p = 0$ in Section 2.3, the diagonal terms of $H^{XX'}_{j,j',l}$ are zero, except for

$$H^{XX}_{s,s,0} = \epsilon_s. \tag{3.22}$$

To calculate the off-diagonal terms $H^{X\bar{X}}_{j,j',l}$ and $S^{X\bar{X}}_{j,j',l}$, we exploit the fact that p-orbitals can be decomposed into orthogonal components, Eq. (2.16). In Section 2.3 it was shown that a π-orbital is orthogonal to both the p- and s-component of the σ-orbital on the neighbouring atom in the $\boldsymbol{\tau}$ direction. Therefore, in the calculation of $H_{s\tau}$ and $S_{s\tau}$, the only part of the p-orbital that contributes is the projection onto $\boldsymbol{\tau_0}$. If we define a unit vector $\hat{\boldsymbol{n}}^X_{jl}$ as being the direction of the p-orbital labeled j on the X atom in the l'th unit cell, we may write

$$H^{BA}_{s,p_j,l} = -H^{AB}_{s,p_j,l} = \hat{\boldsymbol{n}}^A_{j0} \cdot \hat{\boldsymbol{\tau}}_l H_{s\tau}, \tag{3.23}$$

$$S^{BA}_{s,p_j,l} = -S^{AB}_{s,p_j,l} = \hat{\boldsymbol{n}}^A_{j0} \cdot \hat{\boldsymbol{\tau}}_l, \tag{3.24}$$

where $\hat{\boldsymbol{\tau}}_l$ is a unit vector going from the A_0- to the B_l-atom, so

$$\hat{\boldsymbol{\tau}}_l = \frac{\boldsymbol{\tau}_l}{a_{\mathrm{C-C}}}. \tag{3.25}$$

To calculate $H^{BA}_{p_i,p_j,l}$ and $S^{BA}_{p_i,p_j,l}$, we define a coordinate system where

$$\hat{\boldsymbol{n}}^A_{i0} = n^A_{i0,\tau}\hat{\boldsymbol{\tau}}_{\boldsymbol{l}} + n^A_{i0,x}\hat{\boldsymbol{x}}, \tag{3.26}$$

$$\hat{\boldsymbol{n}}^B_{jl} = n^B_{jl,\tau}\hat{\boldsymbol{\tau}}_{\boldsymbol{l}} + n^B_{jl,x}\hat{\boldsymbol{x}} + n^B_{jl,y}\hat{\boldsymbol{y}}. \tag{3.27}$$

There will be two terms, one proportional to H_τ and one proportional to H_π. The σ-term comes from the part parallel to $\boldsymbol{\tau_l}$, so it has the form

$$n^A_{i0,\tau} n^B_{j0,\tau} H_\tau. \tag{3.28}$$

The π-term must come from the projection onto the plane orthogonal to $\boldsymbol{\tau}$, and herein only from the part where $\hat{\boldsymbol{n}}^A_{i0}$ and $\hat{\boldsymbol{n}}^B_{jl}$ are parallel. Therefore it has the form

$$n^A_{i0,x} n^B_{jl,x} H_\pi. \tag{3.29}$$

To get it in coordinate independent form, we write

$$n^A_{i0,x} n^B_{jl,x} = \hat{\boldsymbol{n}}^A_{i0} \cdot \hat{\boldsymbol{n}}^B_{jl} - n^A_{i0,\tau} n^B_{jl,\tau}, \tag{3.30}$$

$$n^A_{i0,\tau} n^B_{jl,\tau} = \left(\hat{\boldsymbol{n}}^A_{i0} \cdot \hat{\boldsymbol{\tau}}_l\right)\left(\hat{\boldsymbol{n}}^B_{jl} \cdot \hat{\boldsymbol{\tau}}_l\right). \tag{3.31}$$

Therefore

$$H^{BA}_{p_i,p_j,l} = H^{AB}_{p_i,p_j,l} = \hat{\boldsymbol{n}}^A_{i0} \cdot \hat{\boldsymbol{n}}^B_{jl} H_\pi + \left(\hat{\boldsymbol{n}}^A_{i0} \cdot \hat{\boldsymbol{\tau}}_l\right)\left(\hat{\boldsymbol{n}}^B_{jl} \cdot \hat{\boldsymbol{\tau}}_l\right)\left(H_\tau - H_\pi\right), \tag{3.32}$$

$$S^{BA}_{p_i,p_j,l} = S^{AB}_{p_i,p_j,l} = \hat{\boldsymbol{n}}^A_{i0} \cdot \hat{\boldsymbol{n}}^B_{jl} S_\pi + \left(\hat{\boldsymbol{n}}^A_{i0} \cdot \hat{\boldsymbol{\tau}}_l\right)\left(\hat{\boldsymbol{n}}^B_{jl} \cdot \hat{\boldsymbol{\tau}}_l\right)\left(S_\tau - S_\pi\right). \tag{3.33}$$

To link it to the parameters of the tube, ϕ_c and R, we will write the vectors in the $\hat{\boldsymbol{c}}, \hat{\boldsymbol{t}}, \hat{\boldsymbol{\pi}}$ basis at atom A in the zeroth unit cell, so

$$\hat{\boldsymbol{n}}^A_{c0} = (1, 0, 0) \tag{3.34}$$
$$\hat{\boldsymbol{n}}^A_{t0} = (0, 1, 0) \tag{3.35}$$
$$\hat{\boldsymbol{n}}^A_{\pi 0} = (0, 0, 1) \tag{3.36}$$
$$\hat{\boldsymbol{n}}^B_{cl} = (\cos\theta_l, 0, -\sin\theta_l) \tag{3.37}$$
$$\hat{\boldsymbol{n}}^B_{tl} = (0, 1, 0) \tag{3.38}$$
$$\hat{\boldsymbol{n}}^B_{\pi l} = (\sin\theta_l, 0, \cos\theta_l) \tag{3.39}$$
$$\tau_l = (R\sin\theta_l, t_l, R(\cos\theta_l - 1)). \tag{3.40}$$

t_l and θ_l can be expressed by ϕ_c and $a_{\mathrm{C-C}}$ as

$$t_l = -a_{\mathrm{C-C}}\sin(\phi_c + \delta_l), \tag{3.41}$$
$$\theta_l = \frac{a_{\mathrm{C-C}}}{R}\cos(\phi_c + \delta_l), \tag{3.42}$$

where $\delta_l = (0, \frac{\pi}{3}, -\frac{\pi}{3})$ for $l = 0, 1, 2$. The minus sign in Eq. (3.41) is pure convention [12]. Finding the band structure is now just a matter of inserting everything in Eq. (3.14), and diagonalizing. However, we want to include one more effect, namely spin-orbit coupling.

3.2.3 Spin-orbit coupling

To include spin-orbit interactions, the atomic spin-orbit operator [10, sec. 6.3.2],

$$H_{\mathrm{so}} = \frac{1}{2}V_{\mathrm{so}}\sum_l \boldsymbol{L}_l \cdot \boldsymbol{S}, \tag{3.43}$$

is added to H. Here $\boldsymbol{S}$ is the spin operator, $\boldsymbol{L}_l$ is the angular momentum operator at the l'th atomic site, and V_{so} is the atomic spin-orbit coupling strength. It is found experimentally as the energy difference between two almost identical atomic states, where only one electron in a p orbital has different spin in the two states [2]. Its value is [34],

$$V_{\mathrm{so}} = 7.8\,\mathrm{meV}. \tag{3.44}$$

This form of H_{so} is just an approximation to the exact spin-orbit operator, so let us briefly discuss which approximations are used. If there were only a single atom and not a lattice, the electron would be in some orbital. In this case the atomic spin-orbit operator can be derived from the electrodynamics of the motion of the electron in the orbital to have the form Eq. (3.43). In the tight-binding approximation, which is the method used in this and the previous chapter, the electron is bound in orbitals around all the nuclei. In this approximation the orbitals are not distorted by neighbouring nuclei, meaning that an electron in one orbital cannot feel the electric field of nearby nuclei. The spin-orbit Hamiltonian generated by the motion in the orbital at the l'th atom is therefore $\frac{1}{2}V_{\mathrm{so}}\boldsymbol{L}_l \cdot \boldsymbol{S}$.

Since the electron is in a superposition of the orbitals at all the nuclei, the spin-orbit operator contains the term given in Eq. (3.43). If the electron could feel the electric field of neighboring atoms, there would be additional terms in the spin-orbit Hamiltonian, but since this is not the case in the tight-binding approximation, we use Eq. (3.43).

The dot product $\boldsymbol{L}_l \cdot \boldsymbol{S}$ is rotationally invariant, and the sum over l ensures that H_{so} does not break the helical symmetry. Therefore it does not violate the Bloch condition, Eq. (3.6). However it does break spin degeneracy. Therefore it is necessary to include spin explicitly in the calculations, thus going from 8 to 16 states in Eq. (3.14). The naive way of adding spin to the state would be

$$|jXs\boldsymbol{k}\rangle = |jX\boldsymbol{k}\rangle|s\rangle, \tag{3.45}$$

where s is quantized in the $\hat{\boldsymbol{t}}$ direction. As we will see, this state is not a Bloch state. The only way a Bloch state can change under a rotation around the tube axis is by getting multiplied by a phase, as in Eq. (2.23). If a rotation by θ is performed, the spin gets a phase [13, p. 172], so

$$\mathcal{R}(\theta)|s\rangle = \exp\left(-i\frac{s\theta}{2}\right)|s\rangle, \tag{3.46}$$

where $s = 1$ for spin up and $s = -1$ for spin down. This means that

$$\mathcal{R}(\theta)(|\uparrow\rangle + |\downarrow\rangle) = \alpha_\theta|\uparrow\rangle + \alpha_\theta^*|\downarrow\rangle = \alpha_\theta(|\uparrow\rangle + \alpha_{2\theta}^*|\downarrow\rangle), \tag{3.47}$$

where $\alpha_\theta = \exp(-i\frac{\theta}{2})$. This clearly does not satisfy the Bloch and continuity condition

$$\mathcal{R}(\theta)|\psi\rangle = e^{in_\psi\theta}|\psi\rangle, \tag{3.48}$$

where n_ψ is some integer. Therefore a different set of spin states has to be chosen. Let us construct a state which is invariant under rotation. This can be achieved using local spin states which point in the $\hat{\boldsymbol{t}}$ direction,

$$|s_l\rangle = \mathcal{R}(\theta_l)|s\rangle = \exp\left(-i\frac{s\theta_l}{2}\right)|s\rangle, \tag{3.49}$$

so

$$|jX\tilde{s}\boldsymbol{k}\rangle = \frac{1}{\sqrt{N_s}}\sum_l e^{ikt_l + i(\mu+\frac{s}{2})\theta_l}|\phi_{jXl}\rangle|s_l\rangle, \tag{3.50}$$

$$|jX-\tilde{s}\boldsymbol{k}\rangle = \frac{1}{\sqrt{N_s}}\sum_l e^{ikt_l + i(\mu-\frac{s}{2})\theta_l}|\phi_{jXl}\rangle|-s_l\rangle, \tag{3.51}$$

where we have renamed the spin state to $\tilde{s}$, to remember that it is not homogeneous in space, but gets a phase when travelling around the tube. For shortening the notation, this will be written as

$$|jX\tilde{s}\boldsymbol{k}\rangle = \frac{1}{\sqrt{N_s}}\sum_l e^{ikt_l + iJ\theta_l}|\phi_{jXl}\rangle|s_l\rangle, \tag{3.52}$$

where

$$J = \mu + \frac{s}{2}. \tag{3.53}$$

This is finally a Bloch state fullfilling the helical symmetry, since

$$\mathcal{T}(t)\mathcal{R}(\theta)|jX\tilde{s}\boldsymbol{k}\rangle = e^{-ikt-iJ\theta}|jX\tilde{s}\boldsymbol{k}\rangle. \tag{3.54}$$

This new 16 state basis changes the overlap matrix elements calculated in Section 3.2.2. The diagonal elements are unchanged, since $\langle s_l|s_l\rangle = 1$. There is no overlap between spin up and spin down states on neighboring atoms, since they are quantized in the $\hat{\boldsymbol{t}}$ direction, so their direction is unchanged by rotation around the tube. For neighboring atoms with the same spin direction, a phase is achieved, because

$$\langle s_l|s_{l=0}\rangle = \exp\left(i\frac{s\theta_l}{2}\right). \tag{3.55}$$

Therefore the overlaps are changed from Eqs. (3.12) and (3.13), to

$$\langle jX\tilde{s}\boldsymbol{k}|H|j'X'\tilde{s}\boldsymbol{k}\rangle = \sum_l \exp\left(i\frac{s\theta_l}{2}\right) e^{-ikt_l-iJ\theta_l} H^{XX'}_{j,j',l}, \tag{3.56}$$

$$\langle jX\tilde{s}\boldsymbol{k}|j'X'\tilde{s}\boldsymbol{k}\rangle = \sum_l \exp\left(i\frac{s\theta_l}{2}\right) e^{-ikt_l-iJ\theta_l} S^{XX'}_{j,j',l}. \tag{3.57}$$

In addition to this changed overlap matrix, there is also H_{so}, Eq. (3.43). Let us write it in this basis. As discussed in the beginning of this section, this form of spin-orbit coupling does not take neighboring atoms into account. Therefore the spin-orbit operator must be diagonal in AB-space, so all off-diagonal terms are set to zero. It is thus only necessary to calculate the local matrix elements. The s-orbital has zero angular momentum, so H_{so} on this state gives zero. In the $|\phi_c\uparrow\rangle, |\phi_t\uparrow\rangle, |\phi_\pi\uparrow\rangle, |\phi_c\downarrow\rangle, |\phi_t\downarrow\rangle, |\phi_\pi\downarrow\rangle$ basis, a small calculation following the definitions in [10, sec. 4.3] gives

$$\overline{\overline{H}}_{\mathrm{so}} = \frac{V_{\mathrm{so}}}{2}\begin{pmatrix} 0 & -i & 0 & 0 & 0 & 1 \\ i & 0 & 0 & 0 & 0 & -i \\ 0 & 0 & 0 & -1 & i & 0 \\ 0 & 0 & -1 & 0 & i & 0 \\ 0 & 0 & -i & -i & 0 & 0 \\ 1 & i & 0 & 0 & 0 & 0 \end{pmatrix}. \tag{3.58}$$

Having now the full Hamiltonian and overlap matrix, it is possible to solve Eq. (3.14) to find the band structure. This was done numerically by Izumida et al. [12]. As expected, the curvature and spin-orbit effects are small, so the band structure is very similar to the original graphene band structure. One major difference is however that curvature and spin-orbit induced gaps open at the Dirac points. This can be modelled by an effective π-band Hamiltonian near the Dirac points.

3.2.4 Effective Hamiltonian

We will now show that the band structure near the Fermi level can be described by an effective π-band structure modified by coupling to the σ-bands through second order perturbation theory. We will first explain the method heuristically, and then give the explicit effective Hamiltonian. The graphene Hamiltonian found in Chapter 2 can be written as

$$\overline{\overline{H}}^{\mathrm{G}} = \begin{pmatrix} \overline{\overline{H}}_{\pi}^{\mathrm{G}} & \overline{\overline{0}} \\ \overline{\overline{0}} & \overline{\overline{H}}_{\sigma}^{\mathrm{G}} \end{pmatrix}. \tag{3.59}$$

This is just a way of expressing that there is no mixing of the π- and σ-subspaces. The carbon nanotube Hamiltonian, in the same notation, is

$$\overline{\overline{H}}^{\mathrm{CNT}} = \begin{pmatrix} \overline{\overline{H}}_{\pi}^{\mathrm{CNT}} & \overline{\overline{H}}_{\pi\sigma}^{\mathrm{CNT}} + \overline{\overline{H}}_{\mathrm{so},\pi\sigma} \\ (\overline{\overline{H}}_{\pi\sigma}^{\mathrm{CNT}} + \overline{\overline{H}}_{\mathrm{so},\pi\sigma})^{\dagger} & \overline{\overline{H}}_{\sigma}^{\mathrm{CNT}} + \overline{\overline{H}}_{\mathrm{so},\sigma} \end{pmatrix}. \tag{3.60}$$

We will show that

$$\overline{\overline{H}}^{\mathrm{CNT}} = \overline{\overline{H}}^{\mathrm{G}} + \overline{\overline{H}}', \tag{3.61}$$

where $\overline{\overline{H}}'$ is of the order $(a_{\mathrm{C-C}}/R)^2\overline{\overline{H}}^{\mathrm{G}}$. $\frac{a_{\mathrm{C-C}}}{R}$ is of the order of $0.1 - 0.3$ for small radius tubes, so treating $\overline{\overline{H}}'$ as a perturbation is a good approximation. The reason why there is no $H_{\mathrm{so},\pi}$ term is that the spin-orbit Hamiltonian Eq. (3.58) does not have any diagonal terms, so it does not couple an orbital to itself, and it does not couple neighboring atoms. The other spin-orbit terms are of the size $V_{\mathrm{so}} = 8\,\mathrm{meV}$ [34], so three orders of magnitude smaller than the graphene hopping parameters Eqs. (3.15)-(3.21). Therefore it can be treated perturbatively. The diagonal terms of $\overline{\overline{H}}_{\pi}^{\mathrm{CNT}}$ and $\overline{\overline{H}}_{\sigma}^{\mathrm{CNT}}$ are identical to the diagonal terms of $\overline{\overline{H}}_{\pi}^{\mathrm{G}}$ and $\overline{\overline{H}}_{\sigma}^{\mathrm{G}}$ respectively, since the curvature has no local effect on an individual atom. The off-diagonal terms are given by $H_{j,j',l}^{X\bar{X}}$, which are expressed in Eqs. (3.23) and (3.32) by the inner products between the orbital vectors $\hat{\boldsymbol{n}}_{jl}^{X}$ and $\hat{\boldsymbol{\tau}}_l$. For the π-subspace,

$$H_{p_\pi,p_\pi,l}^{BA} = \hat{\boldsymbol{n}}_{\pi 0}^{A} \cdot \hat{\boldsymbol{n}}_{\pi l}^{B} H_\pi + \left(\hat{\boldsymbol{n}}_{\pi 0}^{A} \cdot \hat{\boldsymbol{\tau}}_l\right)\left(\hat{\boldsymbol{n}}_{\pi l}^{B} \cdot \hat{\boldsymbol{\tau}}_l\right)\left(H_\tau - H_\pi\right). \tag{3.62}$$

From the specific form of the geometrical unit vectors Eqs. (3.34)–(3.40), it is seen that

$$\hat{\boldsymbol{n}}_{\pi 0}^{A} \cdot \hat{\boldsymbol{n}}_{\pi l}^{B} \approx 1 - \theta_l^2, \tag{3.63}$$

$$\left(\hat{\boldsymbol{n}}_{\pi 0}^{A} \cdot \hat{\boldsymbol{\tau}}_l\right)\left(\hat{\boldsymbol{n}}_{\pi l}^{B} \cdot \hat{\boldsymbol{\tau}}_l\right) \approx \theta_l^2. \tag{3.64}$$

From Eq. (3.42),

$$\theta_l \leq \frac{a_{\mathrm{C-C}}}{R}, \tag{3.65}$$

so

$$\overline{\overline{H}}_{\pi}^{\mathrm{CNT}} = \overline{\overline{H}}_{\pi}^{\mathrm{G}} + \overline{\overline{H}}'_{\pi}, \tag{3.66}$$

where $\overline{\overline{H}}'_{\pi} \sim (a_{\mathrm{C-C}}/R)^2$ as required. A similar result can be easily shown for $\overline{\overline{H}}_{\sigma}^{\mathrm{CNT}}$. For the off-diagonal part of Eq. (3.60), also using the result from Eq. (3.23), we find

$$H^{BA}_{p_\pi,p_\tau,l} = \hat{\boldsymbol{n}}^A_{\pi 0} \cdot \hat{\boldsymbol{n}}^B_{\tau l} H_\pi + \left(\hat{\boldsymbol{n}}^A_{\pi 0} \cdot \hat{\boldsymbol{\tau}}_l\right)\left(\hat{\boldsymbol{n}}^B_{\tau l} \cdot \hat{\boldsymbol{\tau}}_l\right)(H_\tau - H_\pi), \tag{3.67}$$

$$H^{BA}_{s,p_\pi,l} = \hat{\boldsymbol{n}}^A_{\pi 0} \cdot \hat{\boldsymbol{\tau}}_l H_{s\tau}, \tag{3.68}$$

which both are given by

$$\hat{\boldsymbol{n}}^A_{\pi 0} \cdot \hat{\boldsymbol{n}}^B_{\tau l} \approx \theta_l, \tag{3.69}$$

$$\hat{\boldsymbol{n}}^A_{\pi 0} \cdot \hat{\boldsymbol{\tau}}_l \approx \theta_l, . \tag{3.70}$$

Therefore

$$\overline{\overline{H}}_{\pi\sigma}^{\mathrm{CNT}} = \bar{\bar{0}} + \overline{\overline{H}}'_{\pi\sigma}, \tag{3.71}$$

where $\overline{\overline{H}}'_{\pi\sigma} \sim a_{\mathrm{C-C}}/R$. An off-diagonal part that is linear in $a_{\mathrm{C-C}}/R$ leads to corrections to energies of order $(a_{\mathrm{C-C}}/R)^2$, since it enters in second and not in first order perturbation theory. It is thus seen that Eq. (**??**) is fullfilled and that $\overline{\overline{H}}'$ is small. Therefore it can be seen as a perturbation to the graphene π band Hamiltonian. $\overline{\overline{H}}'_{\pi}$ can be included exactly, which gives a modification of the parameter H_π proportional to $(a_{\mathrm{C-C}}/R)^2$. The off-diagonal term $\overline{\overline{H}}'_{\pi\sigma} + \overline{\overline{H}}_{\mathrm{so},\pi\sigma}$ has to be included in second order perturbation theory. It will thus modify the band structure as $(\overline{\overline{H}}'_{\pi\sigma} + \overline{\overline{H}}_{\mathrm{so},\pi\sigma})^2$, so there will be three kinds of terms, $(a_{\mathrm{C-C}}/R)^2$, $(a_{\mathrm{C-C}}/R)V_{\mathrm{so}}$, and V_{so}^2. Since V_{so} is about two orders of magnitude smaller than $a_{\mathrm{C-C}}/R$, the term V_{so}^2 will be neglected. One could also argue that $(a_{\mathrm{C-C}}/R)V_{\mathrm{so}}$ is negligible, but since the spin-orbit coupling is the only effect breaking spin degeneracy, this term contains important qualitative behavior and cannot be neglected.

The graphene Hamiltonian is given by Eq. (3.8). We will be concerned with metallic tubes, i.e. $k_c = 0$, so

$$\overline{\overline{H}}_{\pi}^{\mathrm{G}} = \tau v_F k \sigma_2, \tag{3.72}$$

where σ_2 is the second Pauli matrix in the A, B basis, and $\tau = +(-)1$ corresponds to being close to $\boldsymbol{K}(\boldsymbol{K}')$. Performing second order perturbation theory as mentioned above gives the effective Hamiltonian

$$\overline{\overline{H}}_{\pi}^{\mathrm{eff}} = \overline{\overline{H}}_{\pi}^{\mathrm{G}} + \overline{\overline{H}}_{\pi,\mathrm{soc}}^{\mathrm{eff}} + \overline{\overline{H}}_{\pi,\mathrm{cv}}^{\mathrm{eff}}, \tag{3.73}$$

where [12]

$$\overline{\overline{H}}_{\pi,\mathrm{soc}}^{\mathrm{eff}} = v_F \left(\frac{\epsilon_{\mathrm{soc}}^{(\tau)} s}{v_F} \sigma_0 - \Delta k_{\mathrm{soc}} s \sigma_1 \right), \tag{3.74}$$

$$\overline{\overline{H}}_{\pi,\mathrm{cv}}^{\mathrm{eff}} = -v_F \left(\Delta k_{c,\mathrm{cv}}^{(\tau)} \sigma_1 + \Delta k_{\mathrm{cv}}^{(\tau)} \sigma_2 \right). \tag{3.75}$$

Here $s = \pm 1$ represents spin up or spin down, and the elements are given as

$$v_F \Delta k_{\text{soc}} = \alpha_1 \frac{V_{\text{so}}}{2R}, \tag{3.76}$$

$$\epsilon_{\text{soc}}^{(\tau)} = \tau \alpha_2 \frac{V_{\text{so}}}{2R} \cos 3\eta, \tag{3.77}$$

$$v_F \Delta k_{c,\text{cv}}^{(\tau)} = \tau \beta \frac{\cos 3\eta}{(2R)^2}, \tag{3.78}$$

$$\Delta k_{\text{cv}}^{(\tau)} = \tau \zeta \frac{\sin 3\eta}{(2R)^2}. \tag{3.79}$$

For metallic nanotubes the parameters $\alpha_1, \alpha_2, \beta, \zeta$ were fitted to the numerical calculation of the full band structure, giving

$$\alpha_1 = 0.048\,\text{nm}, \tag{3.80}$$

$$\alpha_2 = -0.045\,\text{nm}, \tag{3.81}$$

$$\beta = 24\,\text{meV} \cdot \text{nm}^2, \tag{3.82}$$

$$\zeta = -0.18\,\text{nm}. \tag{3.83}$$

It is easy to show that the generic Hamiltonian

$$\overline{\overline{H}} = E_0 \sigma_0 + v_F c \sigma_1 + v_F k \sigma_2 \tag{3.84}$$

has the eigenvalues

$$\epsilon_{\pm}(k) = E_0 \pm v_F \sqrt{c^2 + k^2}. \tag{3.85}$$

It is thus linear for large k, and gapped at $k = 0$ with an energy splitting of $2v_F c$ between the valence and conduction band. Furthermore it is shifted upwards by E_0. The band structure of $\overline{\overline{H}}_{\pi}^{\text{eff}}$ can be seen in. The leading behaviour of the effective Hamiltonian comes from Eq. (3.72), where it is seen that the band structure is linear in k with a slope v_F. Eq. (3.79) also has a constant σ_2, which shifts the Dirac point along the k direction, with opposite signs for $\boldsymbol{K}$ and $\boldsymbol{K}'$. It thus does not change the local band structure relative to $\boldsymbol{K}$ and $\boldsymbol{K}'$. The second largest term is $-v_F \Delta k_{c,\text{cv}}^{(\tau)} \sigma_1$ in Eq. (3.75), which gives rise to a gap, similar to $v_F c$ in Eq. (3.84). There is a small addition to this gap coming from the $-v_F \Delta k_{\text{soc}} s \sigma_1$ in Eq. (3.74). For $\tau = 1$ and $s = 1$ the two terms have the same sign, while for $s = -1$, they have opposite signs. Spin up electrons thus have a larger band gap than spin down. It should be kept in mind that the difference between the spin up and spin down band gap is small, since $V_{\text{so}} \ll a_{\text{C-C}}/R$. Finally, there is the term $\epsilon_{\text{soc}}^{(\tau)} s \sigma_0$ in Eq. (3.74). It is negative for $s = 1$ since α_2 is negative, so it shifts the spin up band down and the spin down band up. This gives effectively a smaller energy difference between spin up and spin down electrons than between spin up and spin down holes. For $\tau = -1$, the spin down electrons have a larger gap than spin up, but the sign of σ_0 is also flipped, so that electrons still have a smaller energy difference between spin up and spin down than holes.

These results are not in complete agreement with experimental results. In 2008 Kuemmeth et al. [2] found experimentally that there is indeed a difference between the band splitting of electrons and holes. However they found a splitting of 0.37 meV for electrons and 0.21 meV for holes, in disagreement with Izumida's larger splitting for holes than for electrons.

Chapter 4

Toy model

In Chapter 3 it was shown that the band structure near the Fermi level of a neutral metallic carbon nanotube could be described by the Hamiltonian Eq. (3.73). It contained four gapped cones, spin up and spin down combined with $\boldsymbol{K}$ and $\boldsymbol{K'}$. Spin up at $\boldsymbol{K}$ is degenerate with spin down at $\boldsymbol{K'}$, and it has a larger band gap than spin down at $\boldsymbol{K}$, which is degenerate with spin up at $\boldsymbol{K'}$. The $\boldsymbol{K}, \boldsymbol{K'}$ symmetry is due to time reversal symmetry. Furthermore the entire spin up band structure is shifted downwards, while spin down is shifted upwards at $\boldsymbol{K}$, so there is a smaller energy difference between spin up and spin down electrons than between spin up and spin down holes. These are the essential features of the effective Hamiltonian. To investigate how electron-electron interactions modify this band structure, we will use a toy model Hamiltonian, which has all these features, and can be written We will write it

$$\overline{\overline{H}}_0 = v_F(c_s\sigma_1 + k\sigma_2) - v_F ds. \tag{4.1}$$

Here $v_F k$ gives the asymptotic linear band structure, c_s induces a gap which depends on whether s is positive or negative, and ds gives the spin-dependent energy shift. To get the same features as Eqs. (3.73)–(3.83) at $\boldsymbol{K}$, we choose $d > 0$ and $c_+ > c_- > 0$. Coulomb interactions are not expected to break the $\boldsymbol{K}$, $\boldsymbol{K'}$ degeneracy, so the model only includes two cones. Diagonalising $\overline{\overline{H}}_0$ gives the eigenvalues

$$E_{k,s,\zeta} = \zeta v_F\sqrt{k^2 + c_s^2} - v_F ds, \tag{4.2}$$

where $\zeta = \pm 1$, so $\zeta = 1$ means a state in the conduction band, and $\zeta = -1$ is a state in the valence band. In our model we assume zero temperature and a chemical potential in the middle of the gap. Therefore all states in the conduction band are empty, while all states in the valence band are filled. The eigenstates of $\overline{\overline{H}}_0$ can be written

$$\psi_{k,s,\zeta} = \frac{1}{\sqrt{L}}\chi_{k,s,\zeta}e^{ikx} = \frac{1}{\sqrt{L}}\begin{pmatrix} u_{k,s,\zeta} \\ v_{k,s,\zeta} \end{pmatrix} e^{ikx}. \tag{4.3}$$

In principle there should also be a spin space spinor. This is suppressed, while we remember that states with different spins are orthogonal. Therefore states in one cone are orthogonal

to states in the other cone. This is exactly true for spin up and spin down, while there is a finite scattering amplitude from $\boldsymbol{K}$ to $\boldsymbol{K'}$. However, it as been shown that effect of this scattering is smaller than the spin-orbit splitting [35], so we will neglect it. Let us determine $u_{k,s,\zeta}$ and $v_{k,s,\zeta}$.

$$\begin{aligned}
\overline{\overline{H}}_0\psi_{k,s,\zeta} &= E_{k,s,\zeta}\psi_{k,s,\zeta} \\
&= \frac{1}{\sqrt{L}}v_F \begin{pmatrix} -ds & c_s - ik \\ c_s + ik & -ds \end{pmatrix} \begin{pmatrix} u_{k,s,\zeta} \\ v_{k,s,\zeta} \end{pmatrix} e^{ikx} \\
&= \frac{1}{\sqrt{L}}v_F \left(\zeta\sqrt{c_s^2+k^2} - ds\right) \begin{pmatrix} u_{k,s,\zeta} \\ v_{k,s,\zeta} \end{pmatrix} e^{ikx} \qquad (4.4) \\
\Rightarrow (c_s + ik)u_{k,s,\zeta} - dsv_{k,s,\zeta} &= \left(\zeta\sqrt{c_s^2+k^2} - ds\right) v_{k,s,\zeta} \qquad (4.5) \\
\Rightarrow v_{k,s,\zeta} &= \zeta\frac{c_s + ik}{\sqrt{c_s^2+k^2}}u_{k,s,\zeta}, \qquad (4.6)
\end{aligned}$$

so we may choose

$$\chi_{k,s,\zeta} = \begin{pmatrix} u_{k,s,\zeta} \\ v_{k,s,\zeta} \end{pmatrix} = \frac{1}{\sqrt{2}} \begin{pmatrix} 1 \\ \zeta\frac{c_s+ik}{\sqrt{c_s^2+k^2}} \end{pmatrix}. \qquad (4.7)$$

It is seen that

$$\left|\frac{c_s + ik}{\sqrt{c_s^2+k^2}}\right|^2 = 1. \qquad (4.8)$$

Therefore

$$\chi^\dagger_{k,s,\zeta}\chi_{k,s,-\zeta} = 0 \qquad (4.9)$$

for all k, so two states with the same momentum in opposite bands are orthogonal.

In the language of second quantization, the Hamiltonian Eq. (4.1) can be written

$$\begin{aligned}
H_0 &= \sum_{\nu_i,\nu_j} T_{\nu_i,\nu_j} c^\dagger_{\nu_i} c_{\nu_j} \\
&= \sum_{k,s} c^\dagger_{k,s} v_F (d\sigma_0 + c_s\sigma_1 + k\sigma_2) c_{k,s}, \qquad (4.10)
\end{aligned}$$

where $c^\dagger_{k,s}$ and $c_{k,s}$ are two dimensional creation and annihilation operators in AB space. This can be diagonalized in the AB space giving two bands, so

$$\begin{aligned}
H_0 &= \sum_{\nu_i,\nu_j} T_{\nu_i,\nu_j} c^\dagger_{\nu_i} c_{\nu_j} \\
&= \sum_{k,s} c^\dagger_{k,s} v_F \left(d\sigma_0 + \sqrt{k^2+c_s^2}\sigma_3\right) c_{k,s} \\
&= \sum_{k,s,\zeta} c^\dagger_{k,s,\zeta} v_F \left(d + \zeta\sqrt{k^2+c_s^2}\right) c_{k,s,\zeta}. \qquad (4.11)
\end{aligned}$$

In the following calculations d will be neglected, since all excitations will happen inside the same cone, making the d dependence trivial. However, when discussing the physical predictions for spin-orbit splitting in the end, it will be taken into account. neglecting d means that the eigenenergies reduce to

$$E_{k,s,\zeta} = \zeta \xi_{k,s}. \tag{4.12}$$

where we have defined

$$\xi_{k,s} \equiv E_{k,s,+}. \tag{4.13}$$

4.1 Coulomb interactions

To include Coulomb interactions, the Hamiltonian is written

$$H = H_0 + H_{\text{int}}, \tag{4.14}$$

where H_{int} is the Hamiltonian of Coulomb interactions. It is given by [24, sec. 1.4.4]

$$H_{\text{int}} = \int dx \int dx' : \rho(x) V(x - x') \rho(x') : \tag{4.15}$$

where $V(x-x')$ is the strength of the Coulomb interaction, ρ is the electron density operator, and : indicates normal ordering. Normal ordering means that all creation operators are to the left of all annihilation operators. This Hamiltonian couples each electronic state to all the others, and solving it in general is not possible. It is therefore necessary to reduce it to an effective model where inessential terms are neglected. For semiconducting tubes, the effect of short range Coulomb interactions, i.e. interactions with reciprocal wave vectors larger than $1/R$, has already been investigated [3]. It was shown that these short range interactions lead to an increased Fermi velocity and reduced Coulomb interaction strength, but otherwise leave the theory invariant. The short range interactions thus screen the electrons from each other on larger length scales, and the interaction between these screened quasiparticles has the same form as the original interaction between the bare electrons. We may therefore ignore all interactions on reciprocal space length scales larger than $1/R$. From Eq. (3.7) it is seen that the distance between neighboring one-dimensional subbands is just $1/R$. All states in other subbands are thus too far away in reciprocal space to be included, so the one-dimensional toy-model Eq. (4.1), contains all relevant states. Furthermore only states up to the cut-off $q_{\text{c}} \equiv 1/R$ should be included. We would like to write H_{int} in the k, s, ζ basis to exploit translational invariance. ρ can be expressed as

$$\rho = \sum_s \rho_s, \tag{4.16}$$

where

$$\begin{aligned}\rho_s(x) &= \sum_{k,k',\zeta,\zeta'} \psi^\dagger_{k',s,\zeta'}(x) c^\dagger_{k',s,\zeta'} \psi_{k,s,\zeta}(x) c_{k,s,\zeta} \\ &= \frac{1}{L} \sum_{k,k',\zeta,\zeta'} \left(u^*_{k',s,\zeta'} u_{k,s,\zeta} + v^*_{k',s,\zeta'} v_{k,s,\zeta} \right) e^{i(k-k')x} c^\dagger_{k',s,\zeta'} c_{k,s,\zeta}. \end{aligned} \tag{4.17}$$

Let us define

$$\begin{aligned} w_{k',k,s,\zeta'\zeta} &= \langle k', s, \zeta' | k, s, \zeta \rangle \\ &= u^*_{k',s,\zeta'} u_{k,s,\zeta} + v^*_{k',s,\zeta'} v_{k,s,\zeta} \\ &= \frac{1}{2} \left(1 + \zeta\zeta' \frac{c_s - ik'}{\sqrt{k^2 + c_s^2}} \frac{c_s + ik}{\sqrt{k^2 + c_s^2}} \right) \\ &= \frac{1}{2} \left(1 + \zeta\zeta' \frac{k'k + c_s^2 + ic_s(k' - k)}{\sqrt{k'^2 k^2 + c_s^4 + c_s^2(k^2 + k'^2)}} \right), \end{aligned} \tag{4.18}$$

so

$$\begin{aligned} \rho(x) &= \frac{1}{L} \sum_{k,k',s,\zeta,\zeta'} w_{k',k,s,\zeta'\zeta} e^{i(k-k')x} c^\dagger_{k',s,\zeta'} c_{k,s,\zeta} \\ &= \frac{1}{L} \sum_{\nu\nu'} w_{\nu\nu'} e^{i(k-k')x} c^\dagger_{\nu'} c_\nu, \end{aligned} \tag{4.19}$$

where the index $\nu = \{k, s, \zeta\}$ has been defined. $V(x - x')$ is the potential energy due to Coulomb interactions of an electron at position x when there is another electron at position x'. In our toy model, it is assumed that electrons in the lowest subband do not interact with electrons in the higher subband. In the particle-in-a-box picture, the wave function of the electron in the lowest subband is constant in the circumferential direction. All interactions on a reciprocal space scale of more than $1/R$, i.e. interactions on a real space scale less than R, are neglected so we do not include interactions between electron states at the same $\boldsymbol{t}$ coordinate and different θ. Therefore our one-dimensional theory considers interacting rings of charge. $V(x - x')$ is thus the potential energy of a ring of charge at position x in the electrostatic potential of a ring at x'.

We will do the calculation of $V(x - x')$ in cylindrical coordinates, where the two rings are at position

$$\boldsymbol{r}'(\theta') = (R, \theta', 0), \tag{4.20}$$

$$\boldsymbol{r}(\theta) = (R, \theta, z_0 = x - x') \tag{4.21}$$

respectively. This gives the charge distributions on the two rings

$$\rho_{3\mathrm{D},1}(\boldsymbol{r}') = \rho_0 \delta(r' - R)\delta(z'), \tag{4.22}$$

$$\rho_{3\mathrm{D},2}(\boldsymbol{r}) = \rho_0 \delta(r - R)\delta(z - z_0), \tag{4.23}$$

where ρ_0 is the charge density on the ring. Since the ring is a model of a single electron, the total charge of the ring must be equal to the elementary charge, so

$$\rho_0 = \frac{e}{2\pi R}. \tag{4.24}$$

From electrostatics [36, p. 93],

$$\begin{aligned} V(x-x') &= \int \rho_{3\mathrm{D},2}(\boldsymbol{r}) V_{3\mathrm{D}}(\boldsymbol{r}) d\boldsymbol{r} \\ &= \int \rho_0 \delta(r-R)\delta(z-z_0) V_{3\mathrm{D}}(\boldsymbol{r}) r dr d\theta dz \\ &= \int \rho_0 R V_{3\mathrm{D}}(R,\theta,z_0) d\theta. \end{aligned} \tag{4.25}$$

where

$$V_{3\mathrm{D}}(\boldsymbol{r}) = \frac{1}{4\pi\epsilon_0} \int \frac{\rho_{3\mathrm{D},1}(\boldsymbol{r}')}{|\boldsymbol{r}-\boldsymbol{r}'|} r' dr' d\theta' dz' \tag{4.26}$$

is the electrostatic potential from the first ring. From Eqs. (4.20) and (4.21) follows

$$|\boldsymbol{r}-\boldsymbol{r}'| = \sqrt{z_0^2 + 2R^2(1-\cos(\theta-\theta'))}. \tag{4.27}$$

This gives

$$\begin{aligned} V_{3\mathrm{D}}(\boldsymbol{r}) &= \frac{1}{4\pi\epsilon_0} \int \frac{\rho_0 \delta(r'-R)\delta(z')}{\sqrt{z_0^2 + 2R^2(1-\cos(\theta-\theta'))}} r' dr' d\theta' dz' \\ &= \frac{1}{4\pi\epsilon_0} \frac{\rho_0 R}{\sqrt{z_0^2+2R^2}} \int_0^{2\pi} \frac{1}{\sqrt{1-\frac{2R^2}{z_0^2+2R^2}\cos\theta')}} d\theta', \end{aligned} \tag{4.28}$$

where the δ functions have been integrated out and the integration variable has been changed from θ' to $\theta'-\theta$. The integral gives

$$\int_0^{2\pi} \frac{1}{\sqrt{1-a\cos\theta}} d\theta = 2\left(\frac{K(\frac{2a}{1-a})}{\sqrt{1-a}} + \frac{K(\frac{2a}{1+a})}{\sqrt{1+a}} \right), \tag{4.29}$$

where K is the complete elliptic integral of the first kind [37, formula 17.3.1]. This is rather complicated to evaluate, but we observe that for $a \ll 1$,

$$\int_0^{2\pi} \frac{1}{\sqrt{1-a\cos\theta}} d\theta \approx 2\pi, \tag{4.30}$$

so for $z_0 \gg R$,

$$V_{3\mathrm{D}}(\boldsymbol{r}) \approx \frac{1}{4\pi\epsilon_0} \frac{\rho_0 2\pi R}{\sqrt{z_0^2+2R^2}}. \tag{4.31}$$

Therefore, from Eq. (4.25),

$$V(x-x') = \frac{(\rho_0 2\pi R)^2}{4\pi\epsilon_0}\frac{1}{\sqrt{z_0^2+2R^2}} = \frac{e^2}{4\pi\epsilon_0}\frac{1}{\sqrt{(x-x')^2+2R^2}}. \tag{4.32}$$

It can be written in reciprocal space as

$$V(x-x') = \frac{1}{L}\sum_q V(q)e^{iq(x-x')}, \tag{4.33}$$

where $V(q)$ is the Fourier transform of $V(x-x')$, i.e.

$$\begin{aligned} V(q) &= \int dx V(x)e^{-iqx} \\ &= \int dx \frac{e^2}{4\pi\epsilon_0}\frac{1}{\sqrt{x^2+2R^2}}e^{-iqx} \\ &= \frac{e^2}{4\pi\epsilon_0}2K_0(\sqrt{2}Rq), \end{aligned} \tag{4.34}$$

where $K_0(t)$ is the modified Bessel function of the second kind [37, sec. 9.6-9.8]. It diverges logarithmically as t goes to zero, but is of order of magnitude 1 in most of the range $[0,1]$. Since all interactions above $1/R$ have already been taken into account, we will approximate it by

$$\begin{aligned} V(q) &= V_0 \quad \text{for} \quad |q| < q_\mathrm{c} \\ V(q) &= 0 \quad \text{for} \quad |q| > q_\mathrm{c}, \end{aligned} \tag{4.35}$$

where

$$V_0 = 5.3\frac{e^2}{4\pi\epsilon_0}, \tag{4.36}$$

$$q_\mathrm{c} = \frac{1}{R}. \tag{4.37}$$

The approximation for V_0 is based on the numerical calculations in Section 5.5.

We may now integrate out the explicit position dependence in Eq. (4.15).

$$
\begin{aligned}
H_{\text{int}} &= \frac{1}{L^3}\int dx \int dx' : \sum_{\substack{\nu_1,\nu_2\\ \nu_3,\nu_4,q}} w_{\nu_1,\nu_2} e^{i(k_2-k_1)x} c^\dagger_{\nu_1} c_{\nu_2} V(q) e^{i(x-x')q} w_{\nu_3,\nu_4} e^{i(k_4-k_3)x'} c^\dagger_{\nu_3} c_{\nu_4} : \\
&= \frac{1}{L^3}\sum_{\substack{\nu_1,\nu_2\\ \nu_3,\nu_4,q}} V(q) w_{\nu_3,\nu_4} w_{\nu_1,\nu_2} c^\dagger_{\nu_1} c^\dagger_{\nu_3} c_{\nu_4} c_{\nu_2} \int dx \int dx' e^{i(k_4-k_3)x'} e^{i(k_2-k_1)x} e^{i(x-x')q} \\
&= \frac{1}{L^3}\sum_{\substack{\nu_1,\nu_2\\ \nu_3,\nu_4,q}} V(q) w_{\nu_3,\nu_4} w_{\nu_1,\nu_2} c^\dagger_{\nu_1} c^\dagger_{\nu_3} c_{\nu_4} c_{\nu_2} \int dx \int dx' e^{i(k_4-k_3-q)x'} e^{i(k_2-k_1+q)x} \\
&= \frac{1}{L}\sum_{\substack{\nu_1,\nu_2\\ \nu_3,\nu_4,q}} V(q) w_{\nu_3,\nu_4} w_{\nu_1,\nu_2} c^\dagger_{\nu_1} c^\dagger_{\nu_3} c_{\nu_4} c_{\nu_2} \delta_{k_3,k_4-q}\delta_{k_1,k_2+q} \\
&= \frac{1}{L}\sum_{\substack{k,k',q,s,s'\\ \zeta_1,\zeta_2,\zeta_3,\zeta_4}} V(q) w_{k+q,k,s,\zeta_1\zeta_2} w_{k'-q,k',s',\zeta_3\zeta_4} c^\dagger_{k+q,s,\zeta_1} c^\dagger_{k'-q,s',\zeta_3} c_{k',s',\zeta_4} c_{k,s,\zeta_2}. \qquad (4.38)
\end{aligned}
$$

Here we have used the transformation rule

$$
\begin{aligned}
\frac{1}{L}\sum_{k_1,k_2} f(k_1,k_2)\int dx e^{i(k_1-k_2)x} &= \sum_{k_1,k_2} f(k_1,k_2) 2\pi\delta(k_1-k_2) \\
&= \sum_{k_1}\int \frac{dk_2}{2\pi} f(k_1,k_2) 2\pi\delta(k_1-k_2) \\
&= \sum_{k_1} f(k_1,k_1). \qquad (4.39)
\end{aligned}
$$

In the original AB basis where H_0 is not orthogonal, H_{int} is

$$
H_{\text{int}} = \frac{1}{L}\sum_{\substack{k,k',q\\ s,s',X,X'}} V(q) c^\dagger_{k+q,s,X} c^\dagger_{k'-q,s',X'} c_{k',s',X'} c_{k,s,X}, \qquad (4.40)
$$

where X and X' represent $A(B)$ index.

Let us finish the discussion of the toy model by estimating the size of the parameters. It has been shown [3] that the bare non-interacting graphene Fermi velocity is renormalized in carbon nanotubes by short range ($< R$) Coulomb interactions to the value

$$
v_F = 1.1\cdot 10^6 \frac{\text{m}}{\text{s}}. \qquad (4.41)
$$

Since we have set $\hbar = 1$ in all equations, it is necessary to reinsert it when we want to plug in numbers. When $\hbar = 1$, energy has units of inverse time, so we can make the conversion

$$
\begin{aligned}
\hbar v_F &= 6.6\cdot 10^{-13}\text{meV}\cdot\text{s}\cdot 1.1\cdot 10^6 \frac{\text{m}}{\text{s}} \\
&\to 7.2\cdot 10^2 \text{meV}\cdot\text{nm} \qquad (4.42) \\
&\Rightarrow \text{nm}^{-1} \leftrightarrow 7.2\cdot 10^2 v_F^{-1}\text{meV}. \qquad (4.43)
\end{aligned}
$$

We would like to estimate the size of all parameters entering the theory. The Coulomb interaction is given by Eq. (4.36),

$$\begin{aligned} V_0 &= 5.3\frac{e^2}{4\pi\epsilon_0} \\ &= 5.3\frac{e^2}{4\pi\frac{e^2}{2\alpha 2\pi\hbar c}} \\ &= 5.3\alpha\hbar c, \end{aligned} \tag{4.44}$$

where $c = 3 \cdot 10^8 \text{m/s} = 272 v_F$ is the speed of light, and $\alpha = 1/137$ is the fine structure constant. This gives

$$V_0 = 5.3 \cdot 2v_F, \tag{4.45}$$

$$g_{\text{bare}} \equiv \frac{V_0}{2\pi v_F} = 1.69, \tag{4.46}$$

where we have defined the bare coupling constant g_{bare}. The bare interaction is however screened by short range interactions to [3]

$$g \equiv \frac{g_{\text{bare}}}{1 + g_{\text{bare}}\pi/2} = 0.46. \tag{4.47}$$

In experiments, the nanotube is occasionally placed on a substrate which induces long range dielectric screening. This changes V_0, since the permittivity is changed from ϵ_0 to $\epsilon = \epsilon_0\epsilon_r$. Therefore g should be divided by ϵ_r in the case of screening. ϵ_r lies typically in the range $1 - 10$. The other parameters are

$$R \approx 1\text{nm} \tag{4.48}$$

$$\Rightarrow q_{\text{c}} = \frac{1}{R} \approx 1\text{nm}^{-1} \approx 1000 v_F^{-1}\text{meV}. \tag{4.49}$$

c_s is approximately given by Eq. (3.78), so

$$c_s \approx \frac{\beta}{(2R)^2 v_F} \approx 10^{-2}\text{nm}^{-1} \approx 10 v_F^{-1}\text{meV}. \tag{4.50}$$

The difference between c_s and c_{-s} is given by Eq. (3.76), so

$$c_s - c_{-s} \approx 10^{-4}\text{nm}^{-1} \approx 0.1 v_F^{-1}\text{meV}. \tag{4.51}$$

The spin-dependent shift d is, from Eq. (3.77),

$$d \approx 10^{-4}\text{nm}^{-1} \approx 0.1 v_F^{-1}\text{meV}. \tag{4.52}$$

The momenta are quantized in steps of the inverse system size $\frac{1}{L}$, so

$$\frac{1}{L} \approx 10^{-3}\text{nm}^{-1} \approx v_F^{-1}\text{meV}. \tag{4.53}$$

It is thus seen that the states can still be viewed as continuous in the gapped area, but the second lowest state in the small gap cone has much higher energy than the lowest state in the large gap cone. In experiments it is thus possible to choose an energy range where only the lowest state in each cone is probed.

Chapter 5

First order perturbation theory

In Chapters 2 and 3 the eigenstates of a non-interacting Hamiltonian were found using single particle quantum mechanics. We will now turn our attention to the interacting Hamiltonian. To find its eigenvalues, i.e. the energies of the system, many-body quantum theory will be used. We will start by explaining the central concepts, following the derivations in Bruus and Flensberg [24]. Then we will show how the eigenenergies of the non-interacting Hamiltonian are modified to first order in the Coulomb interaction.

The full Hamiltonian consists of a non-interacting and an interacting term, H_0 and H_{int}. The non-interacting Hamiltonian, Eq. (4.10), is given by

$$H_0 = \sum_{\nu_i} E_{\nu_i} c^\dagger_{\nu_i} c_{\nu_i}. \tag{5.1}$$

If a single-particle state $|\nu_j\rangle$ is occupied, then

$$\langle \nu_j | H_0 | \nu_j \rangle = E_{\nu_j}, \tag{5.2}$$

and if a set of single particle states $|\mu\rangle = \{|\nu_j\rangle\}$ is occupied,

$$\langle \mu | H_0 | \mu \rangle = \sum_{\nu_j} E_{\nu_j}. \tag{5.3}$$

For a many-body system described by H_0, the energy is just the sum of the energies of all the particles independent of each other. Therefore H_0 is called non-interacting. This is not the case for H_{int}, found in Eq. (4.38) as

$$H_{int} = \frac{1}{L} \sum_{\substack{k,k',q,s,s' \\ \zeta_1,\zeta_2,\zeta_3,\zeta_4}} V(q) w_{k+q,k,s,\zeta_1\zeta_2} w_{k'-q,k',s',\zeta_3\zeta_4} c^\dagger_{k+q,s,\zeta_1} c^\dagger_{k'-q,s',\zeta_3} c_{k',s',\zeta_4} c_{k,s,\zeta_2}. \tag{5.4}$$

It contains two pairs of creation and annihilation operators, so the state of all the other electrons heavily influences the energy of a single particle. This makes diagonalizing H a true many-body problem, where every particle interacts with all the others. The eigenstates of H will not be a sum of single-particle states as for H_0, but collective excitations,

called quasiparticles. However, if H_{int} is much weaker than H_0, the quasiparticles will be similar to the single-particle states, and their energy can be found through perturbation theory. Approximating the energy of a quasiparticle through perturbation theory is however not as simple for interacting many-body systems as for single-particle Hamiltonians. For this we will need the theory of Green's functions and Feynman diagrams, which will be introduced in the next section. For further reading, see [24].

5.1 Green's functions

A Green's function contains information about how a many-body state propagates from one state at one time to another state at another time. We will focus on the single-particle Green's functions, because they convey information about the energies of the quasiparticles. It is emphasized that by single-particle Green's function we mean the propagator of a single particle under the influence of the interactions with the other electrons. Let us define the greater Green's function as [24, p. 125]

$$\begin{aligned} G^{>}(\nu,\nu',t) &= -i\langle c_\nu(t)c^\dagger_{\nu'}(0)\rangle \\ &= -i\langle e^{iHt}c_\nu e^{-iHt}c^\dagger_{\nu'}\rangle. \end{aligned} \tag{5.5}$$

Here the average is defined as [24, p. 27]

$$\langle A\rangle = \frac{\mathrm{Tr}[\rho A]}{\mathrm{Tr}[\rho]}, \tag{5.6}$$

where $\rho = \exp(-\beta H)$. For a system at zero temperature, the operators in the bracket work on the ground state of the Hamiltonian. The chemical potential is included in the Hamiltonian. Eq. (5.5) should be read as following. First an electron is created in the state ν', then the state is allowed to propagate for a time t before an electron is annihilated in the state ν. The state is then propagated back again by a time t, and the inner product is taken with the ground state. For free electrons with the Hamiltonian Eq. (5.3), this gives [24, p. 127]

$$G_0^{>}(\nu,\nu',t) = -i(1-n_F(E_\nu))e^{-iE_\nu t}\delta_{\nu,\nu'}. \tag{5.7}$$

It is seen that the Green's function oscillates with a frequency identical to the energy of the single-particle state ν, if the state is not completely occupied. Since ν is an eigenstate of H, the electron stays in its initial state throughout the propagation, hence the Kronecker δ. We may also define the lesser Green's function as

$$G^{<}(\nu,\nu',t) = -i\langle c^\dagger_{\nu'}(0)c_\nu(t)\rangle, \tag{5.8}$$

which for the free Hamiltonian in Eq. (5.1) gives

$$G_0^{<}(\nu,\nu,t) = -in_F(E_\nu)e^{-iE_\nu t}. \tag{5.9}$$

It thus oscillates with the energy of the state ν if ν is not completely empty. At zero temperature, the one-particle states are completely filled if they are below the Fermi energy and completely empty if they are above the Fermi energy. For non-interacting electrons, the energies E_ν in the Green's functions Eqs. (5.7) and (5.9) are equal to the energy of adding an electron to the system in the state ν. It is convenient to introduce the retarded Green's function

$$G^R(\nu,\nu',t) = \theta(t)(G^>(\nu,\nu',t) - G^<(\nu,\nu',t)), \tag{5.10}$$

where $\theta(t)$ is the Heaviside step function. In the free case it gives

$$G_0^R(\nu,\nu,t) = -i\theta(t)e^{-iE_\nu t}. \tag{5.11}$$

It measures the energy of the single-particle state $|\nu\rangle$ disregarding whether it is empty or not. For the non-interacting case, E_ν can be read off directly from Eq. (5.11). However, to extract the energy from Eq. (5.10) in the general case, we have to introduce a few more mathematical concepts. The Fourier transform of the non-interacting retarded Green's function is

$$\begin{aligned} G_0^R(\nu,\nu,\omega) &= \int dt\, G_0^R(\nu,\nu,t)e^{i(\omega+i\eta)t} \\ &= -i\int dt\theta(t)e^{-iE_\nu t}e^{i\omega t}e^{-\eta t} \\ &= \frac{1}{\omega - E_\nu + i\eta}. \end{aligned} \tag{5.12}$$

The Fourier transform is here defined slightly differently than conventionally, by using the complex frequency $\omega + i\eta$ instead of ω. η is here a positive infinitesimal, introduced to ensure that the Fourier transform converges. It is just a generalization of the Fourier transform to accomodate for principle value integrals. From here we may define the spectral function

$$A(\nu,\omega) = -2\mathrm{Im}G^R(\nu,\nu,\omega), \tag{5.13}$$

so

$$A_0(\nu,\omega) = -2\mathrm{Im}G_0^R(\nu,\nu,\omega) \tag{5.14}$$

$$= 2\pi\delta(\omega - E_\nu). \tag{5.15}$$

It is zero for all ω except for $\omega - E_\nu$, where it has a peak. The spectral function can be viewed as a function indicating how the energy depends on the quantum number. For a non-interacting particle it is a δ function in the diagonal basis, so the energy is uniquely defined when the quantum number is known. For interacting particles, this is not the case if ν expresses single-particle states. Depending on the strength of H_{int}, the spectral function will be modified and more or less broadened. However, if $A_0(\nu,\omega)$ has a sharp peak, the spectral function is close to a δ function, meaning that the state is close to

behaving like a non-interacting quasiparticle. The width of the peak is proportional to the inverse lifetime of the quasiparticle with energy given by the position of the peak. For a non-interacting particle, Eq. (5.15), the width is zero, meaning that the state has an infinite lifetime. This is already known, since an eigenstate of the Hamiltonian is invariant under time evolution. If interactions are weak, we know that the quasiparticle approximation is good, so the spectral function is sharply peaked. The peak is however shifted from its non-interacting position to the energy of the quasiparticle. Finding the energy of the quasiparticle thus amounts to finding the peak of the spectral function. This will be done using the formalism of Matsubara Green's functions.

5.1.1 Matsubara Green's function

We may view the retarded Green's function Eq. (5.10) as a function of t for some specific ν, ν'. Instead of only being defined for real time values t, we may expand it analytically to be defined in the entire complex plane, such that $t \to t - i\tau$. It turns out that it is much easier to evaluate the retarded Green's function on the imaginary axis, i.e. as a function of τ instead of as a function of t. We call the retarded Green's function on the imaginary axis a Matsubara Green's function, $\mathcal{G}(\nu, \nu', \tau)$, so

$$G^R(\nu, \nu', t) \xrightarrow{t \to \tau} \mathcal{G}(\nu, \nu', \tau), \tag{5.16}$$

Which can be Fourier transformed, and if we call the frequency corresponding to imaginary time $i\omega_n$,

$$G^R(\nu, \nu', \omega) = \mathcal{G}(\nu, \nu', i\omega_n \to \omega + i\eta). \tag{5.17}$$

When Fourier transforming, the imaginary time is not integrated from $-\infty$ to ∞, but from $-\beta$ to β. This means that imaginary time frequencies are discrete, hence the subscript n. Since we work in the zero temperature limit, we will let $\beta \to \infty$, making $i\omega_n$ continuous. However, we will sum the Matsubara frequencies as if they were discrete, and take the zero temperature limit afterwards. The free Matsubara Green's function is

$$\mathcal{G}_0(\nu, \nu, i\omega_n) = \frac{1}{i\omega_n - E_\nu}, \tag{5.18}$$

where E_ν is the energy of the state ν.

The Green's function $\mathcal{G}(\nu, \nu', \tau)$ propagates a single particle in a many-body system from the state ν' to ν in the imaginary time τ. To find the explicit form of it, we will use the quantum mechanical principle that the Hamiltonian is the generator of translations in time. Since we have analytically continued our time variable into imaginary time, leaving everything else unchanged, the Hamiltonian has become the generator of translations in imaginary time. This propagation will now be explained in the language of Feynman diagrams.

The particle starts out by propagating according to the non-interacting Green's function for an infinitesimal imaginary time step. Then the Hamiltonian works on it, which either lets it continue unchanged through H_0, or lets it interact with another particle

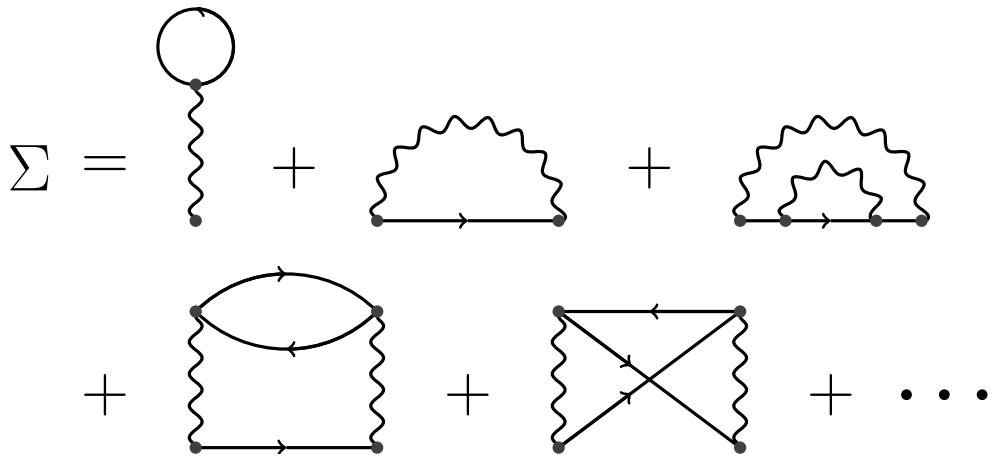

Figure 5.1: The self-energy consists of the sum of all irreducible diagrams with no external legs.

through H_{int}. If it interacts with another particle, momentum is transfered from one particle to the other. Then it continues for another infinitesimal time step, before the Hamiltonian works on it again. After having done this for a lot of infinitesimal steps, an amount τ of imaginary time has passed, and the propagation has finished. All the other electrons are also transformed by the Hamiltonian after each time step, and interact with each other. However, if they do not interact with our particular particle, its propagation is not changed by them. This is why we, in Feynman diagram language, only include connected diagrams. There is the restriction on this propagation that it has to take the particle from ν' to ν. Furthermore it is a single-particle propagator, so after the propagation, all the other particles should be left undisturbed. All momentum transfered to them during the first steps of the propagation should thus be taken back before the propagation has ended. All of these possible propagation paths are summed up, and the result is expressed in $\mathcal{G}(\nu, \nu', \tau)$. If H_{int} is small compared to H_0, then the amplitude of a path decreases exponentially fast with the number of times the particle has interacted with H_{int}. Therefore it is typically only necessary to include the paths with the fewest interactions. This propagation can be modelled using Feynman diagrams, as shown in Fig. 5.1. Each diagram corresponds to one such propagation path. To get the full Green's function, all diagrams should be summed.

We will now describe which Feynman diagrams are allowed, and their interpretation. The straight lines in the diagrams represent non-interacting Green's functions, and the wavy lines represent momentum transfer through the Coulomb interaction. Let us write $\nu = \{k, \mu\}$, where k is the momentum and μ is the additional quantum numbers. When one propagator for a state k', μ' ends at a vertex where a wavy line leads out the momentum q, a new one with state $k\mu$ can only start from that vertex if μ and μ' are not orthogonal and $k' = k + q$, so the diagram is multiplied by an amplitude $\langle \mu | \mu' \rangle \delta_{k', k+q}$. It can be shown that the full Green's function can be expressed using a self-energy $\Sigma(\nu, \nu')$ [24, p. 236] by

Dyson's equation,

$$\begin{aligned}\overline{\overline{\mathcal{G}}} &= \overline{\overline{\mathcal{G}}}_0 + \overline{\overline{\mathcal{G}}}_0\overline{\overline{\Sigma}}\,\overline{\overline{\mathcal{G}}} \\ &= \left(\overline{I} - \overline{\overline{\mathcal{G}}}_0\overline{\overline{\Sigma}}\right)^{-1}\overline{\overline{\mathcal{G}}}_0. \end{aligned} \tag{5.19}$$

where the elements of $\overline{\overline{\mathcal{G}}}$ are $\langle\nu_i|\mathcal{G}|\nu_j\rangle$ and so on. The self-energy is given as the sum of all connected diagrams where the two external lines are removed, as shown in Fig. 5.1. From Eq. (5.7), $\overline{\overline{\mathcal{G}}}_0$ is diagonal and, if $\overline{\overline{\Sigma}}$ is also diagonal, Eq. (5.19) has the solution

$$\begin{aligned}\mathcal{G}(\nu, i\omega_n) &= \frac{\mathcal{G}_0(\nu, i\omega_n)}{1 - \mathcal{G}_0(\nu, i\omega_n)\Sigma(\nu, i\omega_n)} \\ &= \frac{1}{i\omega_n - E_\nu - \Sigma(\nu, i\omega_n)}. \end{aligned} \tag{5.20}$$

When $i\omega_n$ is replaced by $\omega + i\eta$ to get the original retarded Green's function, comparing with Eq. (5.12) shows that the energy of the quasiparticle is the frequency for which $\mathcal{G}(\nu, i\omega_n)$ has a pole. In our case, however, $\overline{\overline{\Sigma}}$ is not necessarily diagonal. The basis in which H_0 is diagonal is $\nu = \{k, s, \zeta\}$. If an incoming electron at a vertex is in the state $\{k, s, \zeta\}$, and a momentum q is removed by an interaction line, it is possible for a particle in the state $\{k - q, s, \zeta'\}$ to leave the vertex with an amplitude

$$\langle k, s, \zeta | k - q, s, \zeta'\rangle = w_{k,k-q,s,\zeta\zeta'}. \tag{5.21}$$

This is non-zero for $\zeta = -\zeta'$ for all $q \neq 0$. Since Coulomb interactions conserve both spin and momentum, and the propagation has to leave the surroundings in the same state as before propagation, Σ must be diagonal both in spin and momentum space. There is no conservation law for ζ, so Σ is a 2×2 matrix in ζ space. Inserting this result in Eq. (5.19) gives

$$\mathcal{G}(k, s, \zeta, i\omega_n) = \frac{1}{\mathcal{G}_0(k, s, \zeta, i\omega_n)^{-1} - \Sigma_{ks}(\zeta, \zeta) - \frac{\Sigma_{ks}(+,-)\Sigma_{ks}(-,+)}{\mathcal{G}_0(k,s,-\zeta,i\omega_n)^{-1} - \Sigma_{ks}(-\zeta,-\zeta)}}. \tag{5.22}$$

The effective self-energy of the quasiparticle is thus

$$\Sigma^{\text{eff}}_{ks}(\zeta, \zeta) = \Sigma_{ks}(\zeta, \zeta) + \frac{\Sigma_{ks}(+,-)\Sigma_{ks}(-,+)}{\mathcal{G}_0(k, s, -\zeta)^{-1} - \Sigma_{ks}(-\zeta, -\zeta)}, \tag{5.23}$$

where the Matsubara frequency index in the self-energies has been suppressed. This will also be done for the propagators, so

$$\mathcal{G}(k, s, \zeta) \equiv \mathcal{G}(k, s, \zeta, i\omega_n). \tag{5.24}$$

For a state in the conduction band ($\zeta = 1$), the quasiparticle corresponds to adding an electron. In this case the energy it costs to add an electron is given by the pole of the full Green's function Eq. (5.20), using the effective self-energy. For a state in the valence band, the quasiparticle excitation is a hole, whose energy is given as minus the frequency

of the pole. Finding the exact self-energy amounts to calculating all connected diagrams, which is an impossible task. However, if the Coulomb interaction is weak, the diagrams of low order will have a larger contribution than higher order diagrams. This is the basis of perturbation theory, and we will therefore start by calculating the diagrams of lowest order. Let us, before going on to the explicit evaluation of the diagrams, state how a Feynman diagram is read:

- Straight lines propagate a fermion in a state $\{ks\zeta, ik_n\}$, and they give a factor $\mathcal{G}_0(ks\zeta, ik_n)$.
- Wavy lines symbolize transfer of momentum q through Coulomb interactions, and give a factor $-V(q)$.
- Each vertex with an incoming electron in the state $\{k, s, \zeta\}$ and outgoing electron in $\{k-q, s, \zeta'\}$ gives a factor $w_{k,k-q,s,\zeta\zeta'}$.
- At each vertex both momentum and Matsubara frequency should be conserved.
- For each fermion loop, meaning a closed loop of straight lines, the diagram should be multiplied by -1.
- To include all allowed paths, all ζ and Matsubara frequencies are summed over, and internal momenta are integrated out. Each momentum integral is normalized by a factor $\frac{1}{2\pi}$, and each Matsubara sum by $\frac{1}{\beta}$.

It will thus be necessary to perform sums over Matsubara frequencies, which can be done using contour integration [24, sec. 11.4].

5.2 Fermi and Bose frequencies at zero temperature, and why we do not care

In the next section we will perform the summation over Matsubara frequencies summation for both Fermi and Bose frequencies. Fermi frequencies arise from the free propagators, and Bose frequencies from the wavy interaction lines $V(q)$. The Bose frequencies are given by [24, chap. 11]

$$q_n = \frac{2n\pi}{\beta}, \tag{5.25}$$

and the Fermi frequencies are

$$k_n = \frac{(2n+1)\pi}{\beta}. \tag{5.26}$$

When they are summed, they give

$$\frac{1}{\beta}\sum_{iq_n} g_0(iq_n) = -\sum_j \operatorname*{Res}_{z=z_j}[g_0(z)]n_B(z_j), \tag{5.27}$$

$$\frac{1}{\beta}\sum_{ik_n} g_0(ik_n) = \sum_j \operatorname*{Res}_{z=z_j}[g_0(z)]n_F(z_j). \tag{5.28}$$

The Bose and Fermi functions are given as

$$n_B(z) = \frac{1}{e^{\beta z} - 1}, \tag{5.29}$$

$$n_F(z) = \frac{1}{e^{\beta z} + 1}. \tag{5.30}$$

It can be seen that

$$n_B(z + iq_n) = n_B(z), \tag{5.31}$$

$$n_F(z + iq_n) = n_F(z), \tag{5.32}$$

$$n_B(z + ik_n) = -n_F(z), \tag{5.33}$$

$$n_F(z + ik_n) = -n_B(z). \tag{5.34}$$

For zero temperature, i.e. $\beta \to \infty$,

$$n_F(z) = -n_B(z). \tag{5.35}$$

Therefore Eqs. (5.27) and (5.28) are exactly the same. In addition, from Eqs. (5.31) and (5.34) it is seen evident that adding a Bose or Fermi frequency to the variable of a Bose or Fermi function does not change the value of the function.

5.3 Hartree diagram

The Hartree diagram as seen in Fig. 5.2 is the simplest diagram. Since the incoming and outgoing non-interacting propagator must have the same momentum, the interaction line transfers zero momentum, so it contributes with a factor $-V(0)$. The propagator in the loop is $\mathcal{G}_0(p, s', \zeta)$. Since the propagator ends at its own beginning in the loop vertex, the overlap is $w_{p,p,s',+} = 1$. The lower vertex gives

$$w_{k,k,s,\zeta\zeta'} = (1 + \zeta\zeta')/2 = \delta_{\zeta\zeta'} \tag{5.36}$$

The fermion loop gives a factor -1. This means that

$$\Sigma^{\text{Hartree}}_{ks}(+,-) = \Sigma^{\text{Hartree}}_{ks}(-,+) = 0, \tag{5.37}$$

$$\begin{aligned}\Sigma^{\text{Hartree}}_{ks}(\zeta,\zeta) &= \frac{1}{\beta}\sum_{ip_n}\frac{1}{2\pi}\int dp \sum_{s',\zeta} V(0)\mathcal{G}_0(p, s', \zeta', ip_n) \\ &= \frac{1}{\beta}\sum_{ip_n}\frac{1}{2\pi}\int dp \sum_{s',\zeta'} V(0)\frac{1}{ip_n - E_{p,s,\zeta'}}.\end{aligned} \tag{5.38}$$

From Eq. (4.1) it is seen that the energies in the lower band are the same as in the upper band with opposite sign, so we write

$$E_{p,s,\zeta} = \zeta\xi_{p,s}. \tag{5.39}$$

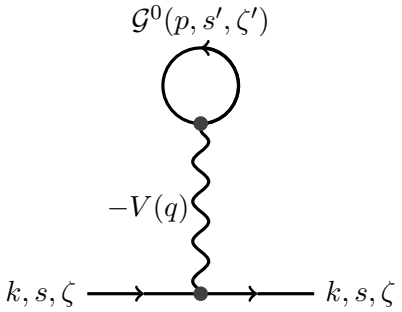

Figure 5.2: The Hartree diagram.

Therefore

$$\Sigma_{ks}^{\text{Hartree}}(\zeta, \zeta) = \frac{1}{2\pi} \int dp \sum_{s',\zeta'} V(0) n_F(\zeta' \xi_{p,s'}). \tag{5.40}$$

At zero temperature the Fermi function is zero for negative ζ and one for positive ζ, so

$$\begin{aligned} \Sigma_{ks}^{\text{Hartree}}(\zeta, \zeta) &= \frac{1}{2\pi} \int dp \sum_{s'} V(0) \\ &= \sum_{p,s'} V(0) \\ &= \frac{N}{L} V(0). \end{aligned} \tag{5.41}$$

It is seen that it is independent of all three indeces k, s, ζ. This means that all states are shifted upwards in energy by the same amount $\frac{N}{L}V(0)$. However, it is impossible to measure such a shift, since energies can only be measured compared to some external reference system, so only energy differences between states of a system can be measured. Since the Hartree term as an overall shift in energy thus has no physical significance, we will neglect it.

5.4 Fock diagram

The Fock or exchange self-energy diagram is shown in figure Fig. 5.3, and is given by

$$\Sigma_{ks}^{\text{Fock}}(\zeta_i, \zeta_o) = \frac{1}{\beta} \int \frac{dq}{2\pi} \sum_{\zeta, iq_n} (-V(q)) \mathcal{G}^0(k + q, s, \zeta) w_{k,k+q,s,\zeta_i\zeta} w_{k+q,k,s,\zeta\zeta_o}. \tag{5.42}$$

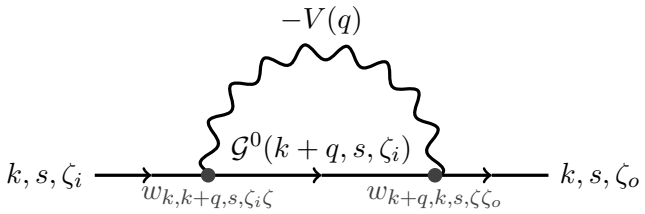

Figure 5.3: The Fock diagram.

The propagator is

$$\mathcal{G}^0(k+q,s,\zeta) = \frac{1}{ik_n + iq_n - \zeta\xi_{k+q,s}} \tag{5.43}$$

$$\Rightarrow \frac{1}{\beta}\sum_{\zeta,iq_n} \mathcal{G}^0(k+q,s,\zeta) = n_F(\zeta\xi_{k+q,s}) = \delta_{\zeta,-1}, \tag{5.44}$$

since all valence band states are filled and all conduction band states are empty. The vertex overlaps are

$$w_{k,k+q,s,\zeta_i\zeta} = \frac{1}{2}\left(1 + \zeta_i\zeta\frac{c_s - ik}{\sqrt{k^2+c_s^2}}\frac{c_s + i(k+q)}{\sqrt{(k+q)^2+c_s^2}}\right) = \frac{1}{2}(1+\zeta_i\zeta a), \tag{5.45}$$

$$w_{k+q,k,s,\zeta\zeta_o} = \frac{1}{2}\left(1 + \zeta_o\zeta\frac{c_s - i(k+q)}{\sqrt{(k+q)^2+c_s^2}}\frac{c_s + ik}{\sqrt{k^2+c_s^2}}\right) = \frac{1}{2}(1+\zeta_o\zeta a^*), \tag{5.46}$$

where

$$a \equiv \frac{c_s - ik}{\sqrt{k^2+c_s^2}}\frac{c_s + i(k+q)}{\sqrt{(k+q)^2+c_s^2}} \tag{5.47}$$

has been introduced for clarity. Using $|a|^2 = 1$ and $\zeta = -1$ from Eq. (5.44)

$$w_{k,k+q,s,-\zeta_i}w_{k+q,k,s,-\zeta_o} = \frac{1}{4}(1+\zeta_i\zeta_o - (\zeta_i a + \zeta_o a^*)). \tag{5.48}$$

It is thus seen that for $\zeta_i = \zeta_o$,

$$\begin{aligned} w_{k,k+q,s,-\zeta_i}w_{k+q,k,s,-\zeta_i} &= |w_{k,k+q,s,-\zeta_i}|^2 \\ &= \frac{1}{2}\left(1 - \zeta_i \mathrm{Re}(a)\right) \\ &= \frac{1}{2}\left(1 - \zeta_i\frac{c_s^2 + (k+q)k}{\sqrt{(k+q)^2+c_s^2}\sqrt{k^2+c_s^2}}\right). \end{aligned} \tag{5.49}$$

Inserting this into Eq. (5.42) and using $V(q)$ as defined in Eq. (4.35), yields

$$\Sigma_{ks}^{\text{Fock}}(\zeta,\zeta) = -\frac{V_0}{2\pi}\int_{-q_c}^{q_c} dq \frac{1}{2}\left(1-\zeta\frac{c_s^2+(k+q)k}{\sqrt{(k+q)^2+c_s^2}\sqrt{k^2+c_s^2}}\right). \tag{5.50}$$

As $\Sigma_{ks}^{\text{Fock}}(\zeta,\zeta)$ is evidently symmetric in k, so we will assume $k \geq 0$ in the following. Using the notation

$$\int_a^b dx f(x) + \int_c^d dx f(x) = \left(\int_a^b dx + \int_c^d dx\right) f(x), \tag{5.51}$$

we obtain

$$\begin{aligned}\Sigma_{ks}^{\text{Fock}}(\zeta,\zeta) =& -gv_F\int_{-q_c+k}^{q_c+k} dq\frac{1}{2}\left(1-\zeta\frac{c_s^2+qk}{\sqrt{q^2+c_s^2}\sqrt{k^2+c_s^2}}\right) &(5.52)\\ =& -gv_F\frac{1}{2}\left(\left(2\int_0^{q_c-k}dq+\int_{q_c-k}^{q_c+k}dq\right)\left(1-\zeta\frac{c_s^2}{\sqrt{q^2+c_s^2}\sqrt{k^2+c_s^2}}\right)\right.\\ &\left.-\zeta\int_{q_c-k}^{q_c+k}dq\frac{qk}{\sqrt{q^2+c_s^2}\sqrt{k^2+c_s^2}}\right). &(5.53)\end{aligned}$$

The integrals are solved using

$$\int dx\frac{1}{\sqrt{x^2+a^2}} = \ln\left(\sqrt{x^2+a^2}+x\right) \tag{5.54}$$

$$\int dx\frac{x}{\sqrt{x^2+a^2}} = \sqrt{x^2+a^2}, \tag{5.55}$$

so

$$\begin{aligned}\Sigma_{ks}^{\text{Fock}}(\zeta,\zeta) =& -gv_F\frac{1}{2}\left(2q_c-\frac{\zeta}{\sqrt{k^2+c_s^2}}\right.\\ &\left.\left(c_s^2\ln\left(\sqrt{c_s^2+q^2}+q\right)\left(2|_0^{q_c-k}+|_{q_c-k}^{q_c+k}\right)+k\sqrt{q^2+c_s^2}|_{q_c-k}^{q_c+k}\right)\right)\\ =& -gv_F\frac{1}{2}\left(2q_c-\frac{\zeta}{\sqrt{k^2+c_s^2}}\right.\\ &\left(c_s^2\ln\left(\frac{(\sqrt{c_s^2+(q_c-k)^2}+q_c-k)(\sqrt{c_s^2+(q_c+k)^2}+q_c+k)}{c_s^2}\right)\right.\\ &\left.\left.+\ k\left(\sqrt{(q_c+k)^2+c_s^2}-\sqrt{(q_c-k)^2+c_s^2}\right)\right)\right). &(5.56)\end{aligned}$$

The constant term $-gv_F q_c$ is independent of k, s, ζ. It therefore just gives a constant shift, so it will be neglected, as the Hartree term before. For $\zeta_i = -\zeta_o$,

$$\begin{aligned} w_{k,k+q,s,\zeta_i} w_{k+q,k,s,-\zeta_i} &= -\frac{1}{2} i\zeta_i \mathrm{Im}(a) \\ &= -\frac{1}{2} i\zeta_i \frac{c_s}{\sqrt{k^2+c_s^2}} \frac{q}{\sqrt{(k^2+q^2)+c_s^2}}. \end{aligned} \tag{5.57}$$

Therefore

$$\begin{aligned} \Sigma_{ks}^{\mathrm{Fock}}(\zeta,-\zeta) &= g\frac{1}{2} i\zeta \frac{c}{\sqrt{c_s^2+k^2}} \int_{-q_c}^{q_c} \frac{q}{\sqrt{(k+q)^2+c_s^2}} \\ &= gv_F \frac{1}{2} i\zeta \frac{c}{\sqrt{c_s^2+k^2}} \int_{-q_c+k}^{q_c+k} \frac{q-k}{\sqrt{q^2+c_s^2}} \\ &= gv_F \frac{1}{2} i\zeta \frac{c}{\sqrt{c_s^2+k^2}} \left(\sqrt{(q_c+k)^2+c_s^2} - \sqrt{(q_c-k)^2+c_s^2} \right. \\ &\left. -k \ln \left(\frac{\left(\sqrt{c_s^2+(q_c-k)^2}+q_c-k\right)\left(\sqrt{c_s^2+(q_c+k)^2}+q_c+k\right)}{c_s^2} \right) \right). \end{aligned} \tag{5.58}$$

It is seen that $\Sigma_{ks}^{\mathrm{Fock}}(\zeta,-\zeta)$ is zero for $k=0$, so the effective self-energy Eq. (5.23) at $k=0$ is

$$\Sigma_{0s}^{\mathrm{eff}}(\zeta,\zeta) = \Sigma_{0,s}(\zeta,\zeta). \tag{5.59}$$

$\Sigma_{0,s}(\zeta,\zeta)$ reduces to

$$\begin{aligned} \Sigma_{0,s}(\zeta,\zeta) &= \zeta g v_F c_s \ln \left(\frac{\sqrt{c_s^2+q_c^2}+q_c}{c_s} \right) \\ &\approx \zeta g v_F c_s \ln \left(\frac{2q_c}{c_s} \right), \end{aligned} \tag{5.60}$$

where the last approximation is valid since $q_c \approx 100 c_s$, as can be seen from comparing Eqs. (4.48) and (4.50). From Eq. (5.60) we see that the self-energy of an electron is positive, and the self-energy of a hole is negative. This means that the gap gets larger. In graphene it was found [28] that the Fock diagram gives rise to a self-energy given by

$$\Sigma_{\mathrm{graphene}} = \zeta g v_F |\boldsymbol{k}| \ln \left(\frac{\Lambda}{|\boldsymbol{k}|} \right), \tag{5.61}$$

where Λ is a momentum cut-off of the order $1/a$, the length of the lattice vector in graphene. Our theory shows that exactly the same happens due to long range interactions in nearly metallic nanotubes. The graphene Fock self-energy has been used to predict the gap renormalization in semiconducting nanotubes [3]. Using the graphene result is

equivalent to including only short range interactions, since a nanotube is only similar to graphene on length scales smaller than $1/R$, where curvature effects are negligible. It is promising that our theory coheres with previous calculations of graphene and semiconducting nanotube gaps. The gap renormalization of nearly metallic nanotubes due to interactions has also been examined by Levitov and Tsvelik [26]. They started from the Luttinger liquid theory of interacting metallic tubes, and added the gap as a perturbing magnetic field. From this approach, which is completely different from ours, they also found that the gap is enhanced by interactions. However, they found

$$\Sigma_{\text{Levitov}} \propto c_s \left(\frac{q_c}{c_s}\right)^{\alpha}, \tag{5.62}$$

where α in the limit of strong interactions is equal to $4/5$. Even though it superficially looks quite different from our theory, it actually has the same qualitative features. $\Sigma_{Levitov}(c_s)$ and $\Sigma_{0,s}(c_s)$ both have negative curvature, go to zero for small c_s, are almost linear for large c_s, and the derivative diverges for small c_s. It would be interesting to examine which physical assumptions lead to the different predictions of the two theories.

If we insert estimated parameters from the end of Chapter 4,

$$\begin{aligned}\Sigma_{0,s}(\zeta,\zeta) &= 0.46\zeta v_F c_s \ln\left(\frac{2\cdot 1000}{10}\right)\\ &= 2.44\zeta v_F c_s.\end{aligned} \tag{5.63}$$

The gap thus increases by more than a factor of 3 due to the Fock diagram. Let us now examine how the Fermi velocity renormalizes. For $c_s \ll k < q_c$,

$$\begin{aligned}\Sigma_{ks}(\zeta,\zeta) &= -gv_F\frac{1}{2}\left(-\frac{\zeta}{k}\left(c_s^2\ln\left(\frac{2(q_c-k)\cdot 2(q_c+k)}{c_s^2}\right)+k\cdot(q_c+k-(q_c-k))\right)\right)\\ &= \zeta g v_F k.\end{aligned} \tag{5.64}$$

The off-diagonal term is, using Eq. (5.58),

$$\Sigma_{ks}(\zeta,-\zeta) = \frac{1}{2}i\zeta\frac{c}{k}\left(-k\ln\left(\frac{2(q_c-k)\cdot 2(q_c+k)}{c_s^2}\right)+2k\right). \tag{5.65}$$

Therefore

$$\frac{\Sigma_{ks}(+,-)\Sigma_{ks}(-,+)}{\mathcal{G}_0(ks-\zeta)^{-1}-\Sigma_{ks}(-\zeta,-\zeta)} \sim \frac{1}{k}, \tag{5.66}$$

which is negligible for large k. The Fermi velocity thus increases by around a factor 1.5 due to interactions.

The self-energy has now been determined to first order in g. In the next section, we will compare this analytical result with a numeric evaluation of the Fock diagram, to evaluate the quality of the approximation Eq. (4.35).

5.5 Test of approximation of $V(q)$

In Section 4.1, the Coulomb interaction $V(q)$ was approximated to be constant up to a high momentum cut-off at $q_c = 1/R$, given by Eq. (4.35). Having now calculated the Fock diagram, it is possible to check this approximation. A less crude approximation is given by Eq. (4.34), which is plotted in Fig. 5.4.

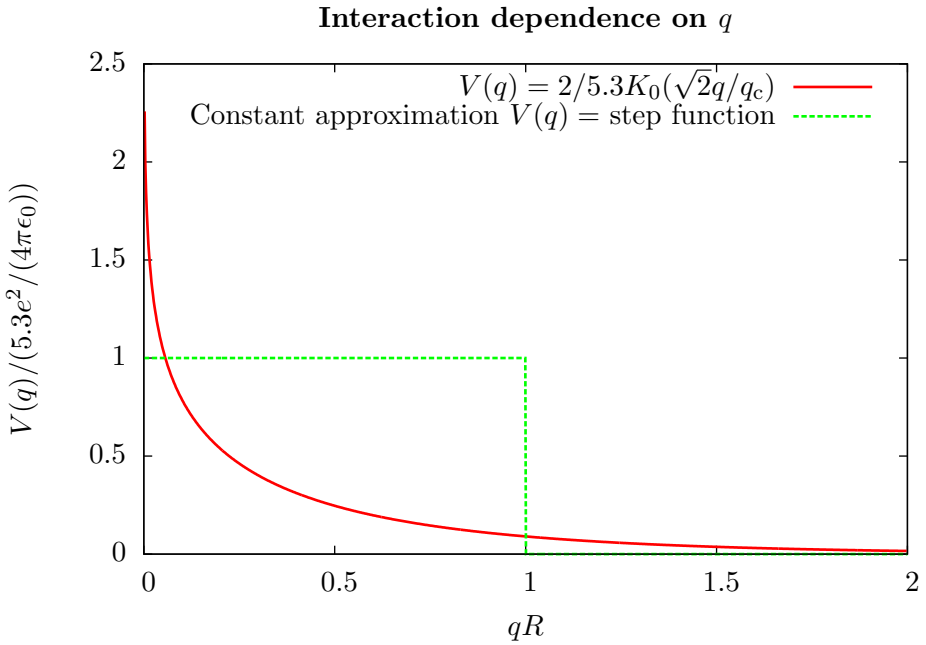

Figure 5.4: The red curve is the function $V(q) = \frac{e^2}{4\pi\epsilon_0} 2K_0(\sqrt{2}q/q_c)$, which is the interaction given by Eq. (4.34). The green curve is the constant potential $V(q) = V_0$ with a cut-off at $q = q_c = 1/R$, defined in Eq. (4.35).

From the figure it is not convincing that this function can be reasonably approximated constant function. However, having found the explicit form of the Fock diagram, we may now numerically calculate how well this approximation holds. For $k = 0$, the approximated Fock self-energy is given by Eq. (5.60). Having this result, it is possible to check the validity of the approximation in Eq. (4.35). If the interaction in the form of Eq. (4.34) is used, we obtain

$$\Sigma_{0,s}(\zeta,\zeta) = \zeta \frac{g}{g_{\text{bare}}} \frac{e^2}{4\pi\epsilon_0} v_F c_s \int dq 2K_0(\sqrt{2}q/q_c) \frac{1}{v_F\sqrt{q^2+c_s^2}}. \tag{5.67}$$

This integral can be evaluated numerically, and the result is shown in Fig. 5.5. The value of V_0 has been determined such that the Bessel function self-energy is the same as the step function self-energy for $q_c = 100c_s$. Even though the approximation does not fit very well to the numerical calculation, it still has the same qualitative features, being negatively curved and with a decreasing curvature as a function of q_c. In Fig. 5.4 it is seen that the

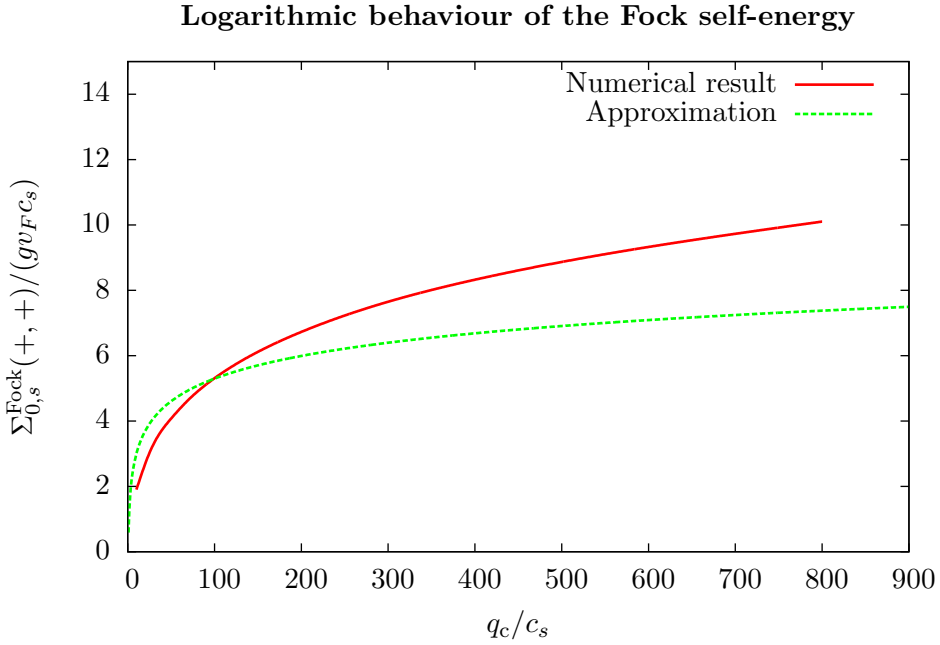

Figure 5.5: The red points are a numerical evaluation of Eq. (5.67). The green curve is Eq. (5.60).

constant interaction is quite different from the Bessel function interaction. The value of the constant interaction seems high compared to the Bessel function. This is because the Fock self-energy is dominated by low momentum terms, so they are weighted higher in the calculation. Given the discrepancy presented in Figs. 5.4 and 5.5, the precision of the interaction strength is quite low, so we estimate $g = 0.45 \pm 0.15$.

5.6 Mean field theory

A way to include higher order perturbation theory is by calculating the diagram shown in Fig. 5.6. The double line corresponds to the renormalized propagator, so this diagram is actually a sum of all diagrams with nested Fock diagrams. This is equivalent to using self-consistent mean field theory in the Hartree-Fock approximation, [24, sec. 4.3]. The unperturbed Hamiltonian is, from Eq. (4.10),

$$\begin{aligned} H_0 &= \sum_{k,s} \boldsymbol{c}^\dagger_{k,s} v_F(c_s\sigma_1 + k\sigma_2)\boldsymbol{c}_{k,s} \\ &= \sum_{k,s} c^\dagger_{k,s,1} v_F(c_s - ik)c_{k,s,2} + c^\dagger_{k,s,2} v_F(c_s + ik)c_{k,s,1} \end{aligned} \tag{5.68}$$

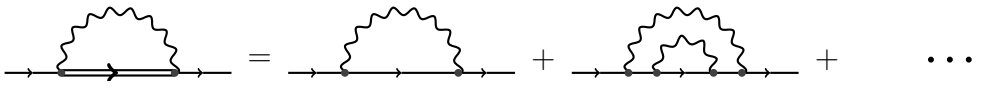

Figure 5.6: Solving the Fock mean-field equation self-consistently corresponds to calculating this diagram.

where $\boldsymbol{c}_{k,s}$ is a two-dimensional column vector in AB space with elements $c_{k,s,1}$ and $c_{k,s,2}$. The interaction Hamiltonian is

$$H_{\text{int}} = \frac{1}{L} \sum_{k_1,k_2,q,s,X,X'} V(q) c^\dagger_{k_1+q,X} c^\dagger_{k_2-q,X'} c_{k_2,X'} c_{k_1,X}. \tag{5.69}$$

Here $X = 1$ represents an A atom and $X = -1$ represents a B atom. In the mean field approximation, we define

$$H_{\text{int}} = H_{\text{Hartree}} + H_{\text{Fock}}. \tag{5.70}$$

When the energies are not found self-consistently, H_{Hartree} has the same band structure as was found by taking only the Hartree diagram into account in the previous section, and the same for Fock, hence the names. When they are solved self-consistently, the energies are equivalent to those found by calculating the double-lined diagram seen in Fig. 5.6.

As seen in Section 5.3, the Hartree term shifts the entire band structure, so it will be neglected. The Fock term is given by

$$\begin{aligned} H_{\text{Fock}} = -\frac{1}{2L} \sum_{k_1,k_2,q,s,X,X'} V(q) (\langle c^\dagger_{k_1+q,s,X} c_{k_2,s,X'} \rangle c^\dagger_{k_2-q,s,X'} c_{k_1,s,X} + \\ \langle c^\dagger_{k_2-q,s,X'}, c_{k_1,s,X} \rangle c^\dagger_{k_1+q,s,X} c_{k_2,s,X'} - \langle c^\dagger_{k_1+q,s,X} c_{k_2,s,X'} \rangle \langle c^\dagger_{k_2-q,s,X'}, c_{k_1,s,X} \rangle). \end{aligned} \tag{5.71}$$

The last term will only shift the band structure in the same way as the Hartree term, so it is not necessary to solve for it self-consistently. Coulomb interactions conserve momentum, which put the constraint

$$\langle c^\dagger_{k_1+q,s,X} c_{k_2,s,X'} \rangle = \delta_{k_1+q,k_2} \langle c^\dagger_{k_1+q,k_1+q} \rangle. \tag{5.72}$$

Therefore

$$\begin{aligned} H_{\text{Fock}} = &- \frac{1}{2L} \sum_{k_1,k_2,q,s,X,X'} V(q) \Big(\langle c^\dagger_{k_1+q,s,X} c_{k_2,s,X'} \rangle c^\dagger_{k_2-q,s,X'} c_{k_1,s,X} & (5.73) \\ &+ \langle c^\dagger_{k_2-q,s,X'}, c_{k_1,s,X} \rangle c^\dagger_{k_1+q,s,X} c_{k_2,s,X'} \Big) & (5.74) \\ = &- \frac{1}{2L} \sum_{k,q,s,X,X'} V(q) \Big(\langle c^\dagger_{k+q,s,X} c_{k+q,s,X'} \rangle c^\dagger_{k,s,X'} c_{k,s,X} & (5.75) \\ &+ \langle c^\dagger_{k-q,s,X'}, c_{k-q,s,X} \rangle c^\dagger_{k,s,X} c_{k,s,X'} \Big), & (5.76) \end{aligned}$$

where k_1+q and k_2 have been replaced by k, since there was only one momentum variable in each term. $V(q)$ is symmetric in q, so q can be replaced by $-q$ in the second term, and X and X' are summation indeces which can be interchanged. Therefore

$$H_{\text{Fock}} = -\frac{1}{L}\sum_{k,q,s,X,X'} V(q)\langle c^\dagger_{k+q,s,X}c_{k+q,s,X'}\rangle c^\dagger_{k,s,X'}c_{k,s,X} \tag{5.77}$$

$$= \frac{1}{L}\sum_{k,s,X,X'}\left(-\sum_q V(q)\langle c^\dagger_{k+q,s,X}c_{k+q,s,X'}\rangle\right) c^\dagger_{k,s,X'}c_{k,s,X} \tag{5.78}$$

$$= \frac{1}{L}\sum_{k,s,X,X'} F_{k,s,X'X}c^\dagger_{k,s,X'}c_{k,s,X}, \tag{5.79}$$

where

$$F_{k,s,X'a} = -\frac{1}{L}\sum_q V(q)\langle c^\dagger_{k+q,s,X}c_{k+q,s,X'}\rangle. \tag{5.80}$$

If $F_{k,s,X'X}$ is viewed as the (X',X)'th element of the matrix $\overline{\overline{F}}_{k,s}$, the full Hamiltonian can be written

$$H = \sum_{k,s}\boldsymbol{c}^\dagger_{k,s}\left(v_F c_s\sigma_1 + v_F k\sigma_2 + \overline{\overline{F}}_{k,s}\right)\boldsymbol{c}_{k,s}. \tag{5.81}$$

$\overline{\overline{F}}_{k,s}$ depends on the eigenstates of the Hamiltonian. Solving the Hamiltonian self-consistently means that the eigenstates of the full Hamiltonian are used to determine $\overline{\overline{F}}_{k,s}$. F can be expanded as

$$\overline{\overline{F}}_{k,s} = F_{k,s,0}\sigma_0 + F_{k,s,1}\sigma_1 + F_{k,s,2}\sigma_2 + F_{k,s,3}\sigma_3. \tag{5.82}$$

We will start by calculating $\overline{\overline{F}}_{k,s}$ to first order, meaning non-self-consistently. This will prove that this is indeed equivalent to the self-energy of the Fock diagram, and at the same time pave the way for the self-consistent calculation.

Since only the lower bands are occupied, the averages are given by

$$\langle c^\dagger_{k+q,s,X'}c_{k+q,s,X}\rangle = \chi^*_{k,s,-,X'}\chi_{k,s,-,X}, \tag{5.83}$$

where $\chi_{k,s,-}$ is the spinor in AB space quantifying to what extent a state in the lower band is a superposition of A and B states, as defined in Eq. (4.7).

5.6.1 Shift term, F_0

The expression for F_0 is

$$F_{k,s,0} = \frac{F_{k,s,11}+F_{k,s,22}}{2} = -\frac{1}{2L}\sum_q V(q)\left(\langle c^\dagger_{k+q,s,1}c_{k+q,s,1}\rangle + \langle c^\dagger_{k+q,s,2}c_{k+q,s,2}\rangle\right). \tag{5.84}$$

From Eqs. (5.83) and (4.7) follows

$$\langle c^\dagger_{k+q,s,1} c_{k+q,s,1}\rangle + \langle c^\dagger_{k+q,s,2} c_{k+q,s,2}\rangle = 1, \tag{5.85}$$

and thus

$$F_{k,s,0} = -\frac{1}{4L}\sum_q V(q)(1+1) = -\frac{1}{2L}\sum_q V(q) = -\frac{V_0 q_c}{2\pi} = -g v_F q_c. \tag{5.86}$$

$F_{k,s,0}$ is multiplied by σ_0 in the Hamiltonian, so it just introduces a momentum and spin independent constant shift of the band structure. In Eq. (5.56), the same constant shift was found, so this result is as expected.

5.6.2 Orthogonal term, F_3

It is seen that

$$F_3 = \frac{F_{11} - F_{22}}{2} = 0, \tag{5.87}$$

since the original Hamiltonian is off-diagonal in AB space, so nothing breaks AB symmetry.

5.6.3 Gap term F_1

The σ_1 term is given by

$$\begin{aligned} F_{k,s,1} &= \frac{F_{k,s,21} + F_{k,s,12}}{2} \\ &= -\frac{1}{2L}\sum_q V(q)\left(\langle c^\dagger_{k+q,s,1} c_{k+q,s,2}\rangle + \langle c^\dagger_{k+q,s,2} c_{k+q,s,1}\rangle\right). \end{aligned} \tag{5.88}$$

From Eqs. (4.7) and (5.83) follows that

$$\begin{aligned} F_{k,s,1} &= -\frac{1}{2L}\sum_q V(q)\frac{1}{2}\frac{-(c_s + i(k+q)) - (c_s - i(k+q))}{\sqrt{c_s^2 + (k+q)^2}} \\ &= \frac{1}{2L}\sum_q V(q)\frac{c_s}{\sqrt{c_s^2 + (k+q)^2}} \\ &= \frac{1}{2}\frac{V_0}{2\pi}\int_{-q_c}^{q_c} dq \frac{c_s}{\sqrt{(k+q)^2 + c_s^2}} \\ &= \frac{1}{2} g v_F \int_{-q_c+k}^{q_c+k} dq \frac{c_s}{\sqrt{q^2 + c_s^2}} \\ &= \frac{1}{2} g v_F \left(2\int_0^{q_c-k} dq \frac{c_s}{\sqrt{q^2 + c_s^2}} + \int_{q_c-k}^{q_c+k} dq \frac{c_s}{\sqrt{q^2 + c_s^2}}\right). \end{aligned} \tag{5.89}$$

The result of this integral is given by Eq. (5.54), so

$$\begin{aligned} F_{k,s,1} =& \frac{1}{2} g v_F \left(2 c_s \ln \left(\frac{\sqrt{(q_c - k)^2 + c_s^2} + q_c - k}{c_s} \right) \right. \\ & \left. + c_s \ln \left(\frac{\sqrt{(q_c + k)^2 + c_s^2} + q_c + k}{\sqrt{(q_c - k)^2 + c_s^2} + q_c - k} \right) \right) \\ =& \frac{1}{2} g v_F c_s \ln \left(\frac{\left(\sqrt{(q_c - k)^2 + c_s^2} + q_c - k \right) \left(\sqrt{(q_c + k)^2 + c_s^2} + q_c + k \right)}{c_s^2} \right). \end{aligned} \tag{5.90}$$

For $q_c \gg k$, $q_c \gg c_s$ this reduces to

$$F_{k,s,1} = g v_F c_s \ln \left(\frac{2 q_c}{c_s} \right), \tag{5.91}$$

identical to Eq. (5.60).

5.6.4 Velocity term, F_2

The last term is

$$\begin{aligned} F_{k,s,2} &= \frac{F_{k,s,21} - F_{k,s,12}}{2i} \\ &= -\frac{1}{2i} \frac{1}{L} \sum_q V(q) \left(\langle c^\dagger_{k+q,s,2} c_{k+q,s,1} \rangle - \langle c^\dagger_{k+q,s,1} c_{k+q,s,2} \rangle \right) \\ &= -\frac{1}{2i} \frac{1}{L} \sum_q V(q) \frac{1}{2} \left(\frac{-(c_s + i(k+q)) + (c_s - i(k+q))}{\sqrt{c_s^2 + (k+q)^2}} \right) \\ &= \frac{1}{2} \frac{1}{L} \sum_q V(q) \left(\frac{k+q}{\sqrt{c_s^2 + (k+q)^2}} \right) \\ &= \frac{1}{2} g v_F \int_{-q_c + k}^{q_c + k} dq \frac{q}{\sqrt{q^2 + c_s^2}}. \end{aligned} \tag{5.92}$$

Using Eq. (5.55), this gives

$$F_{k,s,2} = \frac{1}{2} g v_F \left(\sqrt{(q_c + k)^2 + c_s^2} - \sqrt{(q_c - k)^2 + c_s^2} \right). \tag{5.93}$$

Expanding to linear order in k and c_s,

$$F_{k,s,2} = g v_F k, \tag{5.94}$$

as was also found in Eq. (5.64).

5.7 Self-consistent solution

In the previous section, $\overline{\overline{F}}_{k,s}$ was found using H_0 from Eq. (5.68). To find a self-consistent value of $\overline{\overline{F}}_{k,s}$, one should use H given by Eq. (5.81) to calculate the averages. This gives four integral equations of the four functions $F_{k,s,0}, F_{k,s,1}, F_{k,s,2}, F_{k,s,3}$, which do not have a general solution. However, they can be solved using a few assumptions and approximations. We notice that the constant shift $F_{k,s,0}$ is insignificant, so it will be neglected. That leaves three equations of three functions, instead of four. It is assumed that the true self-consistent solution can be found iteratively. This is done by inserting the non-self-consistent values of $F_{k,s,1}, F_{k,s,2}, F_{k,s,3}$ from Section 5.6 in H, using this H to find some new values of $F_{k,s,1}, F_{k,s,2}, F_{k,s,3}$, reinserting them into H and iterating this process until convergence. It should be noted that in some physical systems, spontaneous symmetry breaking [24, sec. 4.4-4.5] occurs, and thus mean field solutions cannot be found iteratively. However, this is not expected in this case, where the quasiparticles are continuous deformations in the interaction strength of free electrons. We are now ready to calculate the self-consistent mean field value of the parameters. $F_{k,s,2}$ in Eq. (5.94) has the same form as the σ_2 term of H_0, except that v_F is replaced by $(1+g)v_F$. $F_{k,s,1}$ in Eq. (5.91) is independent of k so it is just a rescaling of the gap, with no qualitative change. $F_{k,s,3}$ was found to be zero independently of v_F and c_s. Since $F_{k,s,1}$ and $F_{k,s,2}$ do not change the qualitative behaviour of the Hamiltonian, the iterative process can never generate a non-zero $F_{k,s,3}$ term. Therefore $F_{k,s,3}$ is assumed to be zero in the self-consistent solution. Similarly, $F_{k,s,2}$ is independent of the gap, so it can be solved independently of $F_{k,s,1}$. $F_{k,s,2}$ changes the Hamiltonian in a way equivalent to renormalizing the Fermi velocity, so we define $\tilde{v}_F$ as

$$v_F k + F_{k,s,2} = \tilde{v}_F k. \tag{5.95}$$

Using the full Hamiltonian Eq. (5.81) to calculate $F_{k,s,2}$, we should replace v_F by $\tilde{v}_F$ in Eq. (5.94). In principle g_{bare} depends on v_F, but we assume that long range interactions do not affect short range behaviour. Therefore

$$F_{k,s,2} = \frac{V_0}{2\pi} k. \tag{5.96}$$

Since it is independent of v_F, the first order mean field result is identical to the self-consistent result, so

$$\tilde{v}_F = \frac{v_F}{1-g}. \tag{5.97}$$

The renormalized Fermi velocity has to be incorporated in H before we can calculate the self-consistent value of c_s. The Hamiltonian has now become

$$H = \sum_{k,s} \boldsymbol{c}^\dagger_{k,s} \left(v_F c_s \sigma_1 + \tilde{v}_F k \sigma_2 + F_{k,s,1} \right) \boldsymbol{c}_{k,s}. \tag{5.98}$$

It is not exactly in the same form as the Eq. (5.81) because the Fermi velocities v_F and $\tilde{v}_F$ in the two terms differ. If we introduce $c_s' = \frac{v_F}{\tilde{v}_F} c_s$, we find that

$$H = \sum_{k,s} \boldsymbol{c}_{k,s}^\dagger \left(\tilde{v}_F c_s' \sigma_1 + \tilde{v}_F k \sigma_2 + F_{k,s,1} \right) \boldsymbol{c}_{k,s}. \tag{5.99}$$

With this definition,

$$F_{k,s,1} = g \tilde{v}_F c_s \ln \left(\frac{2q_c}{c_s} \right). \tag{5.100}$$

To find the renormalized gap, a self-consistency equation equivalent to Eq. (5.95) is used,

$$v_F c_s + g v_F \tilde{c}_s \ln \left(\frac{2q_c}{\tilde{c}_s} \right) = v_F \tilde{c}_s. \tag{5.101}$$

This equation converges for

$$g \ln \left(\frac{2q_c}{\tilde{c}_s} \right) < 1. \tag{5.102}$$

As $g \ln \left(\frac{2q_c}{\tilde{c}_s} \right)$ approaches 1, it diverges, so mean field theory breaks down. First we will however solve the mean field problem assuming that $g \ln \left(\frac{2q_c}{\tilde{c}_s} \right) < 1$. By renaming

$$\tilde{c}_s = (1 + \beta) c_s \tag{5.103}$$

and assuming small β, Eq. (5.101) reduces to

$$\begin{aligned} 1 + g(1+\beta) \ln \left(\frac{2q_c}{(1+\beta)c_s} \right) &= 1 + \beta \\ \Rightarrow g(1+\beta) \left(\ln \left(\frac{2q_c}{c_s} \right) - \beta \right) &= \beta \\ \Rightarrow g \ln \left(\frac{2q_c}{c_s} \right) - g\beta + g\beta \ln \left(\frac{2q_c}{c_s} \right) &= \beta \\ \Rightarrow \beta = \frac{g \ln \left(\frac{2q_c}{c_s} \right)}{1 + g \left(1 - \ln \left(\frac{2q_c}{c_s} \right) \right)}. \end{aligned} \tag{5.104}$$

The gap is thus changed from $v_F c_s$ to

$$v_F \tilde{c}_s = v_F c_s \left(1 + \frac{g \ln \left(\frac{2q_c}{c_s} \right)}{1 + g \left(1 - \ln \left(\frac{2q_c}{c_s} \right) \right)} \right). \tag{5.105}$$

Since

$$\ln \left(\frac{2q_c}{c_s} \right) > 1, \tag{5.106}$$

the gap grows more than in the non-self-consistent case Eq. (5.91).

In Eq. (5.63) it was shown that for tubes with no dielectric screening, i.e. suspended tubes, $g \ln\left(\frac{2q_c}{c_s'}\right) < 1$ is not satisfied, so the mean field calculation breaks down. However, screening can contribute by as much as a factor 10 for the right substrate, so the regime where Eq. (5.105) is valid is experimentally realizable. If Eq. (5.102) is not satisfied, mean field theory is not valid. It is seen that this happens if g is to large, i.e. interactions are strong. For large g perturbation theory in general breaks down, because higher order diagrams contribute more than lower order diagrams, leading to a divergent sum of diagrams.

Chapter 6

Higher order Coulomb interactions

In the previous chapter it was shown that mean field calculations break down due to the large interaction strength. Below we will show that higher order diagrams, especially those entering the random phase approximation, screen the interaction. This reduces the interaction strength, such that the perturbation series rapidly converges.

6.1 The pair bubble

As for the Fock diagram, the pair bubble self-energy is a two times two matrix. It is given by

$$\begin{aligned}\Sigma^{\mathrm{pb}}_{ks}(\zeta_i,\zeta_o) =& -\frac{1}{\beta^2}\int\frac{dq}{2\pi}\int\frac{dp}{2\pi}\sum_{s'}\sum_{\zeta,iq_n,\zeta',ip_n,\zeta''}(-V(q))^2\mathcal{G}_0(k+q,s,\zeta)\\ &\mathcal{G}_0(p,s',\zeta')\mathcal{G}_0(p-q,s',\zeta'')w_{k,k+q,s,\zeta_i\zeta}w_{k+q,k,s,\zeta\zeta_o}\left|w_{p-q,p,s',\zeta'\zeta''}\right|^2\\ =& -\left(\frac{V_0}{2\pi}\right)^2\int_{-q_c}^{q_c}dq\int dp\sum_{s'}\sum_{\zeta,\zeta',\zeta''}\Bigg(w_{k,k+q,s,\zeta_i\zeta}w_{k+q,k,s,\zeta\zeta_o}\left|w_{p-q,p,s',\zeta'\zeta''}\right|^2\\ &\frac{1}{\beta^2}\sum_{iq_n,ip_n}\mathcal{G}_0(k+q,s,\zeta)\mathcal{G}_0(p,s',\zeta')\mathcal{G}_0(p-q,s',\zeta'')\Bigg).\end{aligned}\tag{6.1}$$

It can be seen in diagram form in Fig. 6.1.

We will start by evaluating the Matsubara sums. The sum of the free frequency in the

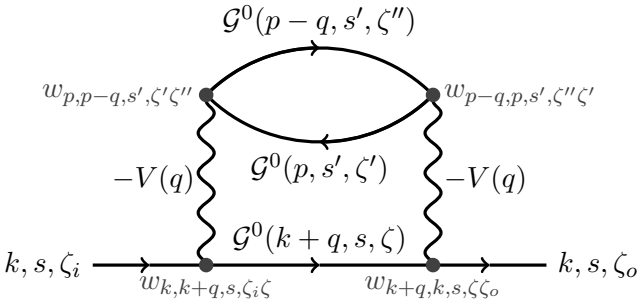

Figure 6.1: The pair bubble diagram.

bubble is

$$\begin{aligned}\frac{1}{\beta}\sum_{ip_n}\mathcal{G}_0(p,s',\zeta')\mathcal{G}_0(p-q,s',\zeta'') &= \frac{1}{\beta}\sum_{ip_n}\frac{1}{ip_n-\zeta'\xi_{p,s'}}\frac{1}{ip_n-iq_n-\zeta''\xi_{p-q,s'}}\\ &= \frac{1}{\beta}\sum_{ip_n}\frac{1}{ip_n-\zeta'\xi_{p,s'}}\frac{1}{ip_n-iq_n-\zeta''\xi_{p-q,s'}}\\ &= \frac{n_F(\zeta''\xi_{p-q,s'})}{iq_n+\zeta''\xi_{p-q,s'}-\zeta'\xi_{p,s'}}+\frac{n_F(\zeta'\xi_{p,s'})}{\zeta'\xi_{p,s'}-iq_n-\zeta''\xi_{p-q,s'}}\\ &= \frac{n_F(\zeta''\xi_{p-q,s'})-n_F(\zeta'\xi_{p,s'})}{iq_n+\zeta''\xi_{p-q,s'}-\zeta'\xi_{p,s'}}. \end{aligned} \tag{6.2}$$

The second Matsubara sum can now be evaluated,

$$\begin{aligned}&\frac{1}{\beta^2}\sum_{iq_n,ip_n}\mathcal{G}_0(k+q,s,\zeta)\mathcal{G}_0(p,s',\zeta')\mathcal{G}_0(p-q,s',\zeta'')\\ &=\sum_{iq_n}\frac{1}{iq_n+ik_n-\zeta\xi_{q+k,s}}\frac{n_F(\zeta''\xi_{p-q,s'})-n_F(\zeta'\xi_{p,s'})}{iq_n+\zeta''\xi_{p-q,s'}-\zeta'\xi_{p},s'}\\ &=(n_F(\zeta''\xi_{p-q,s'})-n_F(\zeta'\xi_{p,s'}))\frac{n_F(\zeta'\xi_{p,s'}-\zeta''\xi_{p-q,s'})-n_F(\zeta\xi_{q+k,s})}{\zeta'\xi_{p,s'}-\zeta''\xi_{p-q,s'}-\zeta\xi_{q+k,s}+ik_n}. \end{aligned} \tag{6.3}$$

As before, n_F is one when its argument is negative and zero when it is positive. Therefore the terms are zero unless $\zeta'=-\zeta''$ and $\zeta=\zeta''$. This gives

$$\begin{aligned}\Sigma^{\mathrm{pb}}_{ks}(\zeta_i,\zeta_o) &= -\left(\frac{V_0}{2\pi}\right)^2\int_{-q_c}^{q_c}dq\int dp\sum_{s'}\sum_{\zeta,\zeta',\zeta''}w_{k,k+q,s,\zeta_i\zeta}w_{k+q,k,s,\zeta\zeta_o}\left|w_{p-q,p,s',\zeta'\zeta''}\right|^2\\ &\qquad(n_F(\zeta''\xi_{p-q,s'})-n_F(\zeta'\xi_{p,s'}))\frac{n_F(\zeta'\xi_{p,s'}-\zeta''\xi_{p-q,s'})-n_F(\zeta\xi_{q+k,s})}{\zeta'\xi_{p,s'}-\zeta''\xi_{p-q,s'}-\zeta\xi_{q+k,s}+ik_n}\\ &=\left(\frac{V_0}{2\pi}\right)^2\int_{-q_c}^{q_c}dq\int dp\sum_{s'}\left(\left|w_{p-q,p,s',-}\right|^2\right.\\ &\qquad\left.\left(\frac{w_{k,k+q,s,-\zeta_i}w^*_{k,k+q,s,-\zeta_o}}{\xi_{p-q,s'}+\xi_{p,s'}+\xi_{q+k,s}+ik_n}+\frac{w_{k,k+q,s,\zeta_i}w^*_{k,k+q,s,\zeta_o}}{-\xi_{p-q,s'}-\xi_{p,s'}-\xi_{q+k,s}+ik_n}\right)\right). \end{aligned} \tag{6.4}$$

We rotate back to real frequencies by substituting ik_n with $\omega + i\eta$. The frequency ω corresponds to the energy of the state, and it is positive for states in the upper band.

$\Sigma^{\rm pb}_{ks}(\zeta_i, \zeta_o)$ is odd under the transformation $\omega \to -\omega$, $\zeta_i \to -\zeta_i$, $\zeta_o \to -\zeta_o$, so the electron and hole state energies are shifted by the same amount in opposite directions. This means that if the electron energy is decreased, the hole energy is also decreased, so the gap gets smaller. It is thus not necessary to evaluate Eq. (6.4) for both electrons and holes. We will now analyze the self-energy for the state $k = 0$, to examine how the gap is renormalized. For $\zeta_i = -\zeta_o$, the overlaps in the numerator are

$$\begin{aligned} w_{q,0,s,+} w^*_{q,0,s,-} =& \frac{1}{4}\left(1 + \frac{c_s - iq}{\sqrt{c_s^2 + q^2}}\right)\left(1 - \frac{c_s + iq}{\sqrt{c_s^2 + q^2}}\right) \\ =& \frac{-2iq}{\sqrt{c_s^2 + q^2}}. \end{aligned} \tag{6.5}$$

Since the rest of the integrand is an even function of q,

$$\Sigma^{\rm pb}_{0,s}(+,-) = \Sigma^{\rm pb}_{0,s}(-,+) = 0. \tag{6.6}$$

For $\Sigma^{\rm pb}_{0,s}(+,+)$, Eq. (6.4) reduces to

$$\begin{aligned} \Sigma^{\rm pb}_{0,s}(+,+) = \left(\frac{V_0}{2\pi}\right)^2 \int_{-q_{\rm c}}^{q_{\rm c}} dq \int dp \sum_{s'} \left|w_{p-q,p,s',-}\right|^2 \\ \left(\frac{|w_{q,0,s,-}|^2}{\xi_{p-q,s'} + \xi_{p,s'} + \xi_{q,s} + \tilde{v}_F \tilde{c}_s} + \frac{|w_{q,0,s,+}|^2}{-\xi_{p-q,s'} - \xi_{p,s'} - \xi_{q,s} + \tilde{v}_F \tilde{c}_s}\right). \end{aligned} \tag{6.7}$$

Using

$$\left|w_{p-q,p,s',-}\right|^2 > 0, \tag{6.8}$$

$$|w_{q,0,s,+}|^2 > |w_{q,0,s,-}|^2 > 0, \tag{6.9}$$

$$\xi_{p-q,s'} + \xi_{p,s'} + \xi_{q,s} > \tilde{v}_F \tilde{c}_s, \tag{6.10}$$

it is seen that $\Sigma^{\rm pb}_{0,s}(+,+)$, is negative. This is also what was expected, since second order perturbation theory is known to lower the ground state of a quantum mechanical system [10, Eq. (6.15)].

6.1.1 Approximate evaluation

Eq. (6.4) can not be evaluated analytically, but for $k = 0$ it is possible to make a reasonable approximation. Let us start with the pair bubble,

$$\begin{aligned}
\Pi^0(q, iq_n) \equiv & -\int \frac{dp}{2\pi} \sum_{s'} \sum_{\zeta',\zeta''} \left| w_{p-q,p,s',\zeta'\zeta''} \right|^2 \frac{1}{\beta} \sum_{ip_n} \mathcal{G}_0(p, s', \zeta') \mathcal{G}_0(p-q, s', \zeta'') \\
= & -\int \frac{dp}{2\pi} \sum_{s'} \sum_{\zeta',\zeta''} \left| w_{p-q,p,s',\zeta'\zeta''} \right|^2 \frac{n_F(\zeta''\xi_{p-q,s'}) - n_F(\zeta'\xi_{p,s'})}{iq_n + \zeta''\xi_{p-q,s'} - \zeta'\xi_{p,s'}} \\
= & -\int \frac{dp}{2\pi} \sum_{s'} \sum_{\zeta'} \left| w_{p-q,p,s',-} \right|^2 \frac{\zeta'}{iq_n - \zeta'(\xi_{p-q,s'} + \xi_{p,s'})} \\
= & \int \frac{dp}{2\pi} \sum_{s'} \left| w_{p-q,p,s',-} \right|^2 \left(\frac{1}{\xi_{p-q,s'} + \xi_{p,s'} - iq_n} + \frac{1}{\xi_{p-q,s'} + \xi_{p,s'} + iq_n} \right) \\
= & -\int \frac{dp}{2\pi} \sum_{s'} \left| w_{p-q,p,s',-} \right|^2 \frac{2(\xi_{p-q,s'} + \xi_{p,s'})}{(iq_n - \xi_{p-q,s'} - \xi_{p,s'})(iq_n + \xi_{p-q,s'} + \xi_{p,s'})} \\
= & \int \frac{dp}{2\pi} \sum_{s'} \left| w_{p-q,p,s',-} \right|^2 \frac{2(\xi_{p-q,s'} + \xi_{p,s'})}{(\xi_{p-q,s'} + \xi_{p,s'})^2 - (iq_n)^2}.
\end{aligned} \tag{6.11}$$

From Eqs. (4.50) and (4.51) it is seen that the difference between the gap of spin up and down electrons is two orders of magnitude smaller than the size of the gap. Therefore, in the following, we will approximate $c_s = c_{-s}$. In this approximation the sum over spin just counts the number of cones, N_f, which is equal to 4. In Eq. (6.4) we see that the integrand is symmetric in q, so it is only necessary to analyze it for positive q. The overlap factor is, from Eq. (4.18),

$$\begin{aligned}
|w_{p-q,p,s',-}|^2 = & \left| \frac{1}{2} \left(1 - \frac{c_{s'} - i(p-q)}{\sqrt{c_{s'}^2 + (p-q)^2}} \frac{c_{s'} + ip}{\sqrt{c_{s'}^2 + p^2}} \right) \right|^2 \\
= & \frac{1}{2} \left(1 - \frac{c_{s'}^2 + (p-q)p}{\sqrt{c_{s'}^2 + (p-q)^2}\sqrt{c_{s'}^2 + p^2}} \right).
\end{aligned} \tag{6.12}$$

Since most of the integration region has momenta much larger than c_s, and no divergences are expected for small momenta, to first order in $c_{s'}$ the overlap is

$$\begin{aligned}
|w_{p-q,p,s',-}|^2 \approx & \frac{1}{2} \left(1 - \frac{(p-q)p}{|(p-q)p|} \right) \\
\approx & \begin{cases} 1 & \text{for} \quad p \in [0, q], \\ 0 & \text{otherwise} \end{cases}.
\end{aligned} \tag{6.13}$$

Furthermore, for $q \ll c_s$, we find $|w_{p-q,p,s',-}|^2 \ll 1$, so we approximate $|w_{p-q,p,s',-}|^2 = 0$ for $q < c_{s'}$. For large q and p we may approximate the energy denominator of Eq. (6.4)

$$\xi_{p-q,s'} + \xi_{p,s'} \approx v_F(|p-q| + |p|) = v_F q. \tag{6.14}$$

Therefore

$$\begin{aligned}\Pi^0(q,iq_n) \approx& \int_0^q \frac{dp}{2\pi} N_f \frac{2v_F q}{v_F^2 q^2 - (iq_n)^2} \\ =& \frac{1}{2\pi} N_f \frac{2v_F q^2}{v_F^2 q^2 - (iq_n)^2}.\end{aligned} \tag{6.15}$$

Using this, we find for the self-energy

$$\begin{aligned}\Sigma^{\rm pb}_{0,s}(+,+) =& V_0^2 \int_{-q_c}^{q_c} \frac{dq}{2\pi} \frac{1}{\beta} \sum_{iq_n} \sum_{\zeta} \Pi^0(q,iq_n) \left|w_{0,q,s,\zeta}\right|^2 \mathcal{G}_0(q,s,\zeta) \\ \approx& -g^2 v_F^2 2 \int_{c_s}^{q_c} dq \frac{1}{\beta} \sum_{iq_n} \sum_{\zeta} \left(N_f \frac{2v_F q^2}{(iq_n + v_F q)(iq_n - v_F q)} \right. \\ & \left. \left|w_{0,q,s,\zeta}\right|^2 \frac{1}{iq_n + ik_n - \zeta\xi_{q,s}} \right) \\ =& -g^2 v_F \int_{c_s}^{q_c} dq 4 v_F^2 q^2 \sum_{\zeta} N_f \left|w_{0,q,s,\zeta}\right|^2 \left(\frac{1}{-2v_F q(-v_F q + ik_n - \zeta\xi_{q,s})} \right. \\ & \left. \frac{n_F(\zeta\xi_{q,s})}{(-ik_n + \zeta\xi_{q,s} + v_F q)(-ik_n + \zeta\xi_{q,s} - v_F q)} \right) \\ =& -g^2 v_F \int_{c_s}^{q_c} dq 4 v_F^2 q^2 N_f \left(\sum_{\zeta} \frac{\left|w_{0,q,s,\zeta}\right|^2}{-2v_F q(-v_F q + ik_n - \zeta\xi_{q,s})} \right. \\ & \left. \frac{\left|w_{0,q,s,-}\right|^2}{(-ik_n - \xi_{q,s} + v_F q)(-ik_n - \xi_{q,s} - v_F q)} \right).\end{aligned} \tag{6.16}$$

Approximating the energies according to Eq. (6.14) yields

$$\begin{aligned}\Sigma^{\rm pb}_{0,s}(+,+) \approx& -g^2 v_F \int_{c_s}^{q_c} dq 4 v_F^2 q^2 N_f \\ & \left(\frac{\left|w_{0,q,s,-}\right|^2}{ik_n(ik_n + 2v_F q)} + \frac{\left|w_{0,q,s,+}\right|^2}{2v_F q(2v_F q - ik_n)} + \frac{\left|w_{0,q,s,-}\right|^2}{-2v_F q(ik_n)} \right).\end{aligned} \tag{6.17}$$

Analyzing the remaining overlap factors similar Eq. (6.12), we obtain

$$\begin{aligned}\left|w_{0,q,s,\zeta}\right|^2 =& \left| \frac{1}{2} \left(1 + \zeta \frac{c_s + iq}{\sqrt{c_s^2 + q^2}} \right) \right|^2 \\ \approx& \frac{1}{2} \left(1 + \zeta \frac{c_s}{q} \right).\end{aligned} \tag{6.18}$$

The self-energy thus reduces to

$$\begin{aligned}
\Sigma^{\mathrm{pb}}_{0,s}(+,+) \approx & -g^2 v_F \int_{c_s}^{q_c} dq v_F q N_f \\
& \left(\frac{2v_F q}{ik_n(ik_n + 2v_F q)} + \frac{1}{2v_F q - ik_n} + \frac{1}{-ik_n} \right. \\
& \left. - \frac{2v_F c_s}{ik_n(ik_n + 2v_F q)} + \frac{c_s}{q(2v_F q - ik_n)} + \frac{c_s}{q(ik_n)} \right) \\
= & -g^2 v_F \int_{c_s}^{q_c} dq v_F q N_f \\
& \left(-\frac{1}{ik_n + 2v_F q} + \frac{1}{2v_F q - ik_n} \right. \\
& \left. \frac{c_s}{q(ik_n + 2v_F q)} + \frac{c_s}{q(2v_F q - ik_n)} \right) \\
= & -g^2 v_F \int_{c_s}^{q_c} dq 2v_F q N_f \\
& \left(\frac{ik_n}{(2v_F q)^2 - (ik_n)^2} + \frac{2v_F c_s}{(2v_F q)^2 - (ik_n)^2} \right) \\
= & -g^2 (ik_n + 2v_F c_s) \frac{1}{2} N_f \int_{2v_F c_s}^{2v_F q_c} d(2v_F q) \frac{2v_F q}{(2v_F q)^2 - (ik_n)^2}.
\end{aligned} \tag{6.19}$$

Rotating back to real frequencies $ik_n \to \omega$ and using

$$\int dq \frac{q}{q^2 + c^2} = \frac{1}{2} \ln\left(q^2 + c^2\right), \tag{6.20}$$

this becomes

$$\Sigma^{\mathrm{pb}}_{0,s}(+,+) \approx -\frac{1}{4} g^2 N_f (\omega + 2v_F c_s) \ln\left(\frac{4v_F^2 q_c^2 - \omega^2}{4v_F^2 c_s^2 - \omega^2} \right). \tag{6.21}$$

The frequency ω should be found self-consistently via

$$\begin{aligned}
\omega = & v_F c_s + \Sigma^{\mathrm{Fock}} + \Sigma^{\mathrm{pb}} \\
\Rightarrow \omega = & \frac{1 + g \ln(2q_c/c_s) - g^2 N_f \ln\left(\sqrt{(4v_F^2 q_c^2 - \omega^2)/(4v_F^2 c_s^2 - \omega^2)} \right)}{1 + 1/2 g^2 N_f \ln\left(\sqrt{(4v_F^2 q_c^2 - \omega^2)/(4v_F^2 c_s^2 - \omega^2)} \right)} v_F c_s.
\end{aligned} \tag{6.22}$$

We see that for $gN_f > 1$ and sufficiently small c_s, ω is negative. This is unphysical, since at $\omega = 0$, the gap has closed, so our theory breaks down. From Eq. (4.47) $gN_f = 1.84$, so self-consistent perturbation theory breaks down, as was found in Section 5.7. However, to check the validity of our approximations, we will assume $gN_f < 1$, and compare this result to numerical calculations. Using $\omega = v_F c_s$, we get

$$\Sigma^{\mathrm{pb}}_{0,s}(+,+) \approx -g^2 v_F c_s \frac{3}{2} N_f \ln\left(\sqrt{\frac{4}{3}} \frac{q_c}{c_s} \right). \tag{6.23}$$

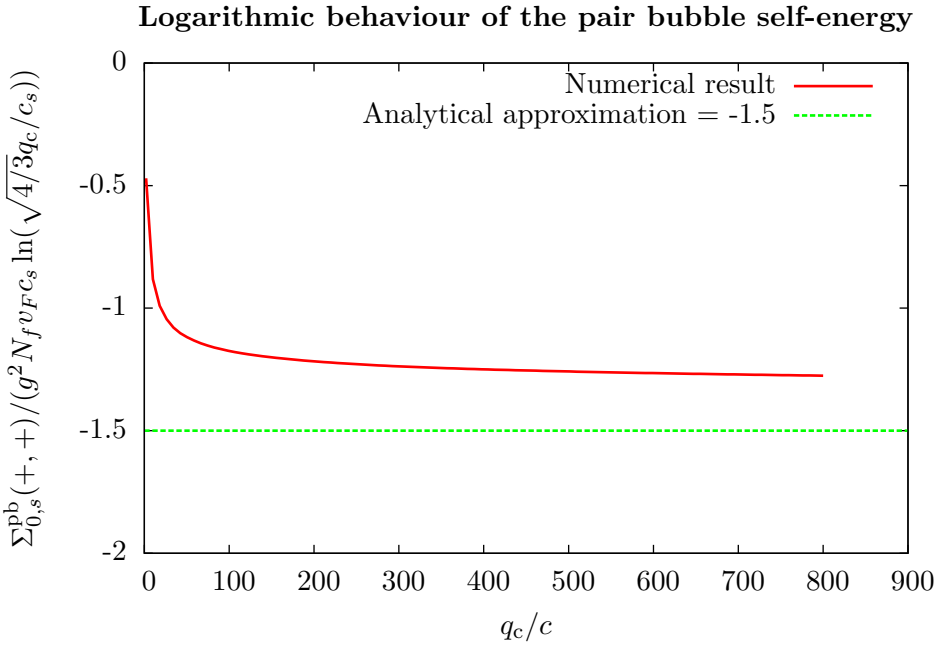

Figure 6.2: The red curve is a numerical calculation of $\Sigma^{\rm pb}_{0,s}(+,+)/(g\Sigma^{\rm Fock}_{0,s}(+,+))$ using Eq. (6.7). The green line is the analytically calculated value of $\Sigma^{\rm pb}_{0,s}(+,+)/(g\Sigma^{\rm Fock}_{0,s}(+,+)) = -\frac{3}{2}$ using the approximations leading to Eq. (6.23). For $q_c/c_s = 10^5$, the numerical result is -1.33. Together with the observed trend, this indicates that the numerical calculation converges logarithmically to the analytical result.

A numerical evaluation of $\Sigma^{\rm pb}_{0,s}(+,+)$ is shown in Fig. 6.2. In the limit of large $q_{\rm c}/c_s$, the exact numerical result is equal to the analytical approximation Eq. (6.23). In the regime we usually work in, $q_{\rm c}/c_s \in [50, 1000]$, the approximation is about 25% larger than the exact result. The numerical result has thus not yet converged to the numerical result. Since the difference between approximation and exact result is quite small, we will continue to work with this approximation for the pair bubble.

For the perturbation series to be convergent, the size of the diagrams has to decrease as the order increases. Comparing Eq. (6.23) and Eq. (5.60), it is seen that the pair bubble self-energy is approximately a factor gN_f larger than the Fock self-energy. Since N_f is equal to 4 for a nanotube, g has to be less than 1/4 for the pair bubble self-energy to be less than the first order self-energy. This does not seem to be the case for an unscreened interaction, see Eq. (4.47). We therefore anticipate that the diagrams do not get smaller when we go to higher order in perturbation theory. A different approach is therefore needed. We will see in Section 6.3 that the random phase approximation leads to a screened interaction, ensuring convergence of the perturbative expansion. First, however, we will look at the second order exchange diagram.

6.2 The exchange diagram

The exchange diagram, as shown in Fig. 6.3, is given by the analytical expression

$$\begin{aligned}\Sigma^{\rm Exchange}_{ks}(\zeta_i,\zeta_o) =& -\frac{1}{\beta^2}\int\frac{dq}{2\pi}\int\frac{dp}{2\pi}\sum_{s'}\sum_{\zeta,iq_n,\zeta',iq'_n,\zeta''}(-V(q))(-V(q'))\\ &\mathcal{G}_0(k+q,s,\zeta)\mathcal{G}_0(k+q',s,\zeta')\mathcal{G}_0(k+q+q',s,\zeta'')\\ &w_{k,k+q,s,\zeta_i\zeta}w_{k+q,k+q+q',s,\zeta\zeta''}w_{k+q+q',k+q',s,\zeta'\zeta''}w_{k+q',k,s,\zeta'\zeta_o}\\ =&\left(\frac{V_0}{2\pi}\right)\int_{-q_{\rm c}}^{q_{\rm c}}dq\int_{-q_{\rm c}}^{q_{\rm c}}dq'\sum_{\zeta,\zeta',\zeta''}(\\ &w_{k,k+q,s,\zeta_i\zeta}w_{k+q,k+q+q',s,\zeta\zeta''}w_{k+q+q',k+q',s,\zeta'\zeta''}w_{k+q',k,s,\zeta'\zeta_o}\\ &\mathcal{G}_0(k+q,s,\zeta)\mathcal{G}_0(k+q',s,\zeta')\mathcal{G}_0(k+q+q',s,\zeta'')).\end{aligned}\tag{6.24}$$

The first Matsubara sum is evaluated as in Eq. (6.2) with p replaced by $k+q'$, q by $-q$ and ik_n absorbed into iq'_n, which gives

$$\frac{1}{\beta}\sum_{iq'_n}\mathcal{G}_0(k+q',s,\zeta')\mathcal{G}_0(k+q+q',s,\zeta'') = \frac{n_F(\zeta'\xi_{k+q',s})-n_F(\zeta''\xi_{k+q+q',s})}{iq_n-\zeta''\xi_{k+q+q',s}+\zeta'\xi_{k+q',s}}.\tag{6.25}$$

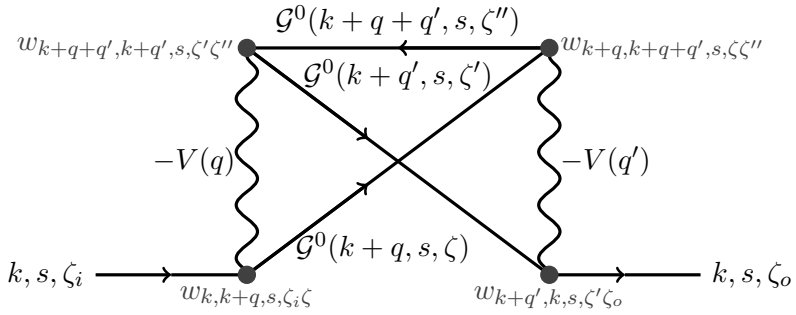

Figure 6.3: The exchange diagram.

The second Matsubara sum is evaluated as Eq. (6.3), with opposite signs on ζ' and ζ'',

$$\begin{aligned}
&\frac{1}{\beta^2}\sum_{iq_n,iq'_n}\mathcal{G}_0(k+q,s,\zeta)\mathcal{G}_0(k+q',s,\zeta')\mathcal{G}_0(k+q+q',s,\zeta'')\\
&=(n_F(\zeta'\xi_{k+q',s})-n_F(\zeta''\xi_{k+q+q',s}))\frac{n_F(\zeta''\xi_{k+q+q'}-\zeta'\xi_{k+q',s})-n_F(\zeta\xi_{k+q,s})}{-\zeta'\xi_{k+q',s}+\zeta''\xi_{k+q+q'}-\zeta\xi_{k+q,s}+ik_n}\\
&=-\frac{1}{-\zeta'\xi_{k+q',s}+\zeta''\xi_{k+q+q'}-\zeta\xi_{k+q,s}+ik_n}\delta_{\zeta\zeta'}\delta_{\zeta,-\zeta''}\,. \qquad (6.26)
\end{aligned}$$

Therefore

$$\begin{aligned}
\Sigma^{\text{Exchange}}_{ks}(\zeta_i,\zeta_o)=&-\left(\frac{V_0}{2\pi}\right)^2\int_{-q_c}^{q_c}dq\int_{-q_c}^{q_c}dq'\left(w_{k+q,k+q+q',s,-}w_{k+q+q',k+q',s,-}\right.\\
&\left.\left(\frac{w_{k,k+q,s,\zeta_i}w^*_{k,k+q',s,\zeta_o}}{-\xi_{k+q',s}-\xi_{k+q+q'}-\xi_{k+q,s}+ik_n}+\frac{w_{k,k+q,s,-\zeta_i}w^*_{k,k+q',s,-\zeta_o}}{\xi_{k+q',s}+\xi_{k+q+q'}+\xi_{k+q,s}+ik_n}\right)\right). \qquad (6.27)
\end{aligned}$$

6.2.1 Approximate evaluation

As for the pair bubble, we will evaluate the exchange diagram approximately for $k=0$. Let us start by approximating the overlaps in the large q,q' regime, so

$$\begin{aligned}
w_{q,q+q',s,-}w_{q+q',q',s,-}&=\frac{1}{4}\left(1-\frac{c_s-iq}{\sqrt{c_s^2+q^2}}\frac{c_s+i(q+q')}{\sqrt{c_s^2+(q+q')^2}}\right)\\
&\quad\left(1-\frac{c_s-i(q+q')}{\sqrt{c_s^2+(q+q')^2}}\frac{c_s+iq'}{\sqrt{c_s^2+q'^2}}\right)\\
&\approx\frac{1}{4}\left(1-\frac{q}{|q|}\frac{q+q'}{|q+q'|}\right)\left(1-\frac{q+q'}{|q+q'|}\frac{q'}{|q'|}\right)\\
&=0. \qquad (6.28)
\end{aligned}$$

The exchange diagram is thus expected to be much smaller than the pair bubble. A numerical calculation with $q_c=100c_s$ gives

$$\Sigma^{\text{Exchange}}_{ks}(+,+)=0.011g^2v_Fc_s. \qquad (6.29)$$

It is thus three orders of magnitude smaller than the pair bubble Eq. (6.23), confirming that it is negligible. It has the opposite sign of the pair bubble as expected.

6.3 Random phase approximation

In Section 6.1 it was shown that the second order diagram is larger than the first order diagram due to the sum $\sum_s = 4$. This factor arise because the electron hole pair in the fermion loop can exist in all four cones. For higher order diagrams, we deduce that if a diagram has m fermion loops, it has a prefactor $N_f^m = 4^m$. An n'th order diagram with m loops is thus proportional to $g^n N_f^m$. For each n there is one diagram with $m = n$, and the rest have $m < n$. The diagram with $m = n$ must therefore be the most important. They are shown in Fig. 6.4. The number of diagrams scales rapidly with n. Therefore one would naively expect the sum of rest of the diagrams to be much larger than the $m = n$ diagram after the first few values of n. However, since there is no general argument for the rest of the diagrams to have the same sign, one expect them to have a random phase, hence the name. On average they thus cancel, and using only the $m = n$ diagrams is a good approximation. This is also called the $1/N_f$ expansion. The $1/N_f$ expansion has already been applied to graphene [27].

The sum of all diagrams with $m = n$ can be evaluated as a Fock diagram with a renormalized interaction line, where the renormalized interaction is given by [24, p. 250]

$$V^{\mathrm{RPA,tot}}(q, iq_n) = \frac{V(q)}{1 + V(q)\Pi^0(q, iq_n)}. \tag{6.30}$$

Inserting $\Pi^0(q, iq_n)$ from Eq. (6.15) gives

$$\begin{aligned} V^{\mathrm{RPA,tot}}(q, iq_n) =& \frac{V(q)}{1 + \frac{1}{2\pi}V(q)N_f \frac{2v_F q^2}{v_F^2 q^2 - (iq_n)^2}} \\ =& V(q)\frac{v_F^2 q^2 - (iq_n)^2}{v_F^2 q^2 - (iq_n)^2 + 2gN_f v_F^2 q^2} \\ =& V(q)\left(1 - \frac{2gN_f v_F^2 q^2}{v_F^2 q^2 - (iq_n)^2 + 2gN_f v_F^2 q^2}\right) \\ =& V(q)\left(1 + \frac{2gN_f v_F^2 q^2}{(iq_n - \alpha v_F q)(\alpha v_F q + iq_n)}\right), \end{aligned} \tag{6.31}$$

where

$$\alpha = \sqrt{1 + 2gN_f}. \tag{6.32}$$

The RPA interaction is thus equal to the original interaction plus an extra negative term,

$$V^{\mathrm{RPA,tot}}(q, iq_n) = V(q) + V^{\mathrm{RPA}}(q, iq_n). \tag{6.33}$$

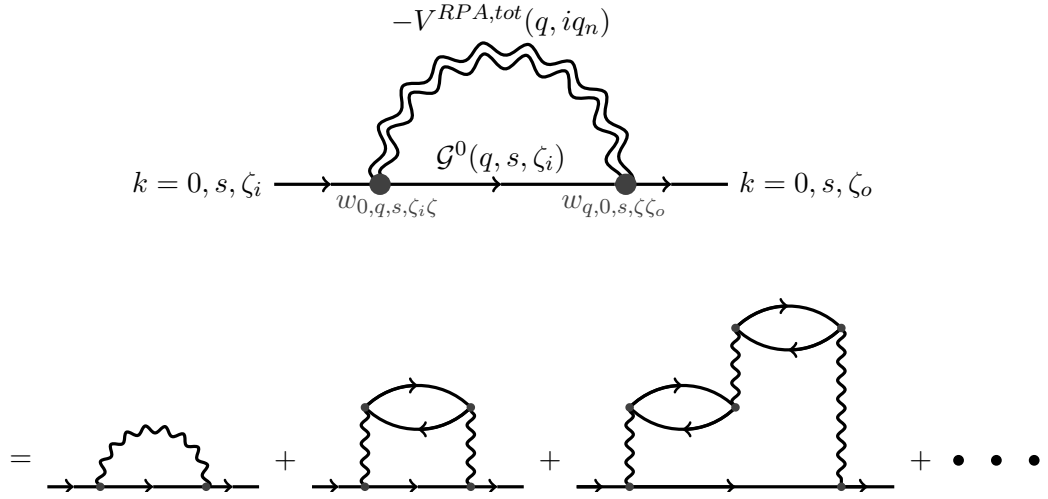

Figure 6.4: The diagrams in the RPA sum.

We will only calculate the RPA self-energy diagram for $k = 0$, which gives

$$\begin{aligned}\Sigma^{\mathrm{RPA,tot}}_{0,s}(\zeta_i, \zeta_o) =& \frac{1}{\beta}\int \frac{dq}{2\pi}\sum_{\zeta, iq_n}\left(-V^{\mathrm{RPA,tot}}(q, iq_n)\right) G^0(q, s, \zeta) w_{0,q,s,\zeta_i\zeta} w_{q,0,s,\zeta\zeta_o} \\ =& \Sigma^{\mathrm{Fock}}_{0,s}(\zeta_i, \zeta_o) + \frac{1}{\beta}\int \frac{dq}{2\pi}\sum_{\zeta, iq_n}\left(-V^{\mathrm{RPA}}(q, iq_n)\right) G^0(q, s, \zeta) w_{0,q,s,\zeta_i\zeta} w_{q,0,s,\zeta\zeta_o} \\ =& \Sigma^{\mathrm{Fock}}_{0,s}(\zeta_i, \zeta_o) + \Sigma^{\mathrm{RPA}}_{0,s}(\zeta_i, \zeta_o). \end{aligned} \tag{6.34}$$

Since both $G^0(q, s, \zeta)$ and $V^{\mathrm{RPA}}(q, iq_n)$ are even in q, we know from Eq. (6.5) that

$$\Sigma^{\mathrm{RPA}}_{0,s}(+, -) = \Sigma^{\mathrm{RPA}}_{0,s}(-, +) = 0. \tag{6.35}$$

The integrand in $\Sigma^{\mathrm{RPA}}_{0,s}(\zeta_i, \zeta_i)$ is even, so it is only necessary to integrate over q. For positive q we can approximate $G^0(q, s, \zeta)$ as

$$\begin{aligned} G^0(q, s, \zeta) =& \frac{1}{iq_n + ik_n - \zeta\xi_q} \\ \approx& \frac{1}{iq_n + ik_n - \zeta v_F q}, \end{aligned} \tag{6.36}$$

so

$$\begin{aligned}\Sigma^{\mathrm{RPA}}_{0,s}(\zeta_i, \zeta_i) = -\frac{1}{\beta}\int_{c_s}^{q_c} v_F dq \sum_{\zeta, iq_n}\Bigg(& \frac{4g^2 N_f v_F^2 q^2}{(iq_n - \alpha v_F q)(\alpha v_F q + iq_n)} \\ & \frac{1}{iq_n + ik_n - \zeta v_F q}\left|w_{0,q,s,\zeta\zeta_i}\right|^2\Bigg). \end{aligned} \tag{6.37}$$

The lower bound on the integral has been changed from 0 to c_s, since neither Eq. (6.36) nor Eq. (6.15) are valid for $q < c_s$. It was shown in the previous section that this is a good approximation. It is seen that for $\alpha \to 1$, i.e. the limit of weak interactions, Eq. (6.37) is identical to Eq. (6.16). This is what we expected, since the pair bubble is the dominant term in the RPA sum for weak interactions. We will now perform the Matsubara sum for an arbitrary $\alpha > 1$.

$$\begin{aligned}
\Sigma^{\mathrm{RPA}}_{0,s}(\zeta_i,\zeta_i) =& -4g^2N_fv_F\int_{c_s}^{q_\mathrm{c}} dq v_F^2q^2\sum_\zeta |w_{0,q,s,\zeta\zeta_i}|^2 \\
&\left(\frac{n_F(\zeta v_Fq)}{(\zeta v_Fq-ik_n-\alpha v_Fq)(\zeta v_Fq-ik_n+\alpha v_Fq)}\right. \\
&\left.+\frac{1}{-2\alpha v_Fq(-\alpha v_Fq+ik_n-\zeta v_Fq)}\right) \\
=& -4g^2N_fv_F\int_{c_s}^{q_\mathrm{c}} dq v_F^2q^2 \\
&\left(\frac{|w_{0,q,s,-\zeta_i}|^2}{(-(\alpha+1)v_Fq-ik_n)((\alpha-1)v_Fq-ik_n)}\right. \\
&+\frac{|w_{0,q,s,\zeta_i}|^2}{-2\alpha v_Fq(-(\alpha+1)v_Fq+ik_n)} \\
&\left.+\frac{|w_{0,q,s,-\zeta_i}|^2}{-2\alpha v_Fq(-(\alpha-1)v_Fq+ik_n)}\right) \\
\approx& -2g^2N_fv_F\int_{c_s}^{q_\mathrm{c}} dq v_F^2q^2 \\
&\left(\frac{1-\zeta_ic_s/q}{(-(\alpha+1)v_Fq-ik_n)((\alpha-1)v_Fq-ik_n)}\right. \\
&+\frac{1+\zeta_ic_s/q}{-2\alpha v_Fq(-(\alpha+1)v_Fq+ik_n)} \\
&\left.+\frac{1-\zeta_ic_s/q}{-2\alpha v_Fq(-(\alpha-1)v_Fq+ik_n)}\right). \qquad (6.38)
\end{aligned}$$

A short calculation gives

$$\begin{aligned}
\Sigma^{\mathrm{RPA}}_{0,s}(\zeta_i,\zeta_i) \approx& -2g^2N_f\left(ik_n+\zeta_i\frac{\alpha+1}{\alpha}v_Fc_s\right)v_F\int_{c_s}^{q_\mathrm{c}} dq\frac{v_Fq}{(\alpha+1)^2v_F^2q^2-(ik_n)^2} \\
=& -\frac{g^2}{(\alpha+1)^2}N_f\left(ik_n+\zeta_i\frac{\alpha+1}{\alpha}v_Fc_s\right)\ln\left(\frac{(\alpha+1)^2v_F^2q_\mathrm{c}^2-(ik_n)^2}{(\alpha+1)^2v_F^2c_s^2-(ik_n)^2}\right) \\
=& -\frac{g}{2}\frac{(\alpha-1)}{(\alpha+1)}\left(ik_n+\zeta_i\frac{\alpha+1}{\alpha}v_Fc_s\right)\ln\left(\frac{(\alpha+1)^2v_F^2q_\mathrm{c}^2-(ik_n)^2}{(\alpha+1)^2v_F^2c_s^2-(ik_n)^2}\right). \qquad (6.39)
\end{aligned}$$

Setting $ik_n = \omega$, we get an equation similar to Eq. (6.22),

$$\begin{aligned}\omega =& v_F c_s + \Sigma^{\text{Fock}} + \Sigma^{\text{RPA}} \\ =& \frac{1 + g\left(\ln(2q_c/c_s) - (\alpha-1)/\alpha \ln\left(\sqrt{((\alpha+1)^2 v_F^2 q_c^2 - \omega^2)/((\alpha+1)^2 v_F^2 c_s^2 - \omega^2)}\right)\right)}{1 + g(\alpha-1)/(\alpha+1)\ln\left(\sqrt{((\alpha+1)^2 v_F^2 q_c^2 - \omega^2)/((\alpha+1)^2 v_F^2 c_s^2 - \omega^2)}\right)} v_F c_s.\end{aligned} \tag{6.40}$$

Expanding in g gives

$$\omega = \left(1 + g\ln\left(\frac{2q_c}{c_s}\right)\right) v_F c_s + \mathcal{O}(g^2), \tag{6.41}$$

which isexactly the Fock term in Eq. (5.60). To evaluate it to second order in g, we observe that

$$\frac{\alpha-1}{\alpha} = gN_f + \mathcal{O}(g^2) \tag{6.42}$$

$$\frac{(\alpha-1)}{(\alpha+1)} = \frac{1}{2} gN_f + \mathcal{O}(g^2). \tag{6.43}$$

Thus, ω is given, to second order in g, by

$$\omega = \frac{1 + g\ln(2q_c/c_s) - g^2 N_f \ln\left(\sqrt{((\alpha+1)^2 v_F^2 q_c^2 - \omega^2)/((\alpha+1)^2 v_F^2 c_s^2 - \omega^2)}\right)}{1 + 1/2 g^2 N_f \ln\left(\sqrt{((\alpha+1)^2 v_F^2 q_c^2 - \omega^2)/((\alpha+1)^2 v_F^2 c_s^2 - \omega^2)}\right)} v_F c_s, \tag{6.44}$$

which is the same expression as for the pair bubble Eq. (6.22). The random phase approximation is thus consistent with the first and second order calculations.

We will now show that ω lies in the interval $[0, (\alpha+1)v_F c_s]$ for all values of the parameters g, c_s, q_c. At $g = 0$, i.e. the non-interacting limit, $\omega = v_F c_s$. For ω to be negative, it thus has to cross 0 as a function of g. For $\omega \to 0$, we find

$$\ln\left(\sqrt{\frac{(\alpha+1)^2 v_F^2 q_c^2 - \omega^2}{(\alpha+1)^2 v_F^2 c_s^2 - \omega^2}}\right) \xrightarrow{\omega\to 0} \ln\left(\frac{q_c}{c_s}\right), \tag{6.45}$$

so the numerator becomes

$$\begin{aligned}& 1 + g\left(\ln\left(\frac{2q_c}{c_s}\right) - \frac{\alpha-1}{\alpha}\ln\left(\sqrt{((\alpha+1)^2 v_F^2 q_c^2 - \omega^2)/((\alpha+1)^2 v_F^2 c_s^2 - \omega^2)}\right)\right) \\ \xrightarrow{\omega\to 0}& 1 + g\left(\ln\left(\frac{2q_c}{c_s}\right) - \frac{\alpha-1}{\alpha}\ln\left(\frac{q_c}{c_s}\right)\right) \\ =& 1 + g\left(\ln(2) + \frac{1}{\alpha}\ln\left(\frac{q_c}{c_s}\right)\right),\end{aligned} \tag{6.46}$$

which is always positive, since we are in the $q_c \gg c_s$ limit. Since the denominator in Eq. (6.40) is also positive, the whole righthand side is positive, so ω is always greater than zero. Looking at the other limit, we will let ω approach $\alpha + 1$ from below. This means that

$$\ln\left(\sqrt{\frac{(\alpha+1)^2 v_F^2 q_c^2 - \omega^2}{(\alpha+1)^2 v_F^2 c_s^2 - \omega^2}}\right) \xrightarrow{\omega\to\alpha+1} \infty. \tag{6.47}$$

The numerator thus goes to $-\infty$, while the denominator goes to $+\infty$. This means that the righthand side of Eq. (6.40) becomes negative, which is inconsistent with increasing ω. Therefore ω has the upper bound $\alpha + 1$.

Let us now look at the qualitative behaviour in the limits of weak and strong interactions, at finite values of c_s and q_c. As shown in Eq. (6.41), ω is dominated by the Fock term for weak interactions. It is thus increasing linearly as a function of g for small g. In the limit of strong interactions, we have

$$\frac{\alpha - 1}{\alpha} \xrightarrow{g\to\infty} 1, \tag{6.48}$$

$$\frac{\alpha - 1}{\alpha + 1} \xrightarrow{g\to\infty} 1, \tag{6.49}$$

and ω therefore reduces to

$$\omega \xrightarrow{g\to\infty} \left(\frac{\ln(2q_c/c_s)}{\ln\left(\sqrt{((\alpha+1)^2 v_F^2 q_c^2 - \omega^2)/((\alpha+1)^2 v_F^2 c_s^2 - \omega^2)}\right)} - 1\right) v_F c_s. \tag{6.50}$$

Using the result Eq. (6.45), we see that

$$\omega < \frac{\ln(2)}{\ln(q_c/c_s)} v_F c_s \quad \text{for} \quad g \to \infty. \tag{6.51}$$

For large g, $\omega/(v_F c_s)$ is thus decreasing as a function of q_c/c_s. For small g the Fock term dominates, so in this limit $\omega/(v_F c_s)$ increases as a function of q_c/c_s. We will now examine whether there is a value of g for which $\omega/(v_F c_s)$ is independent of q_c/c_s. Let us approximate

$$\ln\left(\sqrt{\frac{(\alpha+1)^2 v_F^2 q_c^2 - \omega^2}{(\alpha+1)^2 v_F^2 c_s^2 - \omega^2}}\right) \approx \ln\left(\sqrt{\frac{(\alpha+1)^2 v_F^2 q_c^2}{(\alpha+1)^2 v_F^2 c_s^2 - \omega^2}}\right). \tag{6.52}$$

This is a good approximation, since $\omega < (\alpha+1) v_F c_s$, and $q_c \gg c_s$. If we define

$$b = \frac{\omega}{(\alpha+1) v_F c_s}, \tag{6.53}$$

the approximated logarithm can be written as

$$\ln\left(\sqrt{\frac{(\alpha+1)^2 v_F^2 q_c^2}{(\alpha+1)^2 v_F^2 c_s^2 - \omega^2}}\right) = \ln\left(\frac{q_c}{c_s}\right) - \ln\left(\sqrt{1-b^2}\right). \tag{6.54}$$

Eq. (6.40) can therefore be written as

$$\begin{aligned} b(\alpha+1) =& \frac{1+g\ln\left(q_c/c_s\right)+g\ln(2)-g(\alpha-1)/\alpha\left(\ln\left(q_c/c_s\right)-\ln\left(\sqrt{1-b^2}\right)\right)}{1+g(\alpha-1)/(\alpha+1)\left(\ln(q_c/c_s)-\ln\left(\sqrt{1-b^2}\right)\right)} \\ \Rightarrow & b\left(\alpha+1+g(\alpha-1)\left(\ln\left(\frac{q_c}{c_s}\right)-\ln\left(\sqrt{1-b^2}\right)\right)\right) \\ =& 1+g\ln\left(\frac{q_c}{c_s}\right)+g\ln(2)-g\frac{\alpha-1}{\alpha}\left(\ln\left(\frac{q_c}{c_s}\right)-\ln\left(\sqrt{1-b^2}\right)\right). \end{aligned} \tag{6.55}$$

For $\omega/(v_F c_s)$ to be independent of q_c/c_s, this equation must be true for all values of q_c/c_s. Therefore we can split it into two equations, one for the terms containing a factor $\ln\left(q_c/c_s\right)$, and one for the rest,

$$bg(\alpha-1) = g\left(1-\frac{\alpha-1}{\alpha}\right), \tag{6.56}$$

$$b\left(\alpha+1-g(\alpha-1)\ln\left(\sqrt{1-b^2}\right)\right) = 1+g\ln(2)+g\frac{\alpha-1}{\alpha}\ln\left(\sqrt{1-b^2}\right). \tag{6.57}$$

This set of equations can be solved numerically, giving

$$g_{\text{fix}} = 0.452995 \tag{6.58}$$

$$\omega_{\text{fix}} = 1.27357 v_F c_s. \tag{6.59}$$

Note that without approximating ω as in Eq. (6.52), it would not be possible to solve Eq. (6.55) independent of q_c/c_s. The result is therefore only approximate, but since $q_c \gg \omega$, it is almost exact. The coupling strength $g = 0.46$ given in Eq. (4.47) is almost identical to g_{fix}. This means that the gap continues to depend linearly on c_s when interactions are included. $\omega/(v_F c_s)$ is increased from its non-interacting value which is 1, to

$$\gamma_{\text{fix}} = \frac{\omega_{\text{fix}}}{v_F c_s} = 1.27. \tag{6.60}$$

We will now solve Eq. (6.40) numerically. In Fig. 6.5 $\omega/(v_F c_s)$ is plotted as a function of g for different values of q_c/c_s. It is seen that the calculated values of g_{fix} and ω_{fix} fit well to the point where the curves intersect. The relative gap decreases as a function of c_s for interactions weaker than g_{fix}, and it increases as a function of c_s above g_{fix}. In Fig. 6.6 the relative gap is plotted as a function of c_s for small gaps. The interaction strength is chosen as $g = 0.105$, which is the maximum of the blue curve in Fig. 6.5. It seems plausible that the gap is smaller than $(\alpha+1)v_F c_s$ for any g or c_s. In Fig. 6.7, the gap energy is shown as a function of c_s. It is seen that the non-linear behavior is almost negligible. However, the slope is multiplied by $\omega/(v_f c_s)$, which for $g = g_{\text{fix}}$ is $\gamma_{\text{fix}} = 1.27$.

To estimate how the RPA screened interaction affects the other diagrams in the perturbation series, we will make a cruder approximation. Setting $ik_n = \zeta_i v_F c_s$, i.e. the

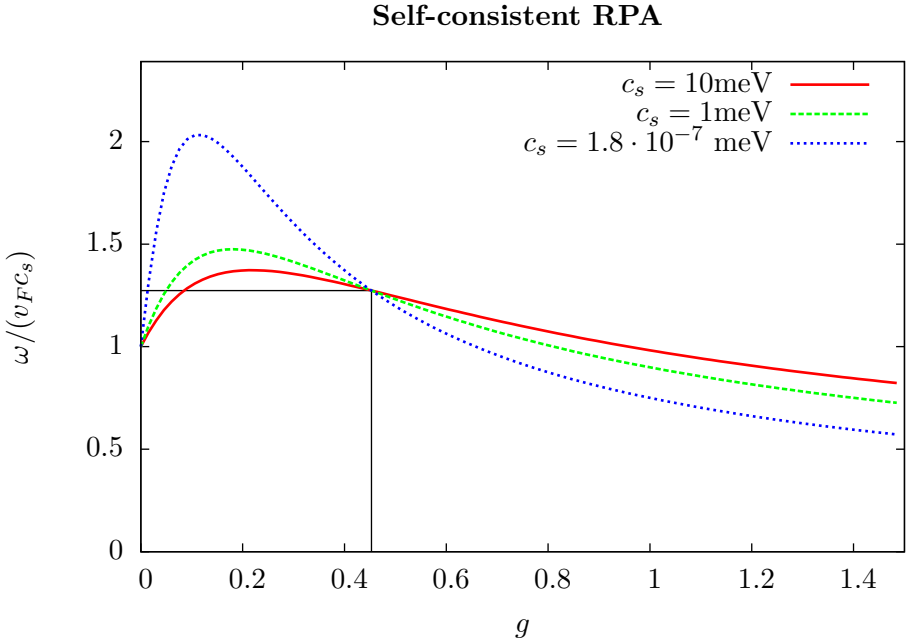

Figure 6.5: The gap energy ω in units of the non-interacting gap $v_F c_s$, from the self-consistent solution of Eq. (6.40) as a function of the interaction strength g. The radius is fixed at $R = 1\,\mathrm{nm}$, and the red, green and blue curves correspond to three different values of the gap. It is seen that at $g = g_{\mathrm{fix}} = 0.45$, the relative gap increase does not depend on the particular value of c_s.

non-interacting value, we find

$$\begin{aligned}\Sigma_{0,s}^{\mathrm{RPA}}(\zeta_i,\zeta_i) \approx& -\zeta_i g\frac{(\alpha-1)}{(\alpha+1)}\frac{2\alpha+1}{\alpha}v_F c_s \ln\left(\sqrt{(4v_F^2q_{\mathrm{c}}^2 - v_F^2c_s^2)/(3v_F^2c_s^2)}\right)\\ \approx& -\zeta_i g\frac{(\alpha-1)}{(\alpha+1)}\frac{2\alpha+1}{\alpha}v_F c_s \ln\left(\frac{2q_{\mathrm{c}}}{c_s}\right).\end{aligned} \tag{6.61}$$

The last approximation leads to $\Sigma_{0,s}^{\mathrm{RPA}}$ and $\Sigma_{0,s}^{\mathrm{Fock}}$ having the same dependence on q_{c}. It is justified from the observation that the prefactor in the logarithm depends heavily on the value of the low momentum cut-off in Eq. (6.39), and the cut-off could just as well have been chosen a factor 2 smaller or larger without violating any assumptions. Therefore we may now write

$$\begin{aligned}\Sigma_{0,s}^{\mathrm{RPA,tot}}(\zeta_i,\zeta_i) =& \Sigma_{0,s}^{\mathrm{Fock}}(\zeta_i,\zeta_i) + \Sigma_{0,s}^{\mathrm{RPA}}(\zeta_i,\zeta_i)\\ =& g_\alpha v_F c_s \ln\left(\frac{2q_{\mathrm{c}}}{c_s}\right),\end{aligned} \tag{6.62}$$

where

$$g_\alpha = g\left(1 - \frac{(\alpha-1)}{(\alpha+1)}\frac{2\alpha+1}{\alpha}\right). \tag{6.63}$$

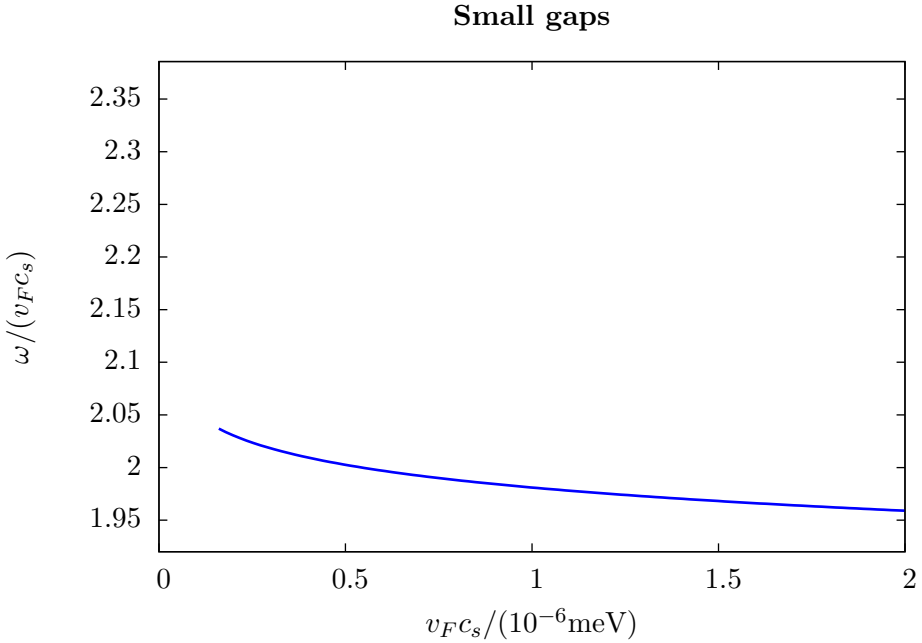

Figure 6.6: The relative gap size for small gaps. The interaction strength is $g = 0.105$, which is the position of the maximum of the blue curve in Fig. 6.5. This corresponds to $\alpha + 1 = 2.38$. The tube radius is 1 nm, as before.

We find that the contributions of the RPA diagrams partially cancel the contribution of the Fock diagram. This agrees with our interpretation of RPA as being effectively a screening of the interaction. Using Eq. (6.32), the maximal value of g_α as a function of g is

$$g_{\alpha,\max} = 0.08, \tag{6.64}$$

which is at $g = 0.23$. The screened coupling constant is thus smaller than 0.08. Using this screened interaction to calculate all higher order diagrams, we find that their contribution is negligible. Going to higher order in perturbation theory would not change the self-energy more than by a correction of the order g_α^2, so we conclude that higher order terms are negligible.

For estimating the precision of this approximation, it is plotted together with the self-consistent solution of Eq. (6.40) and the Fock self-energy from Eq. (5.60) in Fig. 6.8. One clearly sees that using the screened interaction gives a result that is much closer to the self-consistent result than the result obtained using the Fock diagram. For large gaps and weak interactions, it is thus a good approximation. However, from Eq. (6.62) it is seen that in this approximation, the relative gap diverges for small gaps, which is not the case for the self-consistent solution. For sufficiently strong interactions it becomes negative, which is unphysical. Therefore we conclude that the approximation breaks down for small gaps and strong interactions.

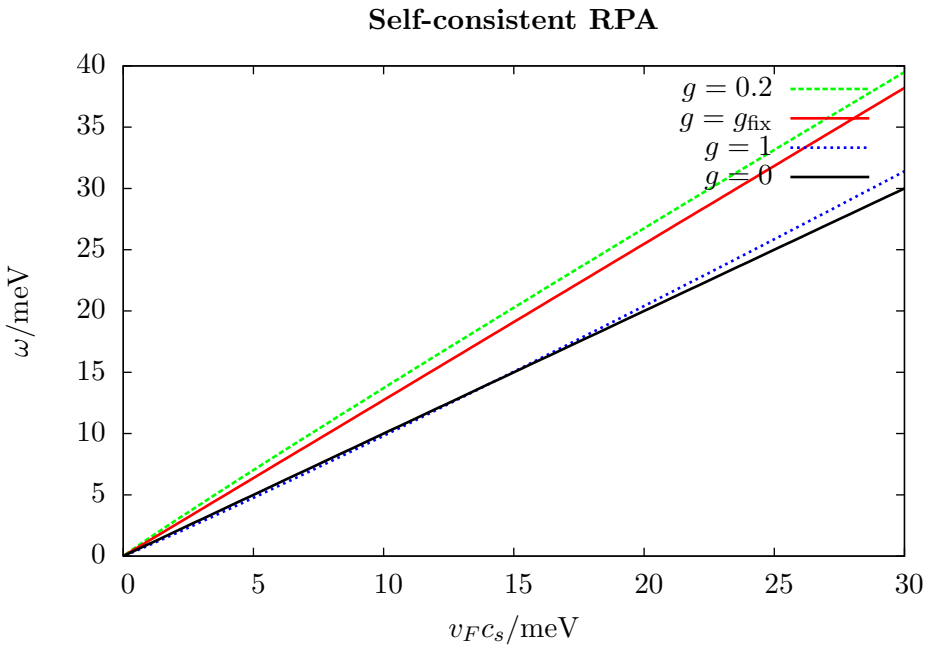

Figure 6.7: The gap energy as a function of c_s. The black line is the non-interacting value $\omega = v_F c_s$. The red line represents $g = g_{\text{fix}}$, so is also linear in $v_F c_s$, but with an increased slope. The green and blue lines are curved in opposite directions, since their interaction strengths are on opposite sides of g_{fix}.

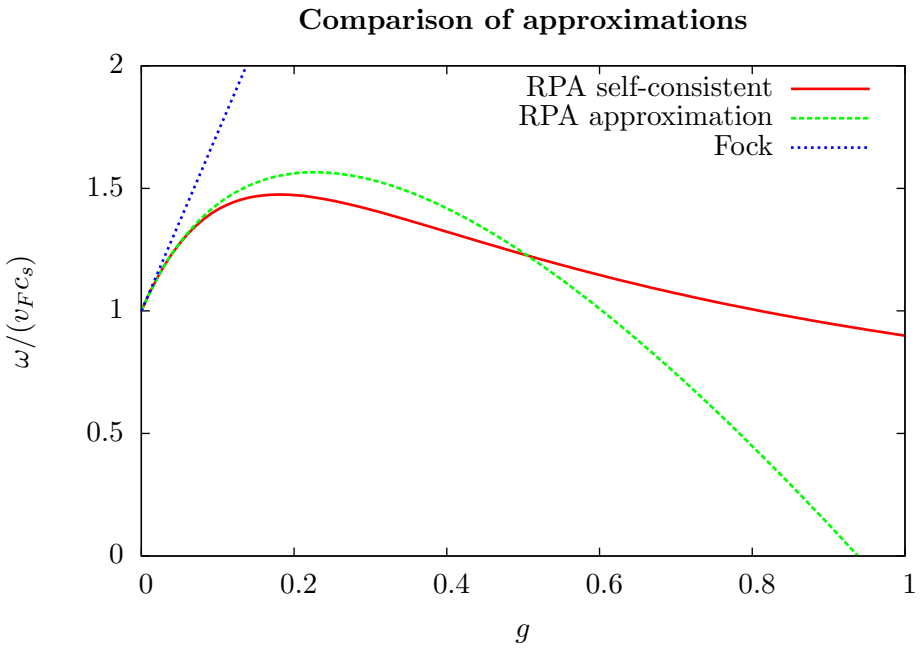

Figure 6.8: The relative gap as a function of g calculated from the Fock diagram Eq. (5.60), the approximated RPA Eq. (6.62) and the self-consistent RPA Eq. (6.40). The Fock self-energy quickly diverges, while the approximated RPA becomes negative for large g. Only the self-consistent RPA is well-behaved for all values of g. The parameters used are $R = 1\,\mathrm{nm}$ and $c_s = 1\,\mathrm{meV}$.

Chapter 7

Experimental evidence and predictions

7.1 Anomalous orbital magnetic moment

When comparing the effective graphene Hamiltonian Eq. (2.66) to the effective nanotube Hamiltonian Eq. (4.1), it is seen that the gap c_s corresponds to a momentum in the circumferential direction. The circumferential momentum can be measured by applying a magnetic field parallel to the tube axis. This is due to the Aharanov-Bohm effect, from which a magnetic field adds a phase to the electron wave function [15], so

$$k_\perp(B) = c_s + \tau\frac{eRB}{2}, \tag{7.1}$$

where $\tau = \pm 1$ denotes $\boldsymbol{K}$ or $\boldsymbol{K}'$ cones, e is the electron charge and R is the radius of the tube. From this we define the magnetic field at which the gap vanishes, B_{Dirac}, as

$$B_{\text{Dirac}} = \frac{2c_s}{eR}. \tag{7.2}$$

We may also define an orbital magnetic moment μ_{orb} as

$$\frac{dE_{0,s,+}}{dB} = \tau\mu_{\text{orb}} + \frac{1}{2}sg_s\mu_B \tag{7.3}$$

where $s = \pm 1$ spin up or down, $g_s \approx 2$ is the electron spin g factor, $\mu_B \approx 5.8 \cdot 10^{-5}\text{eV}\cdot\text{T}^{-1}$ is the Bohr magneton, and $E_{0,s,+}$ is the energy of the $k = 0$ state as defined in Eq. (4.2). The orbital magnetic moment is [1]

$$\mu_{\text{orb}} = \frac{\tau eR}{2}\frac{dE_{0,s,+}}{dk_\perp} = \frac{eR}{2}v_\perp, \tag{7.4}$$

where $v_\perp$ is the Fermi velocity in the perpendicular direction. The self-energy is diagonal in momentum space, so Coulomb interactions do not change the momentum of a state.

Thus, a state with a definite $k_\perp$ in the non-interacting theory has the same $k_\perp$ after interactions have been included. Therefore

$$k_\perp = c_s. \tag{7.5}$$

Including interactions, $E_{0,s,+}$ is no longer equal to $v_F c_s$, but to ω. From Fig. 6.7 it is seen that ω is nearly proportional to c_s. Therefore we may approximate

$$v_\perp = \frac{dE_{0,s,+}}{dk_\perp} \approx \frac{\omega}{c_s}, \tag{7.6}$$

so

$$\mu_{\text{orb}} = \frac{eR}{2}\frac{\omega}{c_s}. \tag{7.7}$$

In [1], the orbital magnetic moment was measured for several nanotubes. For their "Device 1" the orbital magnetic moment was measured to be

$$\mu_{\text{orb,exp}}^{\text{Steele}} = 1.6\,\text{meV/T}. \tag{7.8}$$

For this tube the diameter was also measured using atomic force microscopy to be 3 nm. Using Eq. (7.4) with the non-interacting Fermi velocity v_F from Eq. (4.41) and their measured radius, this gives an orbital magnetic moment of

$$\mu_{\text{orb,non-int}}^{\text{Steele}} = 0.82\,\text{meV/T}. \tag{7.9}$$

The measured orbital magnetic moment is thus larger by a factor of 2 than predicted by the non-interacting theory. Our interacting theory predicts a higher orbital magnetic moment than the non-interacting theory, namely

$$\mu_{\text{orb,int}} = \gamma_{\text{fix}}\mu_{\text{orb,non-int}}, \tag{7.10}$$

using $g = g_{\text{fix}}$. For Steele's experiment, we predict

$$\mu_{\text{orb,int}}^{\text{Steele}} = 1.04\,\text{meV/T}. \tag{7.11}$$

This is not as high as the measured value, so it can not be the full explanation of the anomalously high magnetic moment.

Some recent experimental results are shown in Table 7.1. When no theoretical value is given, it is because the radius has not been measured. In most experiments measuring μ_{orb}, the radius is not measured explicitly. However, Jespersen et al. [15] notes that "nanotubes grown by chemical vapour deposition (...) are expected to have $D \leq 3\,\text{nm}$", where $D = 2R$ is the diameter of the tube. We thus do not expect orbital magnetic moments higher than $\mu_{\text{orb}} = 0.82\,\text{meV/T}$. This contradicts recent experiments [2, 15, 1], as seen in Table 7.1. The measurement by Jespersen et al. is close enough for the deviation to be explained by measurement and diameter limit uncertainty, but only in the case where the diameter is actually 3 nm. In the non-interacting theory, $\mu_{\text{orb}}^{\text{Kuemmeth}}$ correspond to the radius

$$R_{non-int}^{\text{Kuemmeth}} = 2.83\,\text{nm}, \tag{7.12}$$

Author	Measured μ_{orb} in meV/T	Non-interacting theoretically predicted μ_{orb} in meV/T	On substrate/ Suspended
Steele et al. [1]	1.6	0.82	Suspended
Kuemmeth et al. [2]	1.55		
Jespersen et al. [15]	0.87		On substrate
Makarovski et al. [17]	0.41		On substrate
Churchill et al. [18]	0.330		On substrate
Deshpande et al. [19]	0.330		Suspended
Jarillo-herrero et al. [20]	0.85 ± 0.05	1.09	On substrate
Minot et al. [16], 1	0.7 ± 0.1	0.7	Suspended
Minot et al. [16], 2	1.5 ± 0.2	1.4	Suspended

Table 7.1: Experimental measurements of μ_{orb}.

which is significantly higher than the maximum value $R_{max} = 1.5\,\text{nm}$ set by Jespersen et al. Our theory predicts

$$R_{\text{int}}^{\text{Kuemmeth}} = \frac{R_{\text{non-int}}^{\text{Kuemmeth}}}{\gamma_{\text{fix}}} = 2.23\,\text{nm}, \tag{7.13}$$

which is not enough to account for the measured value.

There are also studies who got lower orbital magnetic moments, namely [17, 18, 19] Finally, there are experiments similar to the one by Steele et al., measuring both the orbital magnetic moment and the radius directly [20, 16] The experimental data are not conclusive. A further complication is that there are two kinds of experiments. Either the tube lies directly on the substrate, or it is suspended between the leads. If a tube is in contact with the substrate, the long range Coulomb interactions might be screened by the substrate, reducing the effect of Coulomb interactions. For a suspended tube, this is not the case. The experiments [1, 16, 19] are suspended, while [15, 20, 17, 18] have tubes lying directly on the substrate. There is thus no clear link between enhanced magnetic moment and suspended tubes. However, Steele [1] mentions that "The devices measured here and those measured by Kuemmeth et al. [2] were made using clean nanotubes grown in the last step of the fabrication, while [many of] the other measurements were performed on nanotubes which were grown first and subsequently underwent processing in the cleanroom." There is thus a qualitative difference between the experiments with low and high μ_{orb}. We will however not investigate this further in this thesis.

An interesting feature of Fig. 6.5 is that lower interaction strength actually increases the orbital magnetic moment, since screening from RPA is most pronounced for strong interactions. This means that if the interaction is screened by a substrate, it might in fact lead to a higher orbital magnetic moment.

7.2 Implications on spin-orbit band splitting

As described in Section 3.2.4, Izumida et al. found that spin up and down electrons do not have the same energy difference as spin up and spin down holes [12]. The energy splitting for electrons is

$$\begin{aligned}\Delta_+^{\text{Izumida}} &= 2v_F\Delta k_{\text{soc}} + 2\tau\epsilon_{\text{soc}}^{(\tau)} \\ &= 2\alpha_1\frac{V_{\text{so}}}{2R} + 2\alpha_2\frac{V_{\text{so}}}{2R}\cos 3\eta,\end{aligned} \tag{7.14}$$

whereas for holes

$$\begin{aligned}\Delta_-^{\text{Izumida}} &= 2v_F\Delta k_{\text{soc}} - 2\tau\epsilon_{\text{soc}}^{(\tau)} \\ &= 2\alpha_1\frac{V_{\text{so}}}{2R} - 2\alpha_2\frac{V_{\text{so}}}{2R}\cos 3\eta.\end{aligned} \tag{7.15}$$

The parameters α_1 and α_2 are given in Eqs. (3.80) and (3.81) as

$$\alpha_1 = 0.048\,\text{nm}, \tag{7.16}$$

$$\alpha_2 = -0.045\,\text{nm}. \tag{7.17}$$

It is seen in Eqs. (3.73)–(3.81) that α_1 is proportional to c_s in the effective model Eq. (4.1), while α_2 is proportional to d. α_1 is therefore scaled by the Coulomb interactions by a factor

$$\frac{\tilde{\alpha_1}}{\alpha_1} = \frac{\omega}{v_F c_s} = \gamma_{\text{fix}}, \tag{7.18}$$

while α_2 remains unaltered. Since $|\alpha_2| < |\alpha_1|$, the difference between hole and electron splitting is largest for $\eta = 0$, i.e. a zig-zag tube. In this case the ratio between the hole splitting and the electron splitting is

$$\frac{\Delta_-^{\text{Izumida}}}{\Delta_+^{\text{Izumida}}} = \frac{\alpha_1 - \alpha_2}{\alpha_1 + \alpha_2} \approx 31. \tag{7.19}$$

Our theory however predicts

$$\frac{\Delta_-^{\text{int}}}{\Delta_+^{\text{int}}} = \frac{\tilde{\alpha}_1 - \alpha_2}{\tilde{\alpha}_1 + \alpha_2} \approx 7. \tag{7.20}$$

Zig-zag tubes still give the largest ratio, but it is five times smaller than in the non-interacting theory. An experimental test of this theory would thus be to measure the splitting ratio for a zig-zag tube.

Steele et al. [1] measured a spin-orbit splitting of

$$\Delta_{\text{so,exp}}^{\text{Steele}} = 3.4\,\text{meV} \tag{7.21}$$

for the conduction band. According to the non-interacting theory, their tube should maximally have a spin-orbit splitting of

$$\Delta_{\text{so,non-int}}^{\text{Steele}} = 0.260\,\text{meV}. \tag{7.22}$$

The spin-orbit interaction is thus 13 times higher than expected. Interactions enhance the gap regardless of whether it is due to curvature or spin-orbit effects. If the gap is enhanced by some factor compared to the non-interacting theory, the same happens for the spin-orbit splitting. Kane et al. [3] have shown that short range interactions enhance the gap by a factor 1.36. Our theory further enhances the theoretically predicted value by a factor 1.27. In total, this gives an enhancement of 1.73, yielding

$$\Delta_{\text{so,int}}^{\text{Steele}} = 0.45\,\text{meV}. \tag{7.23}$$

There is still a factor 8 in discrepancy between the value predicted by theory and the experimental result, so long range interactions are not solely responsible for the large spin-orbit coupling. Furthermore, the splittings

$$\Delta_{+}^{\text{Kuemmeth}} = 0.37\,\text{meV}, \tag{7.24}$$

$$\Delta_{-}^{\text{Kuemmeth}} = 0.22\,\text{meV} \tag{7.25}$$

have been measured by Kuemmeth et al. [2]. As discussed at the end of Chapter 3, the non-interacting theory predicts a larger valence band splitting than hole splitting. Our theory can never make the conduction band splitting larger than the valence band splitting, since it only changes α_1.

Chapter 8

Concluding remarks

8.1 Summary

A perturbatively stable theory of how long range Coulomb interactions enhance the gap in nearly metallic carbon nanotubes has been developed in this thesis. In Section 5.4 the first order correction to the gap self-energy is developed. It is shown that the circumferential Fermi velocity is enhanced, and even diverges logarithmically for small gaps. This gives rise to a large gap increase for nearly metallic tubes. The effect is identical to the one found in graphene [28] and semiconducting nanotubes [3] arising from short range Coulomb interactions.

In Section 5.7 it was however shown that the Coulomb interaction is so strong that a self-consistent solution of the first order gap enhancement is divergent. However, similar to graphene [27], it is possible to do a $1/N_f$ expansion and sum all the RPA bubbles, as done in Section 6.3. Due to the high number of cones ($N_f = 4$), this is assumed to be a good approximation. The random phase approximation results in a screened interaction. For gaps larger than 1 meV and interactions weaker than $g = 0.6$, RPA can be well approximated by first order perturbation theory, where the interaction strength is reduced from $g = 0.46$ to $g_\alpha = 0.1$. For smaller gaps or stronger interactions, the RPA self-energy has to be solved self-consistently. In the self-consistent calculation the gap is never enhanced by more than a factor 2.38, for any value of the initial gap or interaction strength. At $g = 0.46$ the gap is approximately 1.27 times larger than the non-interacting gap. The enhancement of the gap leads to higher orbital magnetic moment and spin-orbit splitting. The experiments discussed in Chapter 7 also find values of the orbital magnetic moment and spin-orbit splitting that are too high to be explained by the non-interacting theory. However, the enhancement derived in this thesis is not large enough to quantitatively account for these previously unexplained experimental results.

8.2 Outlook

The relatively weak enhancement of the gap calculated in this thesis is not enough to explain the large values of orbital magnetic moment and spin-orbit splitting measured

in recent experiments [2, 1]. Furthermore, Kuemmeth et al. [2] measured a larger spin-orbit splitting in the conduction band than in the valence band, in contradiction to the non-interacting theory [12]. Our theory would never be able to invert this asymmetry, since it is symmetric in conduction and valence band. Other effects should therefore be considered to understand this phenomenon. In the non-interacting theory [12] as well as in our interacting theory, the gap is predicted to close for a particular magnetic field aligned along the nanotube axis, B_{Dirac}. However, both Steele et al. [1] and Deshpande et al. [14] found that the gap has a residual value of $\sim 50\,\text{meV}$ at B_{Dirac}. This is a huge effect compared to our predicted renormalization. Being still unexplained, the physical effects giving rise to this phenomenon could potentially change crucial elements of our theory. It thus seems more important to explain this B_{Dirac} gap, than to improve the precision of our theory.

The first order diagram calculated in Section 5.4 leads to a logarithmically divergent circumferential Fermi velocity. In the approximated RPA model presented in the end of Section 6.3, the interaction is screened, but otherwise gives rise to the same logarithmic divergence. However, our self-consistent RPA shows that the divergence is an artefact of this approximation. In graphene the same logarithmic divergence has been found [38]. Here the gap is not tuned by a magnetic field, but by changing the chemical potential. This means that there is no residual gap, so it is possible to examine the behaviour for much smaller gaps. It would be interesting to use the self-consistent RPA method on graphene, to investigate whether it suppresses the logarithmic divergence in graphene, as it does in carbon nanotubes.

Bibliography

[1] G. A. Steele, F. Pei, E. A. Laird, J. M. Jol, H. B. Meerwaldt, and L. P. Kouwenhoven. Large spin-orbit coupling in carbon nanotubes. *Nat Commun*, 4:1573, Mar 2013.

[2] F. Kuemmeth, S. Ilani, D. C. Ralph, and P. L. McEuen. Coupling of spin and orbital motion of electrons in carbon nanotubes. *Nature*, 452(7186):448–452, 2008.

[3] C. L. Kane and E. J. Mele. Electron interactions and scaling relations for optical excitations in carbon nanotubes. *Phys. Rev. Lett.*, 93:197402, Nov 2004.

[4] P. R. Wallace. The band theory of graphite. *Phys. Rev.*, 71:622–634, May 1947.

[5] K. S. Novoselov, A. K. Geim, S. V. Morozov, D. Jiang, Y. Zhang, S. V. Dubonos, I. V. Grigorieva, and A. A. Firsov. Electric field effect in atomically thin carbon films. *Science*, 306(5696):666–669, 2004.

[6] A. K Geim and K. S Novoselov. The rise of graphene. *Nature materials*, 6(3):183–191, 2007.

[7] M. E. Peskin and D. V. Schroeder. *An Introduction to Quantum Field Theory*. Perseus Books, Cambridge, Massachusetts, 1995.

[8] M. Srednicki. *Quantum Field Theory*. Cambridge University Press, Cambridge, 2007.

[9] D. P. DiVincenzo and E. J. Mele. Self-consistent effective-mass theory for intralayer screening in graphite intercalation compounds. *Phys. Rev. B*, 29:1685–1694, Feb 1984.

[10] D.J. Griffiths. *Introduction to quantum mechanics*. Pearson Prentice Hall, 2005.

[11] A. Kleiner and S. Eggert. Band gaps of primary metallic carbon nanotubes. *Phys. Rev. B*, 63:073408, Jan 2001.

[12] W. Izumida, K. Sato, and R. Saito. Spin–orbit interaction in single wall carbon nanotubes: Symmetry adapted tight-binding calculation and effective model analysis. *Journal of the Physical Society of Japan*, 78(7):074707, 2009.

[13] J. J. Sakurai and J. Napolitano. *Modern quantum mechanics*. Pearson Education, 2009.

[14] V. V. Deshpande, B. Chandra, R. Caldwell, D. S. Novikov, J. Hone, and M. Bockrath. Mott insulating state in ultraclean carbon nanotubes. *Science*, 323(5910):106–110, 2009.

[15] T. S. Jespersen, K. Grove-Rasmussen, K. Flensberg, J. Paaske, K. Muraki, T. Fujisawa, and J. Nygård. Gate-dependent orbital magnetic moments in carbon nanotubes. *Phys. Rev. Lett.*, 107:186802, Oct 2011.

[16] E. D. Minot, Y. Yaish, V. Sazonova, and P. L. McEuen. Determination of electron orbital magnetic moments in carbon nanotubes. *Nature*, 428(6982):536–539, Apr 2004.

[17] A. Makarovski, A. Zhukov, J. Liu, and G. Finkelstein. Su(2) and su(4) kondo effects in carbon nanotube quantum dots. *Phys. Rev. B*, 75:241407, Jun 2007.

[18] H. O. H. Churchill, F. Kuemmeth, J. W. Harlow, A. J. Bestwick, E. I. Rashba, K. Flensberg, C. H. Stwertka, T. Taychatanapat, S. K. Watson, and C. M. Marcus. Relaxation and dephasing in a two-electron nanotube double quantum dot. *Phys. Rev. Lett.*, 102:166802, Apr 2009.

[19] V. V. Deshpande and M. Bockrath. The one-dimensional wigner crystal in carbon nanotubes. *Nat Phys*, 4(4):314–318, Apr 2008.

[20] P. Jarillo-Herrero, J. Kong, H. S. J. van der Zant, C. Dekker, L. P. Kouwenhoven, and S. De Franceschi. Electronic transport spectroscopy of carbon nanotubes in a magnetic field. *Phys. Rev. Lett.*, 94:156802, Apr 2005.

[21] Y. A. Krotov, D.-H. Lee, and S. G. Louie. Low energy properties of carbon nanotubes. *Phys. Rev. Lett.*, 78:4245–4248, Jun 1997.

[22] A. A. Odintsov and H. Yoshioka. Universality of electron correlations in conducting carbon nanotubes. *Phys. Rev. B*, 59:R10457–R10460, Apr 1999.

[23] A. A. Nersesyan and A. M. Tsvelik. Coulomb blockade regime of a single-wall carbon nanotube. *Phys. Rev. B*, 68:235419, Dec 2003.

[24] H. Bruus and K. Flensberg. *Many-Body Quantum Theory in Condensed Matter Physics*. Oxford University Press, Oxford, 2004.

[25] C. Kane, L. Balents, and M. P. A. Fisher. Coulomb interactions and mesoscopic effects in carbon nanotubes. *Phys. Rev. Lett.*, 79:5086–5089, Dec 1997.

[26] L. S. Levitov and A. M. Tsvelik. Narrow-gap luttinger liquid in carbon nanotubes. *Phys. Rev. Lett.*, 90:016401, Jan 2003.

[27] V. N. Kotov, B. Uchoa, and A. H. Castro Neto. 1/n expansion in correlated graphene. *Phys. Rev. B*, 80:165424, Oct 2009.

[28] D. C. Elias, R. V. Gorbachev, A. S. Mayorov, S. V. Morozov, A. A. Zhukov, P. Blake, L. A. Ponomarenko, I. V. Grigorieva, K. S. Novoselov, F. Guinea, and A. K. Geim. Dirac cones reshaped by interaction effects in suspended graphene. *Nat Phys*, 7(9):701–704, Sep 2011.

[29] C. Kittel. *Introduction to Solid State Physics*. John Wiley & Sons, Inc., New York, 6th edition, 1986.

[30] R. Saito, G. Dresselhaus, and M. S. Dresselhaus. *Physical Properties of Carbon Nanotubes*. Imperial College Press, London, 1998.

[31] A. M. Lunde. Coulomb Drag in Multiwall Carbon Nanotubes. Master's thesis, Niels Bohr Institute, University of Copenhagen and MIC, Technical University of Denmark, Denmark, 2004.

[32] G. S. Painter and D. E. Ellis. Electronic band structure and optical properties of graphite from a variational approach. *Phys. Rev. B*, 1:4747–4752, Jun 1970.

[33] `http://http://tex.stackexchange.com/questions/54341` [2014, February 12].

[34] A. Kramida, Yu. Ralchenko, J. Reader, and and NIST ASD Team. NIST Atomic Spectra Database (ver. 5.1), [Online]. Available: `http://physics.nist.gov/asd` [2014, January 31]. National Institute of Standards and Technology, Gaithersburg, MD., 2013.

[35] A. Secchi and M. Rontani. Intervalley scattering induced by coulomb interaction and disorder in carbon-nanotube quantum dots. *Phys. Rev. B*, 88:125403, Sep 2013.

[36] D.J. Griffiths. *Introduction to electrodynamics*. Prentice Hall, 1999.

[37] M. Abramowitz and I. A. Stegun. *Handbook of Mathematical Functions*. National Bureau of Standards Applied Mathematics Series 55, Washington DC, 1964.

[38] V. N. Kotov, B. Uchoa, V. M. Pereira, F. Guinea, and A. H. Castro Neto. Electron-electron interactions in graphene: Current status and perspectives. *Rev. Mod. Phys.*, 84:1067–1125, Jul 2012.